REVIEW ARTICLE

Check for updates

Lattice strain inhomogeneity in halide perovskite films: its origins and regulations

Yun-Kyeong Hong,† Yu-Na Lee† and Hui-Seon Kim ⓘD *

Since perovskite solar cells reached an astonishing power conversion efficiency of 27%, the persistent stability issue has received significant attention, paving the way for a major step up in commercialization. Strain control has been proposed as a promising technology to address the stability issue because defects governing the structural stability are susceptible to lattice strain. Accordingly, various strategies have been developed and found to be effective in terms of device stability. Nevertheless, most of them are based on interface management by varying target molecules at the interface without understanding the underlying fundamentals. In this review article, we thoroughly investigate the origins of lattice strain in perovskite films, ranging from the atomic scale to the bulk scale, and introduced effective approaches to resolve the strain issue by listing relevant materials. Finally, the synergistic effect of strain regulation is discussed to recognize the feasible impact from the perspective of device performance.

1. Introduction

Since the development of all solid-state perovskite solar cells (PSCs) in 2012,[1,2] a rapid transition has been observed in the research field of emerging photovoltaics.[3,4] The certified power conversion efficiency (PCE) of PSCs recently reached 27.0% owing to intensive efforts from various perspectives, including compositional engineering, interface engineering and modulating crystal growth, along with in-depth fundamental understanding,[5,6] which makes PSCs become one of the most competitive technologies in the photovoltaic market. In this regard, strong demand from industry is well reflected in a steep increase in the perovskite solar module efficiency, recently reaching a PCE of 21.1% over 843.5 cm^2,[7] by improving scalable technology for commercialization to reduce the gap between unit cell and module.[8,9] The astonishing progress in the PCE of PSCs mainly relies on the intrinsic superb properties of the halide perovskite APbI$_3$ (A$^+$ = formamidinium (FA$^+$), methylammonium (MA$^+$), or Cs$^+$),[10] where its distinctive electronic band structure is favorable for photon absorption,[11] low exciton binding energy,[12] balanced long diffusion coefficient for electrons and holes,[13,14] and suppressed charge recombination with high defect tolerance.[15,16] Nevertheless, stability has been a chronic issue in PSCs, although significant progress has been certainly observed with satisfying stringent criteria for module test.[17–19] Recently, the importance of residual lattice strain in the perovskite film has been highlighted not only because

Department of Chemistry and Chemical Engineering, Inha University, Incheon 22212, Republic of Korea. E-mail: hui-seon.kim@inha.ac.kr
† These authors contributed equally to this work.

Yun-Kyeong Hong is an integrated MS-PhD student under Prof. Hui-Seon Kim in the Department of Chemistry and Chemical Engineering, Inha University, Korea, where she also completed her undergraduate study in 2023. Her research focuses on perovskite solar cells (PSCs), with particular interest in strain engineering and the reliability assessment of perovskite solar modules.

Yun-Kyeong Hong

Yu-Na Lee is an integrated MS-PhD student under the supervision of Prof. Hui-Seon Kim in the Department of Chemistry and Chemical Engineering, Inha University, Korea. She obtained her bachelor's degree from Gangneung-Wonju National University in 2023. Her research focuses on PSCs, particularly on controlling crystallographic orientation during crystal growth.

Yu-Na Lee

residual strain readily alters the optoelectronic properties by manipulating the electronic band structure[20,21] but also because lattice stability is highly susceptible to residual strain.[22] Despite controversial approaches to strain engineering,[23,24] it is generally regarded that the in-plane tensile strain resides in the solution-processed halide perovskite film owing to a mismatch in thermal expansion coefficients between the soft perovskite film and the rigid inorganic substrate.[25,26] As theoretically demonstrated, tensile strain is responsible for the increased bandgap and decreased hole mobility, while increased hole mobility is estimated under compressive strain.[27,28] Therefore, compressive strain frequently induces favorable charge transport dynamics and thereby increases the PCE of PSCs.[28,29] Furthermore, superb long-term stability of PSCs is generally enabled by alleviating in-plane tensile strain in the perovskite film.[25] Similarly, many recent studies adopt strain engineering strategies toward achieving a strain-free film by fully relieving the in-plane tensile strain or even inducing in-plane compressive strain to benefit both photovoltaic performance and long-term stability.

Although structural inhomogeneity, being responsible for lattice strain, can be imposed by appreciable lattice tilting on an atomic scale,[30,31] the local strain is further pronounced by the polycrystalline nature with randomly ordered crystals based on solution and low temperature process.[27] In addition, advanced dopant engineering and annealing processes for crystallization lead to depth-dependent lattice strain in the perovskite film.[32] Similarly, the lattice of halide perovskite unavoidably employs various multi-dimensional strains. Even though halide perovskite is widely known as soft lattice, which can adopt strains by lattice deformation,[33] the lattice deformation modulates the band energy structure possibly in an undemanding way, and the accumulated strain can induce defects to release stress at a certain point,[34] which is critical

to performance reliability and structure stability in the long term. Therefore, understanding the origin and the effect of multi-dimensional lattice strain in perovskite film is extremely important in terms of deriving the maximum potential of optoelectronic properties as well as ensuring performance reliability and structural stability in various electronic devices. In this review paper, we discuss the origin of lattice strain from the nanoscale, spatially localized in a nanodomain, to the bulk scale (submicrometer). Characterization methods generally used to assess lattice strain is introduced, along with their validity and limitations. More importantly, we thoroughly investigate various strategies to regulate the residual lattice strain in bulk film by categorizing various approaches. This comprehensive review will not only provide an understanding of the origin-and-effect relationship but also provide a feasible insight to regulate the crystallization and design relevant interfaces based on the effective experimental strategies in terms of strain control. According to recent progress, FAPbI$_3$ is of general interest as the composition of perovskite in this study although MAPbI$_3$ and other compositions are also discussed in terms of fundamental strain studies.

2. Local strain on the atomic scale

It is apparent that FAPbI$_3$ has taken the majority of the perovskite composition, particularly for PSCs with a single junction.[22] FA$^+$ cation plays a role in maintaining charge neutrality within the lattice by being located in the center of voids surrounded by eight PbI$_6^{4-}$ octahedral Conner-sharing cages.[35,36] Moreover, FA$^+$ stabilizes the lattice by nearly satisfying the ideal Goldschmidt tolerance factors ($t = 1$), where the geometrical steric effect is minimized.[37] FA$^+$ exhibits a larger size, compared to MA$^+$,[38] with hydrogen bonding sites at the opposite sides of the molecule,[39] which contributes to a strong interaction with anionic inorganic frameworks.[40] FAPbI$_3$ is generally known as a cubic structure (α-phase with space group of $Pm\bar{3}m$) at room temperature with isotropic motion of FA$^+$ freely rotating in the PbI$_6^{4-}$ inorganic network.[41] As shown in Fig. 1(a), the high symmetry of a cubic structure undergoes phase transition to tetragonal (β-phase at 266 K) and orthorhombic (γ-phase at 153 K) with decreasing temperature,[42] where the PbI$_6^{4-}$ octahedral tilting is enhanced, coupled with suppression of the dynamic motion of FA$^+$.[10] Cubic structure corresponds to a^{0}a^{0}a^0 of Glazer notation, indicating high symmetry in terms of the average position of atoms. Although the high symmetry of a cubic structure would remind us of negligible strain in lattice based on neither octahedral rotation nor Pb^{2+} off-centering, appreciable PbI$_6^{4-}$ sublattice vibration and FA$^+$ rotation is accompanied by thermal ellipsoids in a high frequency range (THz),[30,31] opening up the local cage distortion and octahedral tilting in a high symmetry structure. It is further proposed that the lone pair orbitals of Pb^{2+} can encourage stereochemically off-center motions in the lattice,[43,44] being distinguished from FA$^+$ molecular dynamics mainly as the entropic thermal driving force.[45,46] Such a static distribution

Hui-Seon Kim is an Associate Professor at Inha University, Korea. Her research interest focus on energy materials and devices, including PSCs, since her first paper on solid-state PSCs in 2012. She received her BEng from the School of Chemical Engineering at Sungkyunkwan University (SKKU), Korea, in 2011. She then received her PhD from the Department of Energy Science at SKKU under the supervision of Prof. Nam-Gyu Park in 2016. She started her professional career as a postdoctoral researcher under Prof. Anders Hagfeldt at École Polytechnique Fédérale de Lausanne, Switzerland (2016–2019) and moved to the Department of Chemistry at Inha University as an Assistant Professor (2019–2023).

Hui-Seon Kim

This journal is © The Royal Society of Chemistry 2025

Chem. Soc. Rev., 2025, 54, 7870–7912 | 7871

of different low-symmetry local motif, enabled by different displacement of Pb^{2+}, tilting angle, and rotation with respect to local octahedra in cubic structure, strongly indicates a polymorphous network,[43] which is in accordance with extensive discussions that the experimentally emerging physical feature of the cubic structure reflects spatial-dependent inhomogeneity. However, macroscopically averaged (fictitious monomorphous) cubic unit cells are generally assumed to fit the X-ray diffraction pattern owing to a relatively long coherence length of X-ray diffraction[44,47–49] although the property of the high symmetry (monomorphous) cubic structure would certainly differ from the properties of either the broken symmetry cubic structures (local structural motifs with low symmetry) or the macroscopically averaged polymorphous structures.[43] To this end, space-resolved analysis techniques on the nanoscale are frequently used to examine the local structure. $MAPbBr_3$ nanocrystals with a cubic structure, for example, exhibit 1–2 nm sized local domains with distinctly different orientations of MA^+ from high-resolution transmission electron microscopy (HR-TEM).[50] The local strain induced in the polymorphous network in a single formula unit can become more complicated in the mixed composition by doping. It is well known that an undesirable phase transition from cubic (α-phase) to non-perovskite hexagonal phase (δ-phase with space group of $P6_3/mmc$) occurs owing to the lower minimum in Gibbs free energy (G, $\Delta G = \Delta H - T\Delta S$, where H, T, and S denote enthalpy, temperature, and entropy, respectively) of δ-phase at ambient temperature (below 285 K^{51}–350 K; as shown in bottom of Fig. 1(a)).[52] The metastable α-phase can be kinetically trapped by an energy barrier (activation energy) between α- and -δ phases. Mixed-cation (MA^+ and/or Cs^+) and/or -anion (Br^-) system with smaller radii compared to FA^+ and I^- is frequently adopted for $FAPbI_3$ to enhance thermodynamic stability by lowering the minimum of G not only by increasing S based on an increased lattice disorder but also by decreasing H based on a unit cell contraction, which accordingly increases the energy barrier for α-to-δ transition and thus effectively retards the transition kinetics.[10,53] Therefore, the doping strategy prevails in the $FAPbI_3$ lattice,[54,55] which inevitably alters the local lattice strain, as illustrated in Fig. 1(b) and (c). The breaking of local symmetry, mainly reflected in octahedral tilting, governs local strain. Larger amplitude octahedral tilts are generally responsible for larger strains in the crystal.[56] Consequently, the local strain is inherent to the local chemical bonding environment along the inorganic framework, which enables the manipulation of the local electronic band structure and structural stability.

3. Local strain on sub- and super-grain scales

Although the polymorphous network on the atomic scale would grant a macroscopically averaged structure, there still exists local strain on sub-grain and super-grain scales. Grains in perovskite film are usually identified by scanning electron microscopy (SEM) according to morphological criteria, which frequently and partially neglect crystallographic information. Nanodomains, according to structural criteria within a single grain, are specifically analyzed by the spatial crystal orientations or the spatial optoelectronic properties.[60–63] Ultrasensitive electron backscatter diffraction (EBSD) is a useful technique for the acquisition of structural inhomogeneity by mapping the local crystal orientations of perovskite when minimizing the beam-induced damage.[64] Fig. 2(a) depicts the surface SEM image of $MAPbI_3$ film, while Fig. 2(b) shows the inverse pole figure (IPF) map, obtained by EBSD, of the same region with the SEM image. The black arrow in the SEM image is aligned to cross a single grain boundary based on the morphological perspective (Fig. 2(a)), while the three distinct boundaries exist to separate four different crystal orientations according to the IPF map (Fig. 2(b)), where the separated domains are indexed by 1-4, matching the depicted orientations in Fig. 2(c). This implies that the so-called grains defined by SEM are likely to be composed of smaller domains in terms of structural orientation.[60] Similarly, the IPF map depicted in Fig. 2(d) is converted to individual grains (Fig. 2(e)) determined by crystal orientation based on a threshold of 4° for crystal misorientation. The assigned grain is represented by a united color corresponding to its mean orientation. The color contrast with respect to grains accordingly implies the existence of appreciable local structural heterogeneity in the perovskite film. As depicted in Fig. 2(f), the grain orientation spread (GOS) is indicated by the average deviation in the crystal orientation between each point within a single grain and the mean orientation of the grain. The GOS ranges from 0° (perfectly ordered structure within a grain) to 4.3° (certain structural inhomogeneity within a single grain), strongly proposing a different degree of local strain residing in grain-to-grain. Therefore, when considering that the local variation in structural orientation determines local strain heterogeneity, a higher lattice strain is expected from the high GOS, while the minimized lattice strain is assumed on the grain scale from the 0° of the GOS.[65]

The structural inhomogeneity at the sub-grain level is monitored within a single grain, defined by crystal orientation.[60] Sub-grain boundaries, satisfying the equal threshold of 4°, exist as indicated by the solid line illustrated in Fig. 3(a). However, Fig. 3(b) depicts point-dependent misorientation with respect to the mean orientation of the corresponding grain, which demonstrates that a significant strain heterogeneity resides even in individual grains of $MAPbI_3$ ranging from 0° to exceeding 6°. It is noted that the region closer to the grain boundary exhibits a higher misorientation angle, which indicates a higher degree of lattice deformation near the grain boundaries. Structural inhomogeneity becomes more exaggerated when estimating the misorientation angle between two extreme points in the same grain. Fig. 3(c) depicts the intra-grain misorientation angle by line mapping across the single grain (black arrow in the inset figure), where the misorientation angle reaches 9° between one end and the other end due to steadily varied crystal orientation. The local lattice imperfections induced by a sudden structural change in the ordering
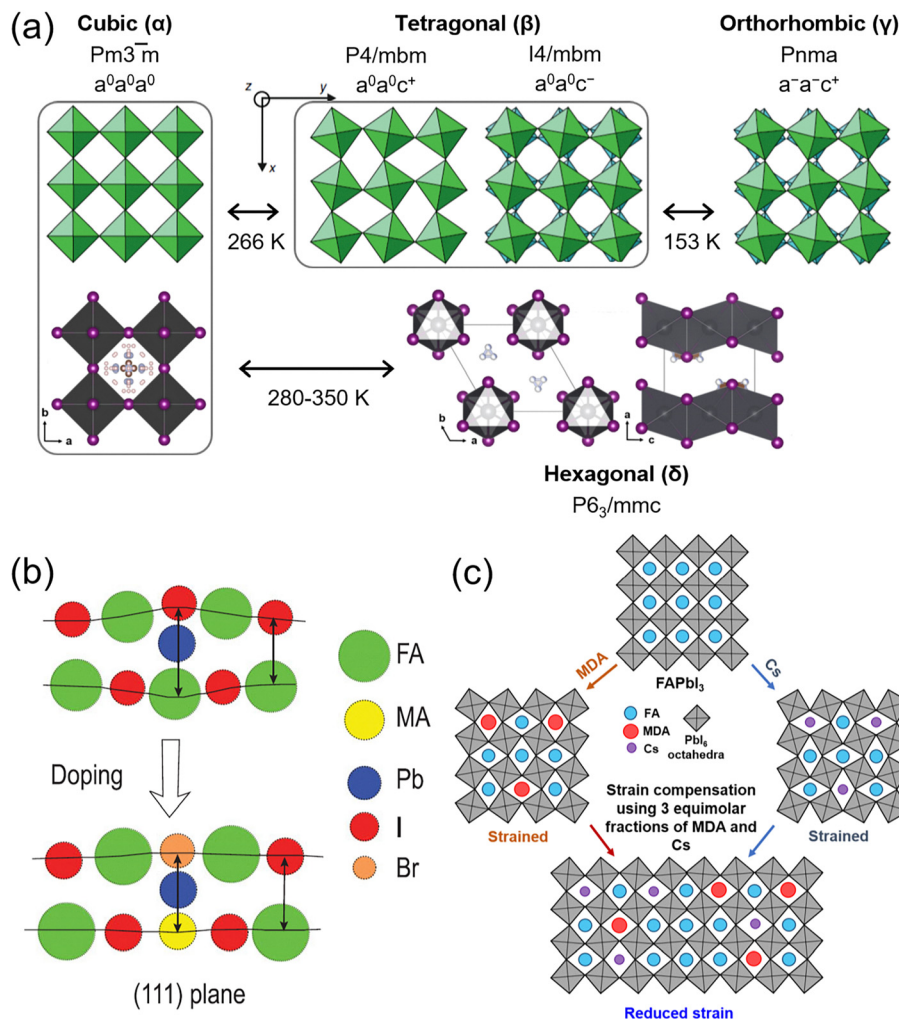
Fig. 1 (a) Phase transition of FAPbI$_3$ depending on temperature. Reproduced with permission from ref. 57. Copyright 2016, Wiley–VCH. (b) Schematic of local strain changes in FAPbI$_3$ by employing MA$^+$ and Br$^-$. Reproduced with permission from ref. 58. Copyright 2021, American Chemical Society. (c) Schematic of local strain induced by incorporating methylenediammonium (MDA^{2+}), Cs$^+$, or MDA^{2+}/Cs$^+$ in FAPbI$_3$ crystal. Reproduced with permission from ref. 59. Copyright 2020, American Association for the Advancement of Science.

of the octahedral framework involve defects, which can act as non-radiative recombination centers,[66] as evidenced by PL response,[60] while the gradual strain change maintains lattice continuity with a spatially varied electronic band structure. Similarly, FAPbI$_3$ exhibits atomic-level inhomogeneity in crystal orientation.[67] Fig. 3(d) shows a TEM image of FAPbI$_3$, where the neighboring local regions indicated as 1-1, 1-2, and 1-3, corresponding to zoomed-in images in Fig. 3(e), represent the interplanar spacings of 0.29 nm along (210), 0.35 nm along (111), and 0.32 nm along (200), respectively. Furthermore, the local structure assigned as 1-4 presents 0.24 nm of interplanar spacing for (300) of PbI$_2$, indicating a partial decomposition. The distinct variation in local crystal orientation, as illustrated in Fig. 3(f), consequently induces lattice strain and thus lowers the uniformity of lattice-level electronic properties.

In addition, structural coherency in super-grain is notably monitored from a single formula (almost phase-pure) of halide

perovskite.[62] Nano- and micro-XRD with corresponding spatial resolution are utilized to analyze residual strain stemming from the structural inhomogeneity in MAPbI$_3$ polycrystalline film. Fig. 4(a) shows a quiver plot for the (110) orientation obtained by nanofocus XRD, where its azimuthal angle coordination is indicated by an arrow pointing direction with a corresponding color (inset color map) in each spatial diffraction spot. When considering the long-range cluster adjacent in both real and reciprocal space coordinates as super-grain, two super-grains are indicated with blue and red in Fig. 4(a). As expected from the earlier discussion on sub-grain strain inhomogeneity, local strain variation is similarly monitored within super-grains, as indicated by a structural inhomogeneity (q). Micro-XRD also reveals the long-range microstrain according to the William-son–Hall equation, where complex local heterogeneity ranging from 0.1 to 0.2% is present (Fig. 4(b)). The different degrees of microstrain would grant different local strain environments along the octahedral framework, leading to an inhomogeneous
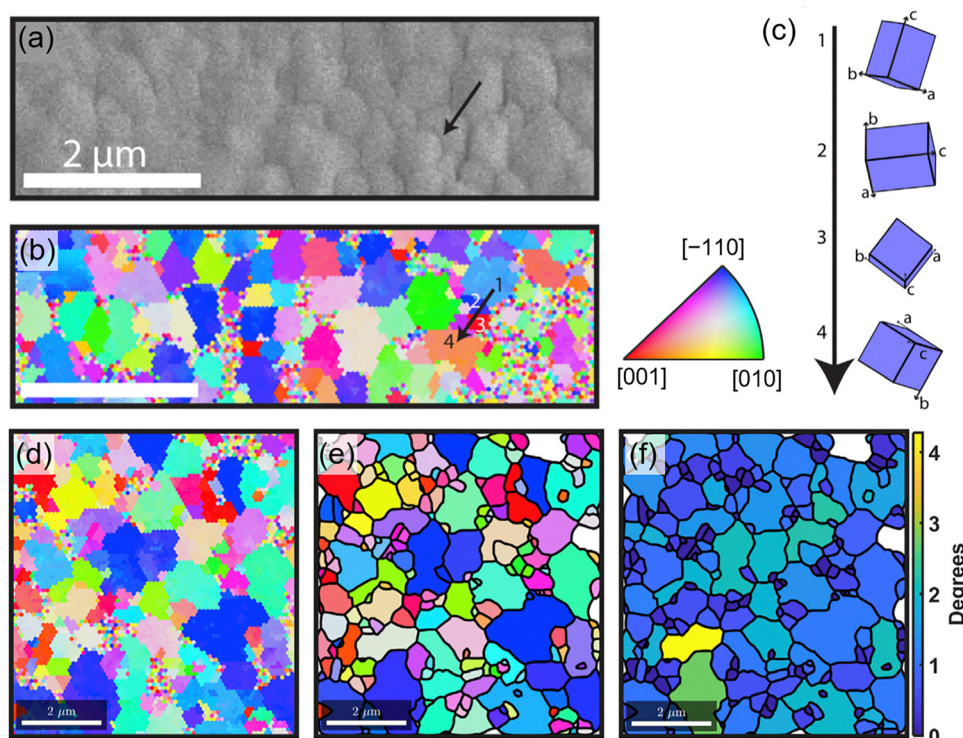
Fig. 2 (a) SEM image and (b) corresponding IPF map of the MAPbI$_3$ film generated by EBSD with a color code for facet orientation. (c) Depicted crystal orientation along the black arrows in (a) and (b). (d) Original IPF map, (e) conversion plot of grains identified from the IPF map with a threshold of 4° with an indication of mean orientation of the respective grains, and (f) conversion plot of GOS with an indication of average local misorientation. Scale bars in (a)−(f) represent 2 μm. Color cold for IPF mapping in (d)−(f) is the same as that in (b). Reproduced with permission from ref. 60. Copyright 2019, Cell Press.

photoluminescence response. Furthermore, the largest structural broadening by increasing local q (decreased interplanar spacing) from the correlation between microstrain and local q in Fig. 4(c) could imply compressive strain along the designated plane. Hence, a dimension of domain, which comprises a relatively uniform lattice configuration without a sudden breaking, can be widely varied from sub-grain level to super-grain level though the marginal local structural inhomogeneity is consistently inherent in the domain with different degrees.

Structural coherency is also governed by crystallographic orientation. The atomic-scale high-resolution Cryo-TEM image depicted in Fig. 5(a) reveals a well-aligned grain boundary between (211)- and (001)-oriented grains,[68] indicating a minimal accumulation of local strain at the (211)/(001) interface.[69] The corresponding fast Fourier transform (FFT) analysis in Fig. 5(b) further confirms the coherency of this grain boundary. In contrast, the convergence of (001)-oriented grains tends to form incoherent grain boundaries, as shown in Fig. 5(c) and (d), with dangling bonds, dislocations, and lattice mismatch, which are responsible for interfacial local strain.[70] Notably, the application of high Miller-index (211) facets to micron-thick FA-based perovskite films is effective in reducing dislocation density and local strain,[68] which highlights the importance of crystallographic orientation at grain boundaries in regulating interfacial lattice strain and in encouraging the structural coherency between adjacent grains toward super-grain.

4. Out-of-plane strain inhomogeneity across bulk film

4.1. Doping (mixed-composition effect)-induced strain inhomogeneity

Based on morphological identification, almost no horizontal grain boundaries in parallel with the substrate are evidenced by the cross-sectional SEM images of state-of-the-art high-performing perovskite films,[71,72] indicating a single grain along the out-of-plane direction, while vertical grain boundaries separate grains along the in-plane direction from the cross-sectional view. Even though the cubic structure underlies a negligible difference between out-of-plane and in-plane directions, a distinctive structural inhomogeneity along the out-of-plane is observed within a single grain (sub-grain level), particularly in the mixed-composition system with a doping strategy to stabilize the α-phase of FAPbI$_3$ or to achieve the wide bandgap material based on the mixed halide system (APbI$_{3-x}$Br$_x$).[73,74] As depicted in Fig. 6(a) a perovskite film with mixed composition of FA$_{0.85}$MA$_{0.15}$Pb(I$_{0.85}$Br$_{0.15}$)$_3$ represents a gradient of (004) interplanar distance along the vertical direction on sub-grain level by decreasing from 1.67 Å (local region III near bottom) to 1.64 Å (local region II at middle) and 1.60 Å (local region I near top surface), which is attributed to the depth-dependent gradient distribution of MA$^+$, as evidenced by time-of-flight secondary ion mass spectrometry depth profiles,[27] probably owing to the

7874 | *Chem. Soc. Rev.*, 2025, **54**, 7870–7912

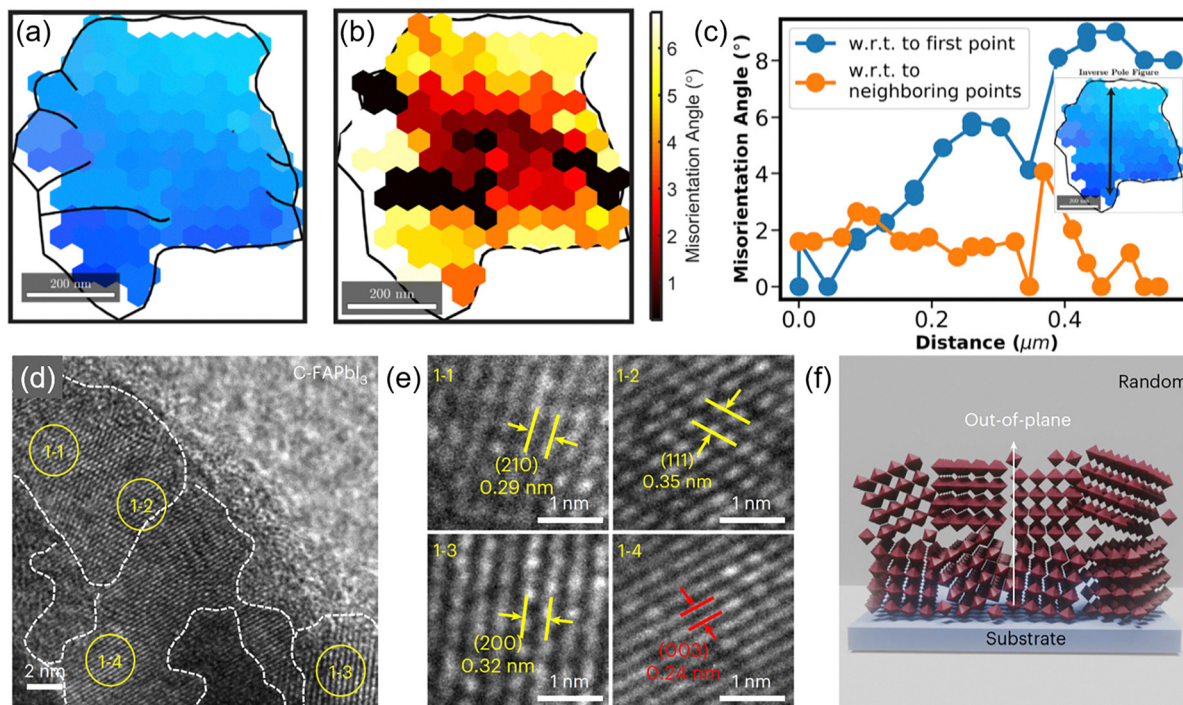This journal is © The Royal Society of Chemistry 2025

Fig. 3 (a) IPF of an individual grain (outer black line) in MAPbI$_3$ with sub-grain boundaries (inner black lines). (b) Misorientation angle with respect to the mean orientation of a single grain. Scale bars in (a) and (b) represent 200 nm. (c) Plot of misorientation angle with respect to the first point (blue symbols) and its neighboring points (orange symbols) along the line mapping (the black arrow in the inset figure). Reproduced with permission from ref. 60. Copyright 2019, Cell Press. (d) HR-TEM image of FAPbI$_3$ film. (e) High-magnification HR-TEM images of different spots (1-1 to 1-4 as indicated in (d)) of FAPbI$_3$ film. The red lines and arrows in (e) indicate the (003) facet of PbI$_2$ generated by perovskite decomposition. (f) Schematic of the crystalline film of FAPbI$_3$. Reproduced with permission from ref. 61. Copyright 2025, Springer Nature.

difference in coordination strength between FA$^+$ and MA$^+$ during the film growth. Similarly, FA$_{1-x}$Cs$_x$PbI$_3$ shows the out-of-plane cation inhomogeneity within a single grain, as illustrated in Fig. 6(b).[74] Cs$^+$-rich region is frequently observed near the bottom, resulting in 3.11 Å for (200) interplanar spacing, which is gradually decreased toward the top surface, leading to FA-rich composition with an enlarged (200) interplanar spacing of 3.20 Å (Fig. 6(c)). Although Cs$^+$ is frequently incorporated to improve the phase stability of α-FAPbI$_3$,[75] the rapid crystallization in the presence of Cs$^+$ inevitably results in an inhomogeneous distribution across the film.[74] To this end, the incorporation of Rb$^+$ is found to be highly effective on more uniform distribution across the film with a mixed-composition system based on quadruple cations (FA$^+$, MA$^+$, Cs$^+$, and Rb$^+$) and triple halides (Cl$^-$, Br$^-$, and I$^-$). The improved distribution of Cs$^+$ and the suppressed halide segregation are evidenced by employing Rb$^+$,[76,77] as confirmed by the relatively depth-independent halide distribution depicted in Fig. 6(d) and (e).[76] The incorporation of Rb$^+$ promotes more homogeneous distribution of Cs$^+$ and halides throughout the perovskite film, which is definitely favorable for mitigating the lattice strain inhomogeneity along the out-of-plane direction, as evidenced by GIXRD results. Although an apparent peak shift in 2θ is observed in the absence of Rb$^+$ from 28.66° to 28.56° with increasing ω from 0.3° to 4.0° (Fig. 6(f)), Rb$^+$ induces a negligible shift in 2θ (Fig. 6(g)), indicating the enhanced lattice strain homogeneity along the out-of-plane direction.[76] Similarly, the

sub-grain level inhomogeneity of local strain in the doped-perovskite film should be carefully assessed by differentiating out-of-plane from in-plane owing to a possible gradient for cation and/or anion distribution along the out-of-plane direction.

4.2. Processing (thermal effect)-induced strain inhomogeneity

The perovskite film is generally grown based on a solution process.[78] Therefore, crystal growth is inevitably governed by solvent evaporation during the annealing process, where an anisotropic solvent evaporation and a difference in thermal expansion coefficient between rigid substrates and soft halide perovskite materials are considered the main reasons for strain inhomogeneity along the out-of-plane direction during the process.[37,58,79] More specifically, the annealing process for the perovskite crystallization is frequently performed using a simple hot plate, which makes it difficult to guarantee a negligible temperature gradient across the loaded precursor between the bottom and the open top. A difficulty in controlling uniform solvent evaporation could induce different crystallization kinetics between the surface and bulk region, which imposes even more complexity when employing additives in the precursor solution. During the annealing process, the PbI$_6^{4-}$ inorganic framework near the bottom is prone to have a more expanded structure, while the lattice near the top surface has a

This journal is © The Royal Society of Chemistry 2025
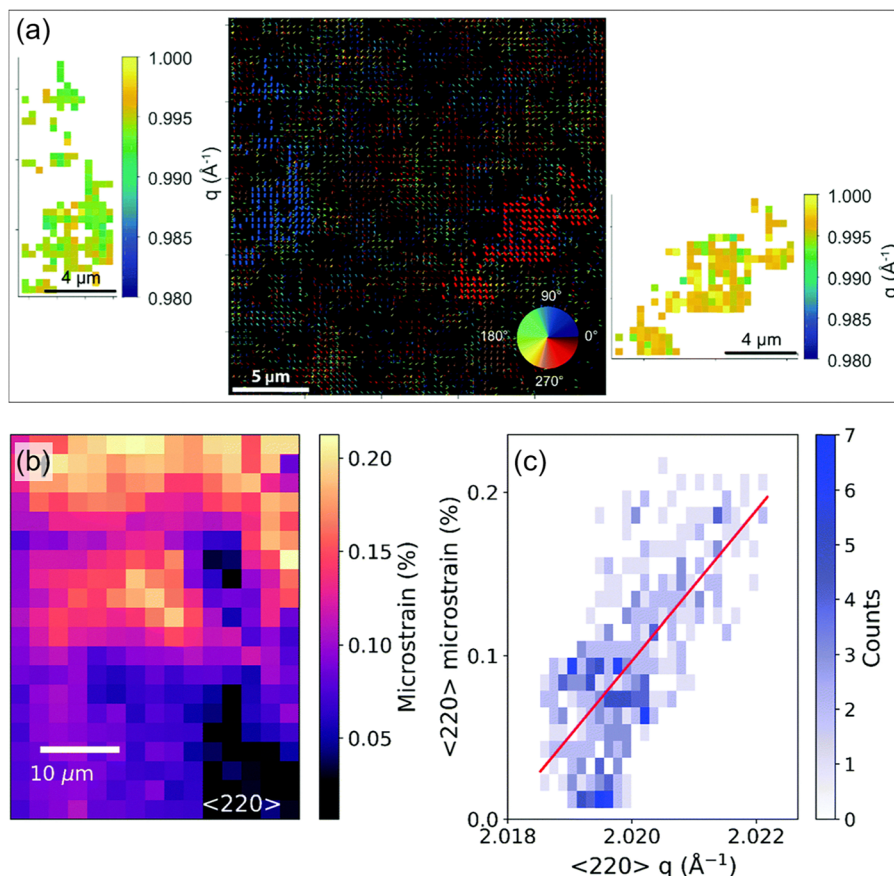
Chem. Soc. Rev., 2025, 54, 7870–7912 | 7875

Fig. 4 (a) Quiver plots generated by nano-XRD measurements of the MAPbI$_3$ film demonstrate two large super-grains along the (110) direction, highlighted in blue (left) and red (right), with local variations in the scattering vector q extracted from the respective super-grains. (b) Microstrain map for the (220) diffraction peak in the MAPbI$_3$ film. (c) Histogram of the microstrain as a function of the scattering vector q for the (220) diffraction peak. The solid red line indicates a linear regression fit to a scatter plot of the data, confirming the correlation. Reproduced with permission from ref. 62. Copyright 2019, Wiley-VCH.

relatively contracted volume owing to the temperature gradient, which increases the chance of larger cations being employed in the bottom.[27] This can further complicate the aforementioned compositional inhomogeneity along the out-of-plane direction. Most importantly, a substantial difference in thermal coefficient by an order of magnitude ($\sim 10^{-5}$ K^{-1} for rigid metal oxide substrates and $\sim 10^{-4}$ K^{-1} for soft organic–inorganic halide perovskite) consequently involves a substantial difference in lattice contraction when cooling from the higher annealing temperature for crystallization.[25,80,81] During the crystallization at higher temperature (*ca.* 100–150 °C), the perovskite lattice is anchored to the underlying substrate, while the strong adhesion between the perovskite and the substrate constrains the perovskite from contracting during cooling to room temperature. The severe constraints of lattice contraction introduce the in-plane biaxial tensile strain, where the most pronounced in-plane tensile strain resides in the bottom region of the perovskite film, while the relatively reduced in-plane tensile strain is applied near the open top, being far away from the substrate.[27] The different degrees of in-plane tensile strain along the out-of-plane direction leads to a vertical gradient in in-plane tensile strain, which is responsible for the strain inhomogeneity along the out-of-plane direction.[25,27,78] It is noticeable that the out-of-plane strain inhomogeneity ranges across the whole bulk film, which is a collective strain on a bulk scale unlike various anisotropic local strains on the nanoscale.

5. Strain inhomogeneity by external stress

The lattice strain in perovskite films is also affected by external environmental factors, such as illumination, moisture, and aging effects. Under illumination, lattice expansion generally occurs in halide perovskite film, where the lattice strain is accordingly alleviated in the expanded unit cell.[82] Nevertheless, the effect of halide phase segregation under illumination can further complicate the local lattice strain. The interaction between phonon and charged entities (usually photogenerated free carriers) induces the local strain by forming a polaron-to-screen charge in the lattice.[83] The polaronic strain can markedly initiate the phase segregation for mixed I$^-$ and Br$^-$, which can be rather restrained by composing a uniform and homogeneous distribution of local polaronic strain under high

7876 | *Chem. Soc. Rev.*, 2025, **54**, 7870–7912

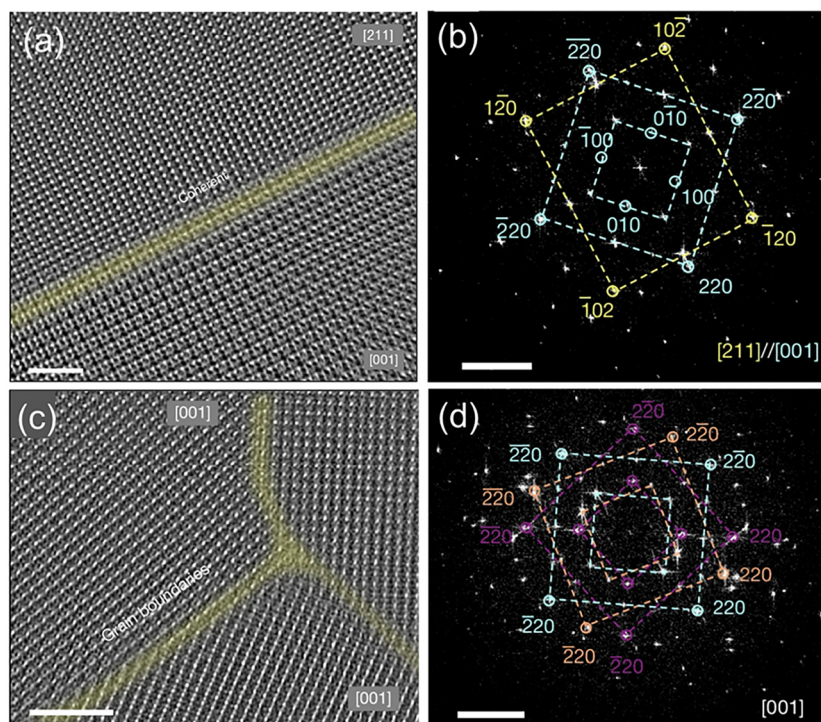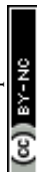This journal is © The Royal Society of Chemistry 2025
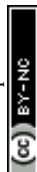
Fig. 5 (a) Atomic-scale Cryo-TEM image of a coherent grain boundary, indicated in light orange, at the interface between (211)- and (001)-oriented perovskite grains. (b) FFT patterns corresponding to the coherent grain boundary along the (211) and (001) zone axes. (c) Cryo-TEM image of regular incoherent grain boundaries, indicated in light orange, and (d) the corresponding FFT patterns between three (001) perovskite grains. Reproduced with permission from ref. 68. Copyright 2025, Springer Nature.

carrier density.[84] The structural instability under illumination is suppressed in terms of a mechanical perspective. A graphene–polymer complex, coordinating on the perovskite surface, can mechanically limit structural deformation and thus effectively mitigate lattice distortion.[85] In addition, halide perovskite films are forced to experience periodic strain alteration during diurnal cycles. Although the lattice strain is mitigated under continuous illumination, the lattice contraction under dark conditions induces a structural reversion to a more asymmetric structure with reinforced lattice strain.[80,82,86] The repetitive strain dynamics can afford to facilitate the formation of deep trap states and potentially accelerate chemical degradation.[87] The incorporation of additives, which can coordinate with Pb^{2+} on the surface, enables the interfacial anchoring at grain boundaries and effectively suppresses the lattice volume fluctuations.[88] Furthermore, the decomposition of the perovskite film is frequently initiated by moisture ingress through the grain boundaries, which act as diffusion pathways for water molecules to penetrate the bulk of the film.[89,90] The moisture subsequently propagates laterally along the crystal planes and leads to a local misorientation and the generation of localized lattice strain,[60,89] suggesting a coupled relationship between lattice strain and moisture-induced degradation. Besides, the aging process of perovskite films often results in changes in the lattice strain.[91] The addition of MACl to $FAPbI_3$ films is generally adopted to ensure high film quality of α-$FAPbI_3$, where the slow removal of Cl^- from the perovskite

film during the so-called 'aging process' is responsible for lattice strain relaxation, leading to an improved PCE after aging.[91]

6. Characterization of out-of-plane strain inhomogeneity across bulk films

Although the local strain and its inhomogeneity are generally assessed by various local mapping analysis techniques with high resolution focusing on the target region,[92,93] strain measurements in terms of the collective bulk film scale have been most widely performed.[94] It is meaningful because the collective strain across the whole bulk film can be more intuitively and directly linked to the device performance. The grazing incidence X-ray diffraction (GIXRD) can reflect the information of in-plane lattice distance, which is suitable for assessing the depth-dependent in-plane strain, while the micro strain, usually estimated by normal XRD, can indicate the deviation extent of interplanar spacing, assuming that the local structural randomness contributes to the strain inhomogeneity along the out-of-plane direction.[95] GIXRD is the most routinely adopted method for assessing lattice strain because depth-dependent in-plane strain distinctly prevails in solution-processed halide perovskite films,[96,97] which is often complemented by HR-TEM to evidence the real lattice distances depending on the depth from the cross-sectional device.[98]
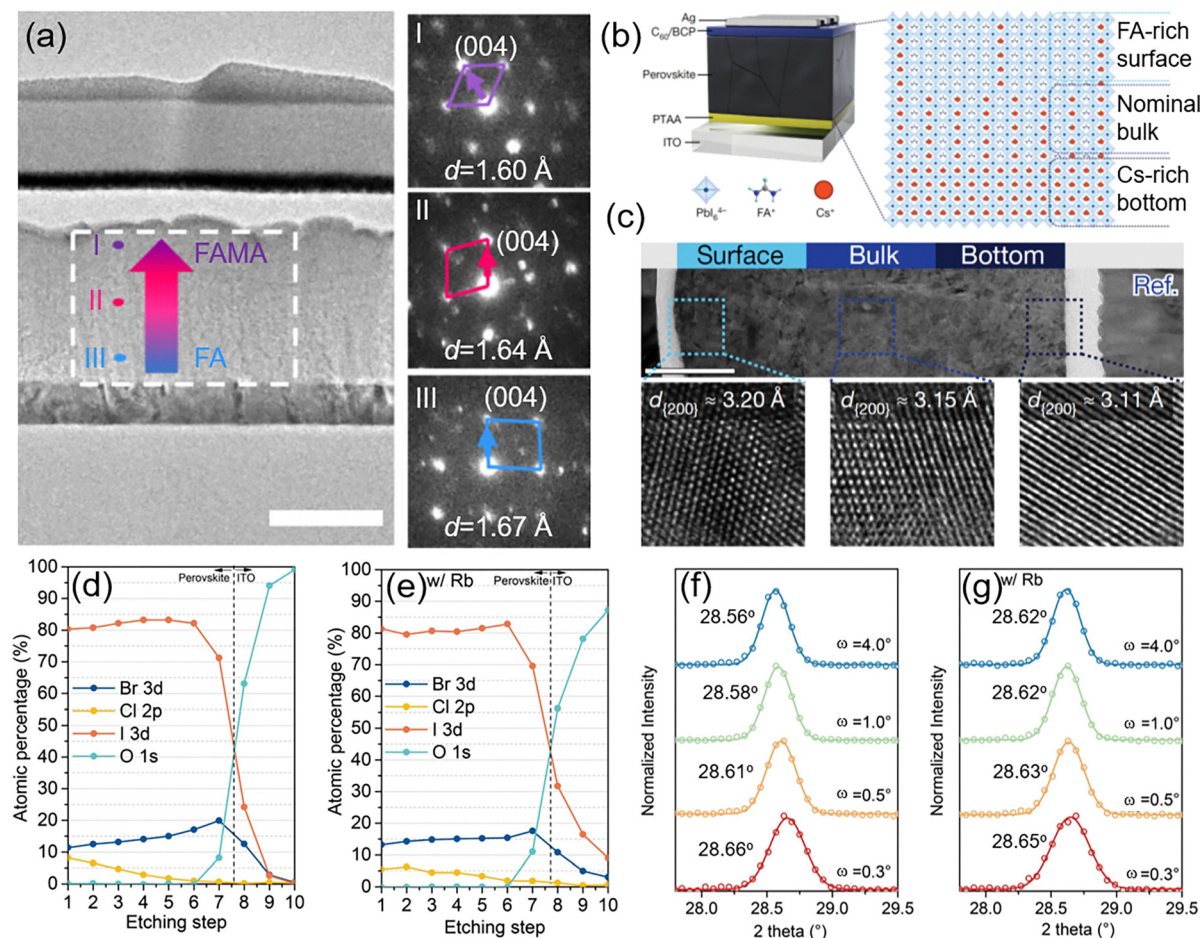
This journal is © The Royal Society of Chemistry 2025

Chem. Soc. Rev., 2025, **54**, 7870–7912 | **7877**

Fig. 6 (a) Cross-sectional TEM image and depth-dependent nano-beam electron diffraction patterns of the $FA_{0.85}MA_{0.15}Pb(I_{0.85}Br_{0.15})_3$-based device. Reproduced with permission from ref. 27. Copyright 2019, Springer Nature. (b) Illustration of the inhomogeneous phase distribution along the out-of-plane of the $FA_{1-x}Cs_xPbI_3$ film. (c) Cross-sectional high-angle annular dark-field TEM images (200 nm for the scale bar) and depth-dependent HR TEM images (7.3 × 7.3 nm) of $FA_{1-x}Cs_xPbI_3$. Reproduced with permission from ref. 74. Copyright 2023, Springer Nature. Depth profile XPS results of oxygen and halides in perovskite film (d) without and (e) with Rb^+. GIXRD patterns with varying ω for the perovskite film (f) without and (g) with Rb^+. Reproduced with permission from ref. 76. Copyright 2025, American Association for the Advancement of Science.

6.1. GIXRD

Normal XRD can selectively recognize the crystal planes in parallel with the sample surface, implying the limited acquisition of crystal information on the planes perpendicular to the sample surface. Therefore, the structural in-plane information, in parallel with the sample surface (*i.e.*, interplanar spacing along the in-plane direction), is effectively restricted in the normal XRD pattern. However, GIXRD enables the in-plane structural information to be reflected, coupled with an out-of-plane response.

6.1.1. Penetration depth. Fig. 7 illustrates the geometric relationship between the X-ray beam and the sample with defined angles in normal XRD and GIXRD. Although the normal XRD is based on either θ–θ (left side of Fig. 7(a)) or θ–2θ (right side of Fig. 7(a)) scan modes, the GIXRD pattern is obtained by moving a detector to sweep 2θ with a fixed incidence angle (α_i) of the X-ray beam (Fig. 7(b)).[99] The penetration depth (z) of the X-ray beam from the surface is then determined by α_i, where a small α_i allows the shallow depth

near the surface is then determined by XRD response while excluding the remaining deeper region below z,[100] as illustrated in Fig. 7(c).

The diffracted intensity (I_d) of the X-ray beam can be driven by the attenuation of the incidence intensity (I_0) according to eqn (1), where μ is the attenuation coefficient (or linear absorption coefficient) of the material, L_1 is the path length ($L_1 = z/\sin \alpha_i$), L_2 is the path length at the diffracted side ($L_2 = z/\sin(2\theta - \alpha_i)$), and 2θ is the Bragg angle.[99]

$$I_d = I_0 \cdot e^{-\mu(L_1 + L_2)} = I_0 \cdot e^{-\mu\left(\frac{z}{\sin \alpha_i} + \frac{z}{\sin(2\theta - \alpha_i)}\right)}. \tag{1}$$

The z is defined as a specific depth at which I_d is reduced by e^{-1} ($\sim$37%) from the original intensity, I_0, under given parameters of μ by material ($\mu = \sim 10^3$ cm^{-1} for FAPbI$_3$ with 1.54 Å of Cu K$_\alpha$)[102–104] and α_i by setting input.[105] In other words, z is a function of α_i, as depicted in eqn (2), confirming a shallow z as

7878 | *Chem. Soc. Rev.*, 2025, **54**, 7870–7912

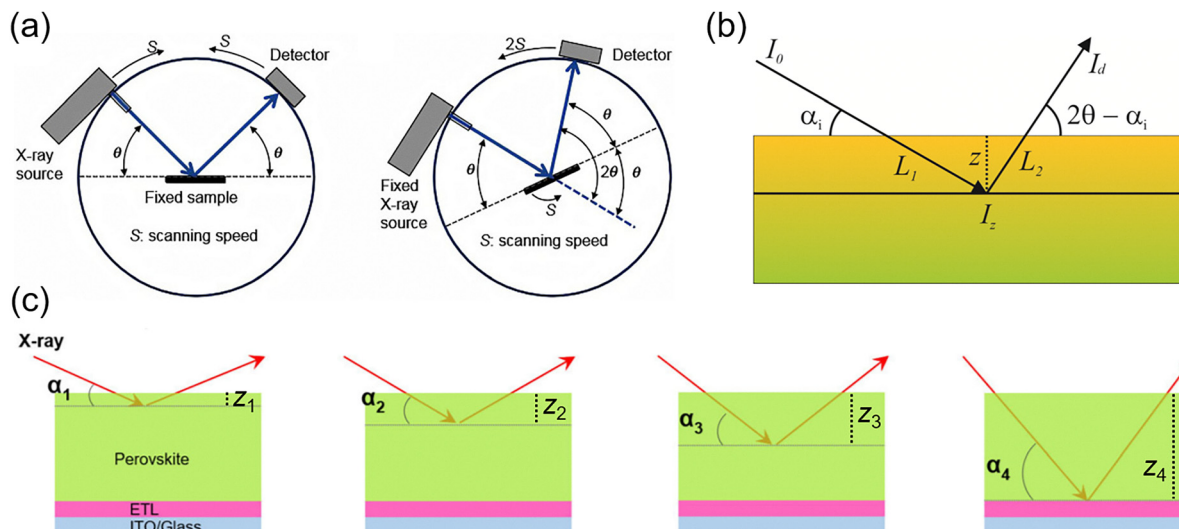This journal is © The Royal Society of Chemistry 2025

Fig. 7 (a) Basic principle of θ/θ (left) and $\theta/2\theta$ (right) goniometers of the normal XRD. Reproduced with permission from ref. 101. Copyright 2016, Elsevier. (b) Illustration of XRD measurement in grazing incidence geometry (GIXRD). Reproduced with permission from ref. 99. Copyright 2016, Royal Society of Chemistry. (c) Illustration of α_i-dependent z ($\alpha_1 < \alpha_2 < \alpha_3 < \alpha_4$ and $z_1 < z_2 < z_3 < z_4$) in GIXRD characterization. Reproduced with permission from ref. 100. Copyright 2023, Springer Nature.

α_i decreases.[99]

$$z = \frac{1}{\mu}\left(\frac{1}{\sin \alpha_i} + \frac{1}{\sin(2\theta - \alpha_i)}\right)^{-1}. \qquad (2)$$

6.1.2. Residual in-plane lattice strain measurements. Polycrystalline material, such as halide perovskite, consists of (hkl) planes oriented exactly parallel to the substrate and oriented in various directions. GIXRD enables the interplanar spacing (d) of randomly oriented (hkl) planes in polycrystalline thin films to be systematically measured by modulating the tilt angle, Ψ, between the crystalline plane normal (L_3-axis; vertical to the (hkl) crystalline) and the surface normal (S_3-axis; vertical to the film surface), while maintaining a small α_i to ensure a limited z, as shown in Fig. 8(a) and (b).[106] From the perspective of residual lattice strain, d of a specific (hkl) plane in a strained film can be simply compared with a reference d under the strain-free condition (d_0). The acquisition of the d of the (hkl) plane at a given Ψ (d_Ψ) estimates the strain (ε) by a comparison with d_0 according to eqn (3):[107]

$$\varepsilon = \frac{d_\Psi - d_0}{d_0}. \qquad (3)$$

There are two ways to make a difference in Ψ according to the tilting direction (either iso- or side-inclinations), which consequently vary z.[106] As depicted in Fig. 8(a), the iso-inclination method applies the same direction of α_i to Ψ, leading to the actual incidence angle (ω) as the sum of α_i and Ψ ($\omega = \alpha_i + \Psi$).[106] Since ω becomes larger with increasing Ψ despite the fixed α_i, a difference occurring in z makes the iso-inclination method suitable for measuring z-dependent ε. When iso-inclination is utilized for GIXRD measurements to analyze the residual strain of perovskite thin films, the plot is

generally represented in d–ω, as shown in Fig. 8(c). As depicted in Fig. 8(c), the d of the perovskite film (particularly for the control sample with a large slope) expands as ω increases from $0.8°$ to $2.4°$, implying that the d increases as it crosses the bulk perovskite film from the top surface to the bottom interface.[108] The positive slope of the d–ω plot, therefore, indicates more pronounced tensile strain near the bottom interface compared to the top surface,[94,108] which is in accordance with the strain tendency of the aforementioned processing-induced in-plane strain inhomogeneity along the out-of-plane direction. However, the marginal slope of the target film, which is close to zero, indicates a negligible depth-dependent tensile strain across the film. Fig. 7(b) illustrates the side-inclination method, where the Ψ is equivalent to the tilting of the Chi angle (χ).[106] As χ increases, the X-ray beam enters the sample at a steeper inclination and accordingly increases its path length within the material.[27] Therefore, a slight change in z is observed as χ varies.[21,27] The GIXRD measurement with the side-inclination method can assume the residual strain (σ) according to eqn (4),[109] suggesting a 2θ–$\sin^2 \Psi$ plot as a useful form to assume the strain, as shown in Fig. 8(d).

$$\sigma = -\frac{E}{2(1+\nu)}\frac{\pi}{180}\cot\theta_0 \frac{\partial(2\theta)}{\partial \sin^2 \Psi}, \qquad (4)$$

where E is the Young's modulus, ν is the Poisson's ratio, and θ_0 is the diffraction peak position under the strain-free condition. Therefore, the slope of the 2θ–$\sin^2 \Psi$ plot implies the strain type with a negative slope ($\sigma > 0$) for tensile strain and a positive slope ($\sigma < 0$) for compressive strain within the film. Fig. 8(d) is obtained by sweeping Ψ from $15°$ to $60°$ by fixing α_i as $0.2°$,[110] showing a decrease in 2θ with increasing Ψ ($\sin^2 \Psi$).[110] Since θ is inversely proportional to d according to Bragg's law and Ψ is proportional to z, the negative slopes imply enlarged d near the

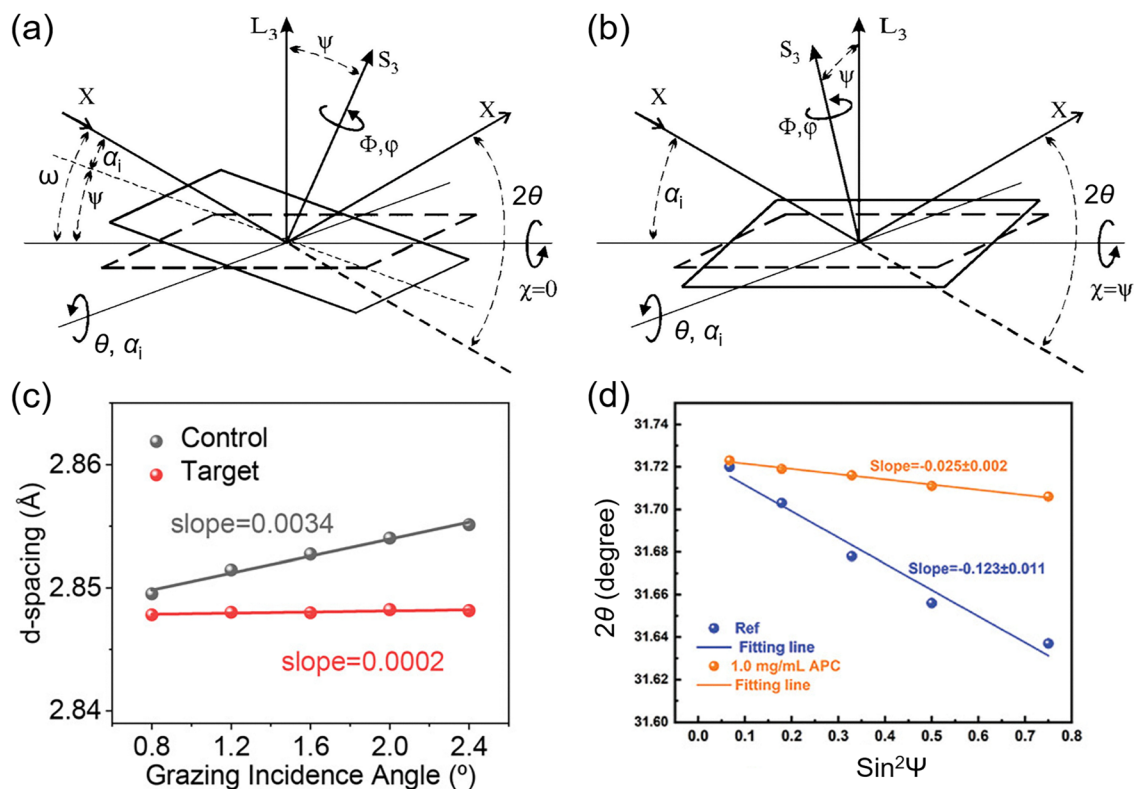This journal is © The Royal Society of Chemistry 2025

Chem. Soc. Rev., 2025, **54**, 7870–7912 | **7879**

Fig. 8 (a) Iso-inclination method tilting the sample (tilting angle = Ψ) in the same direction with α_i (χ = 0) along the axis for 2θ and α_i variation. (b) Side-inclination method tilting the sample (tilting angle = $\Psi = \chi$) along the axis perpendicular to the sample normal direction (S_3) and diffraction vector (L_3). Reproduced with permission from ref. 106. Copyright 2005, International Union of Crystallography. (c) Typical $d-\omega$ plot achieved from iso-inclination method-based GIXRD patterns with linear fittings. Reproduced with permission from ref. 108. Copyright 2025, American Chemical Society. (d) Typical $2\theta-\sin^2\Psi$ plot achieved using side-inclination method-based GIXRD patterns with linear fittings. Reproduced with permission from ref. 110. Copyright 2024, Wiley-VCH.

bottom interface of the perovskite film (with deep penetration of the X-ray beam) compared to the top surface. This is further in accordance with the residual in-plane tensile strain, which originates from the routine annealing process of perovskite films. As depicted in Fig. 8(d), the target film indicated in orange exhibits a relatively flat negative slope compared to that of the control film shown in blue, implying the released in-plane tensile strain with strain inhomogeneity to a lesser extent along the out-of-plane direction.

Many studies have exclusively relied on the GIXRD characterization to evaluate the residual lattice strain in halide perovskite films because the processing-induced strain generally originates from the interface and accordingly leads to the depth-dependent in-plane tensile strain, exhibiting a difference along the out-of-plane direction across the film. When considering that the variation in ω or χ enables the crystal information within different depths to be probed,[101,111] it seems suitable for this purpose. However, one should be careful in interpreting GIXRD patterns owing to the acquisition of (hkl) along different orientations by varying ω or χ. More specifically, the response of a particular orientation, satisfying ω (α_i), among randomly oriented (hkl) planes in a polycrystalline film is often referred to as 'in-plane' to indicate depth-dependency.[27,102,112] Therefore, the assessment of strain inhomogeneity along the

'out-of-plane' direction by GIXRD is difficult, as a sample resembles a perfectly ordered single crystal.

6.2. Microstrain

Fig. 9(a) illustrates the change in the XRD peak depending on the lattice strain.[104] Under the strain-free condition (no strain), the Bragg peak appears at $2\theta_0$, corresponding to d_0. In the second row, a uniform strain changes d, which results in a peak shift to satisfy Bragg's law ($\theta < \theta_0$ for tensile strain and $\theta > \theta_0$ for compressive strain).[113] However, nonuniform strain induces multiple peaks from different d, where the overlap of multiple peaks at close 2θ generates a broad peak.[79] The peak width is quantified using the full width at half maximum (FWHM, β), where not only lattice micro strain (ε) but also crystallite size (D) and the instrument effect serve as parameters determining β.[114] Therefore, the adjusted FWHM ($\beta_{(hkl)}$) can be estimated by removing the instrument effect, making $\beta_{(hkl)}$ only dependent on the sample ($\beta_{(hkl)} = \beta_{\text{crystallite size}} + \beta_{\text{strain}}$).[115,116] Williamson–Hall method allows us to assess the effects of D and ε on $\beta_{(hkl)}$ using $D = K\lambda/(\beta_{\text{crystallite size}} \cos\theta)$ and $\beta_{\text{strain}} = 4\varepsilon \tan\theta$,[114,117] where K is the Scherrer constant of the material (0.89 for cubic structure[118]) and λ is the wavelength of the X-ray beam source (1.54 Å for Cu K$_\alpha$).[104] Therefore, the plot of $\beta \cos\theta - 4\sin\theta$ is a useful form to assume ε, as illustrated in eqn (5) and (6),

7880 | *Chem. Soc. Rev.*, 2025, **54**, 7870–7912

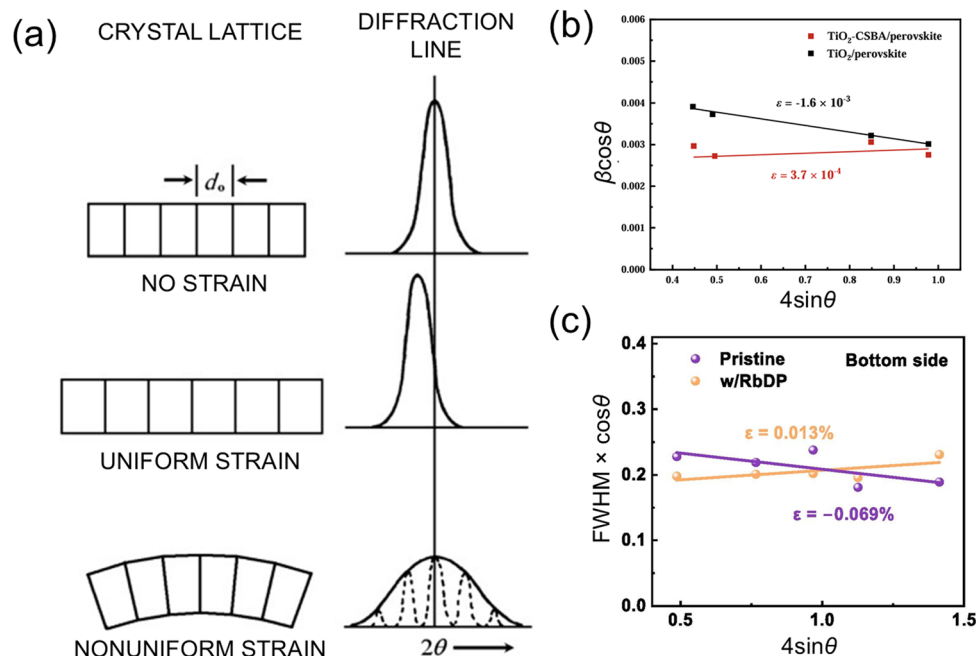This journal is © The Royal Society of Chemistry 2025

Fig. 9 (a) Schematic of the correlation between d in the crystal lattice and the resultant pattern of the diffraction peak. Reproduced with permission from ref. 104. Copyright 2011, Elsevier. (b) $\beta \cos\theta - 4 \sin\theta$ plot based on the Williamson–Hall method with ε obtained from the slope of the linear fitting. Reproduced with permission from ref. 120. Copyright 2024, Wiley-VCH. (c) $\beta \cos\theta - 4 \sin\theta$ plot based on the Williamson–Hall method with ε as a percentage of strain. Reproduced with permission from ref. 121. Copyright 2024, Elsevier.

where the intercept is denoted by $K\lambda/D$ and the slope is denoted by ε. It is noted that ε values with positive and negative signs are reported for perovskite films, as shown in Fig. 9(b) and (c). The interpretation of the meaning of the sign is still controversial.[104,114,119] Some authors suggest the dependence of the sign on the strain type (tensile/compressive),[104,114] while others argue that a negative slope is physically meaningless.[119] In addition to the ambiguity in interpreting the sign of strain, the microstrain is incapable of providing depth-dependent strain information along the out-of-plane direction.

$$\beta_{(hkl)} = \frac{K\lambda}{D\cos\theta} + 4\varepsilon\tan\theta = \frac{K\lambda}{D\cos\theta} + 4\varepsilon\frac{\sin\theta}{\cos\theta}, \qquad (5)$$

$$\beta_{(hkl)}\cos\theta = \frac{K\lambda}{D} + 4\varepsilon\sin\theta. \qquad (6)$$

6.3. HR-TEM

In strain-related studies, TEM is frequently employed to directly verify d values in local spots.[122,123] Specifically, cross-sectional HR-TEM imaging, combined with microscopic diffraction pattern analysis, enables the direct investigation of structural variations at different depths within the film, facilitating strain analysis along the out-of-plane direction.[27,98,124] The acquisitions of d as a function of depth via cross-section HR-TEM analysis successfully complement the GIXRD analysis. Fig. 10(a) and (b) demonstrate the direct evidence of structural changes by calculating d values from TEM analysis. Fig. 10(a) illustrates three different spots across the perovskite bulk film, d values corresponding to (200) exhibit a gradual difference with $d = 3.07$ Å near the top surface

(spot II), $d = 3.11$ Å in the middle (spot V), and $d = 3.12$ Å near the bottom interface (spot VIII),[98] implying the strain inhomogeneity across the bulk film. However, Fig. 10(b) demonstrates consistent d values ($d = 3.19$ Å) for the (200) planes regardless of the depth, confirming a negligible strain variation.[98] The depth-dependent TEM results are consistent with the corresponding GIXRD data presented in Fig. 10(c) and (d). As depicted in Fig. 10(c), the decrease in the Bragg angle 2θ with increasing Ψ results from increasing d at high z (toward bottom interface), being in accordance with d from TEM results (Fig. 10(a)), while the invariant 2θ in Fig. 10(d) confirms the consistent d values from TEM analysis (Fig. 10(b)).[98] Cross-sectional TEM necessitates a sample preparation process using focused ion beam (FIB) milling, which typically utilizes high-energy ions (Ga^+ ions) to trim the perovskite bulk film into lamella, followed by a cleaning process with low beam power to minimize beam-induced damage.[125] It is revealed that conventional accelerating voltages (16–30 kV) and currents (>2.5 nA), which are commonly used for sampling metallic materials, can induce amorphization, chemical decomposition, and structural defects in organic samples.[126,127] Although some studies have reported that the structural damage to perovskite materials is inevitable during FIB milling process, other studies suggest that the damage by FIB milling can be sufficiently avoided by controlling the milling condition. A negligible difference was evidenced from a comparison of TEM analysis results between the perovskite sample directly deposited onto the TEM grid and the FIB-milled perovskite sample by 30 kV Ga^+ ion beam with a current of 28 nA to cut 0.5 μm-thick film from a bulk sample and 30 kV with 2.8 nA for further thinning the film.[125] Therefore, a careful modulation of the beam power for the FIB milling can

This journal is © The Royal Society of Chemistry 2025

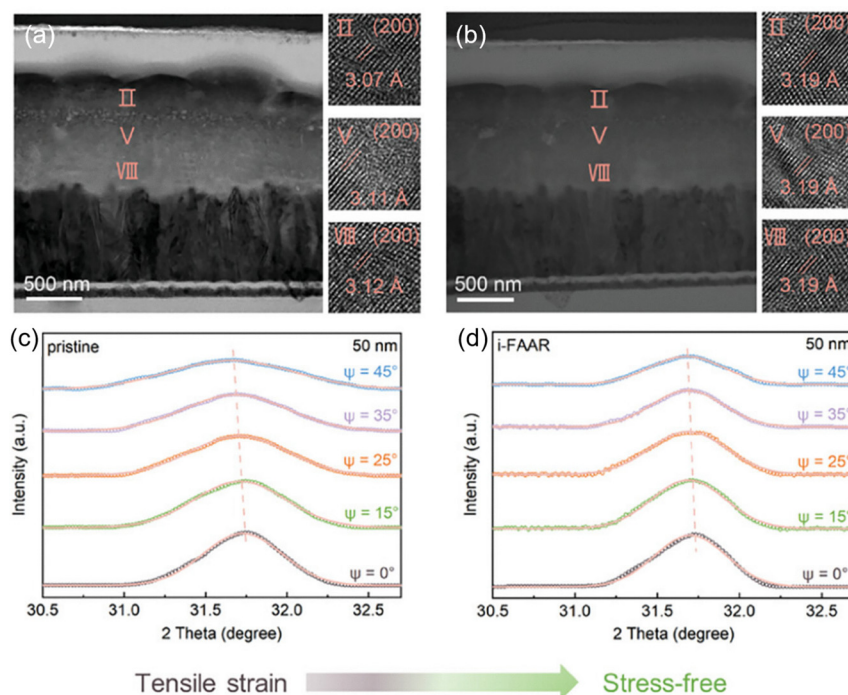Chem. Soc. Rev., 2025, 54, 7870–7912 | 7881

Fig. 10 Cross-sectional TEM images and HR-TEM analysis for obtaining the depth-dependent d of (a) pristine perovskite film and (b) target film with interface-formamidine active addition reaction (i-FAAR). GIXRD patterns of the (c) pristine and (d) i-FAAR-based perovskite films. GIXRD measurements are based on the side-inclination method with a probing depth of 50 nm determined by $\alpha_i = 0.3°-0.4°$. Reproduced with permission from ref. 98. Copyright 2024, Wiley-VCH.

induce negligible damage to perovskite, confirming the reliability of the TEM results for analyzing the residual strain in the perovskite film. Despite the strong merit of TEM analysis in terms of strain evaluation, which can directly monitor d, TEM is basically a spot-dependent analysis,[128] which demands statistical data analysis by measuring multiple spots to derive a reliable conclusion, particularly in halide perovskite film, as it is a polycrystalline material with a varied local structure. Furthermore, it is debatable that the validity of constant crystal structure (*e.g.*, cubic for FAPbI$_3$) despite the strain inhomogeneity along the out-of-plane direction because the residual in-plane tensile strain ideally induces the lattice contraction along the out-of-plane direction.[129] More systematic in-depth study of the lattice distortion on the atomic scale will be significantly helpful for understanding the multiscale strain impact and thus interpreting depth-dependent TEM results.

7. Experimental strategies to control out-of-plane strain inhomogeneity

7.1. Strain control by regulating crystallization

7.1.1. Additive strategy. Appreciable lattice strain with local structural inhomogeneity on sub- and super-grain levels is commonly and widely observed in halide perovskite films, which is apparently unfavorable for device applications in terms of both performance and reliability. It is regarded that less strain with less octahedral tilting increases the

contribution of covalency nature to Pb–I bonding in the inorganic core framework by intensifying the orbital overlapping,[37,56] which implies that the local strain with different degrees of octahedral tilting leads to different optoelectronic properties. The grain boundaries with a sudden lattice discontinuity are assumed to act similarly as boundaries for the electronic band structure.[62] Therefore, the local strain, originating from the local structural inhomogeneity, can afford to induce spatial inhomogeneity in the energy band structure, increasing the sensitivity of material properties.[27] Lattice matching between intra-grains as well as reducing the structural inhomogeneity on a sub-grain scale are highly important in terms of mitigating anisotropic behavior, including charge transport, recombination and stability. To this end, the formation of a uniform crystal orientation has been an experimental pursuit by lattice matching and strain engineering in the perovskite film. The additive strategy has been widely used to enhance the crystal orientation of the FAPbI$_3$ film by utilizing thiocyanate (SCN$^-$), formate (HCOO$^-$), or acetate (CH$_3$COO$^-$),[130–132] which is generally coupled with MACl or long alkyl chain-based chloride to form Cl/I hybrid octahedra,[54,133] unavoidably leaving a small amount of MA, which can occupy the FAPbI$_3$ lattice as a byproduct in the crystallized film,[133] and mostly repels large components, being incapable of filling the lattice point due to a significant difference in ionic radii, to the grain boundaries. The additives play a synergistic role in regulating crystal growth for tuning lattice strain and in passivating defects at the interface.[134,135] The additive engineering is also useful in resolving the inhomogeneous distribution of mixed cations along the

7882 | *Chem. Soc. Rev.*, 2025, **54**, 7870–7912

This journal is © The Royal Society of Chemistry 2025

out-of-plane composition, which otherwise induces detrimental effects by cation segregation.[136,137]

Small molecule-induced strain control. $FA_{1-x}Cs_xPbI_3$ films tend to induce vertical inhomogeneity in composition between FA and Cs, as illustrated in Fig. 5(b) and (c). An organic molecule with a sulfone group (O=S=O), such as 1-(phenyl-sulfonyl) pyrrole (PSP), is proposed to retard the segregation of cations in $FA_{1-x}Cs_xPbI_3$ films.[74] A preferential crystallization with Cs⁺, possibly due to its soft base property or different solubility,[138] can be kinetically hindered by accelerating crystallization rate with lowered energy barriers based on the devised interaction between the sulfone group of additive and Pb atoms in precursor solution (Fig. 11(a) and (b)). A negligible variation in interplanar distances along the out-of-plane direction ($d_{(002)} = 3.13$ Å at the bottom, bulk, and open top) is depicted in Fig. 11(c), indicating a homogeneous distribution between FA and Cs with different ionic radii. The variation in normalized intensity over 3 nm illustrated in Fig. 11(d) confirms a consistent interplanar distance without depth dependency.

Furthermore, the gradient strain along the out-of-plane direction can be effectively alleviated by formulating the local structures with different orientations. A strong chemical coordination effect of the additive, 1-(2-fluorobenzyl)-1H-pyrazolo-[3,4-b]pyridine-3-carboximidamide hydrochloride, to the inorganic framework results in a preferred interaction, particularly with the (111) facet and consequently lowers the surface energy of (111), which serves as a driving force for the (111)-oriented crystal growth on the surface.[108] Fig. 12(a)–(c) illustrates that

the gradient in-plane tensile strain of the control film is mostly released by facet complementarity between (100) and (111), as illustrated in Fig. 12(d). Notably, the local regions with distinct crystal orientation are intentionally adopted to suppress the out-of-plane strain inhomogeneity on a relatively macro scale (bulk film), even though the microstrain is rather pronounced by aggravating crystal orientational mismatch at grain boundaries.[108,139] When considering that the superior performance in both PCE and long-term stability is monitored from the target film with facet complementarity, the strategy for preferentially relieving the vertically gradient collective strain at the cost of bearing local strain at grain boundaries is effective. In other words, the collective strain inhomogeneity along the out-of-plane direction triggers a more detrimental impact than local structural mismatch mostly owing to its larger extent of effective strain range across the whole film, proposing that the depth-dependent biaxial in-plane strain, which is responsible for the out-of-plane strain inhomogeneity, should be resolved with a high priority in perovskite films.

Fig. 13(a) shows the chemical structure of N1,N4-bis(2,3,5,6-tetrafluoro-4-iodophenyl)terephthalamide (FIPh-A). The carbonyl (–C=O), amino (–NH), and iodotetrafluorophenyl (–C₆F₄I) groups of FIPh-A facilitate the crystallization of perovskite and relieve strain as well.[140] Notably, the crystallization of the $FAPbI_3$ perovskite lattice in the presence of FIPh-A effectively increases the formation energy of I⁻ vacancies from 4.86 eV to 5.19 eV (Fig. 13(b)),[140] enhancing the stability of the inorganic framework. FIPh-A, as a multifunctional additive, is highly favorable for strongly interacting with various sites of the
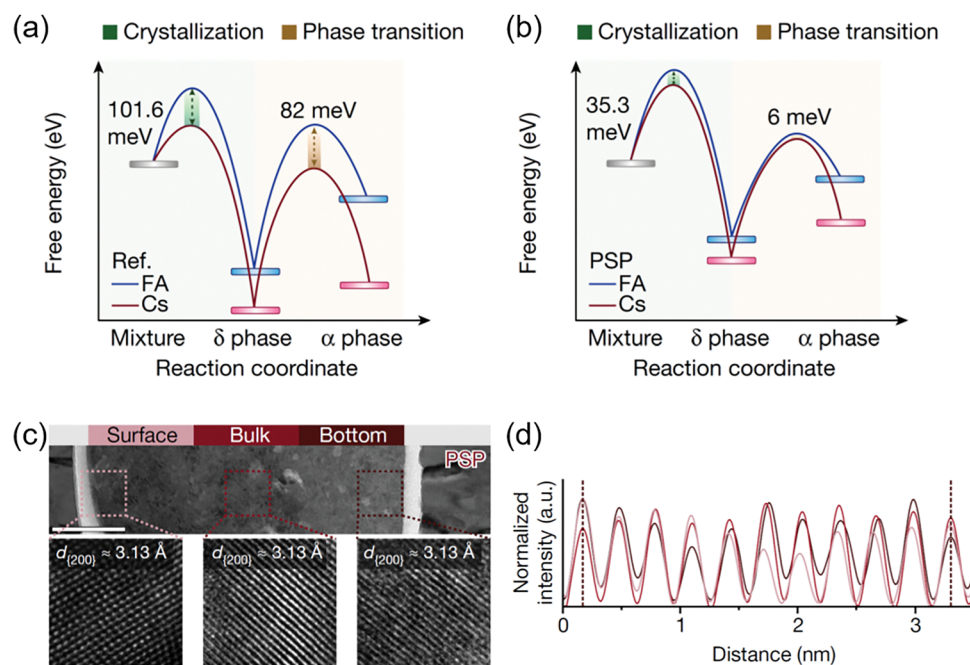

Fig. 11 Schematics of computational results of free energy as a function of the reaction coordinate for (a) control and (b) target conditions with PSP. (c) Cross-sectional high-angle annular dark-field TEM images (200 nm for the scale bar) and depth-dependent HR TEM images (7.3 × 7.3 nm) of the crystal orientation-regulated $FA_{1-x}Cs_xPbI_3$ film. (d) Calculated intensity over 3 nm of the crystal orientation-regulated $FA_{1-x}Cs_xPbI_3$ film depending on the depth. Color code corresponds to surface, bulk, and bottom indicated in (c). Reproduced with permission from ref. 74. Copyright 2023, Springer Nature.
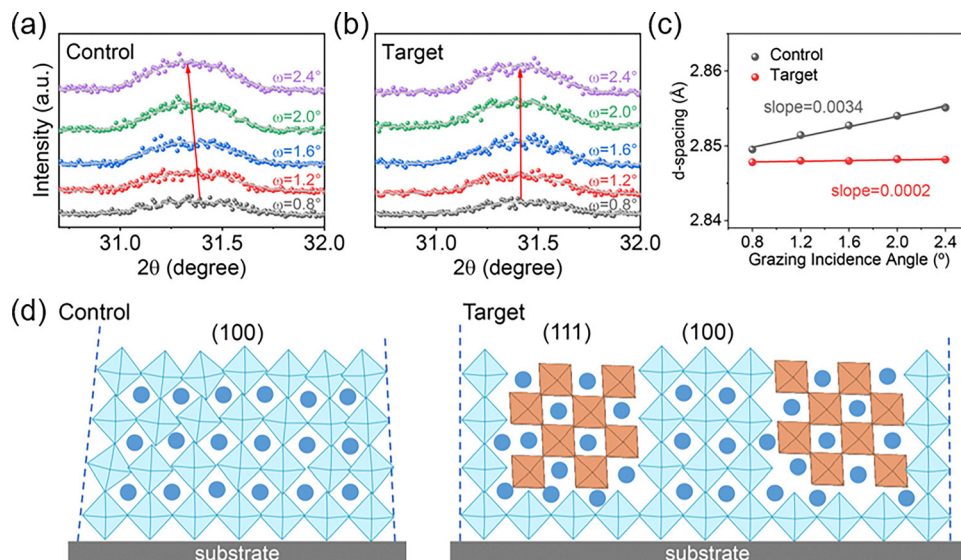
This journal is © The Royal Society of Chemistry 2025

Chem. Soc. Rev., 2025, **54**, 7870–7912 | **7883**

Fig. 12 Depth-dependent GIXRD patterns with varying ω of (a) control and (b) target perovskite films. (c) $d_{(211)}-\omega$ plots converted from the GIXRD patterns. (d) Schematic of lattice orientation in the control (left) and target (right) films. Reproduced with permission from ref. 108. Copyright 2025, American Chemical Society.
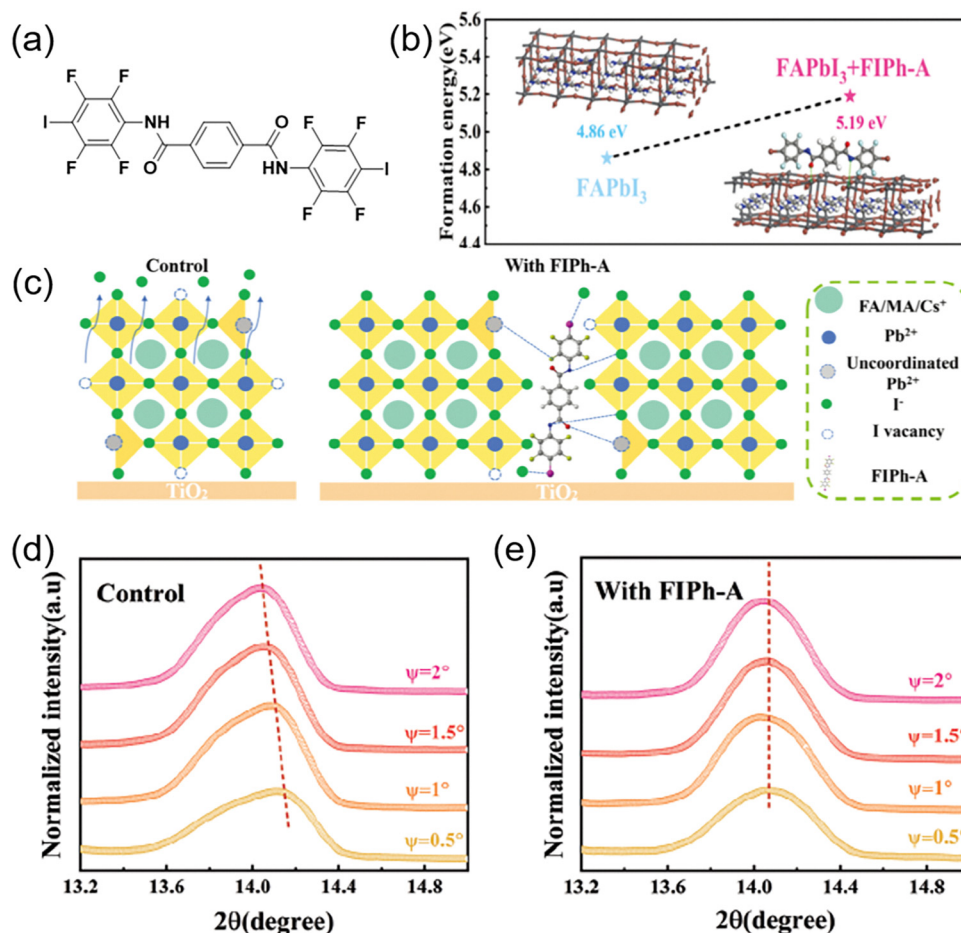

Fig. 13 (a) Molecular structure of FIPh-A. (b) Formation energy of an I^- vacancy calculated using density functional theory (DFT). (c) Illustration of the interaction mechanism between FIPh-A and the perovskite lattice at the grain boundary compared to the control perovskite film. GIXRD spectra of the (d) control film and (e) FIPh-A-employed film. ψ in (d) and (e) indicates ω in the iso-inclination method. Reproduced with permission from ref. 140. Copyright 2024, Wiley-VCH.

7884 | *Chem. Soc. Rev.*, 2025, **54**, 7870–7912

This journal is © The Royal Society of Chemistry 2025

perovskite lattice (*e.g.*, uncoordinated Pb^{2+} and I^-), as illustrated in Fig. 13(c), which contributes to the stabilization of the octahedra inorganic framework in the perovskite lattice. The GIXRD results shown in Fig. 13(d) and (e) confirm that tensile strain is reduced upon the addition of FIPh-A.[140] The synergistic effect of C=O and –NH on stabilizing the inorganic framework while regulating lattice crystallization is also responsible for the residual strain alleviation in the lattice. As shown in Fig. 13(d), the control film suffers from intensive tensile strain by showing a gradual 2θ peak shift toward a lower angle as ω increases in the iso-inclination method of GIXRD. The use of FIPh-A encourages lattice crystallization bearing negligible depth-dependent strain difference, as confirmed by the little 2θ peak shift as ω varies in Fig. 13(e). The relieved tensile strain seems to be closely related to the increased crystalline quality with a preferred orientation.[141]

Crosslinking-induced strain control. Crosslinking-induced strain-regulation crystallization (CSRC) is one of the effective strategies for inducing in-plane compressive strain in the perovskite film.[142] Fig. 14(a) illustrates CSRC treatment with trimethylolpropane triacrylate (TMTA), where TMTA is dissolved in chlorobenzene, acting as an antisolvent. TMTA, consisting of multiple functional groups (–OH and C=O), undergoes crosslinking and turns into poly TMTA (PTMTA) during the annealing process at 150 °C.[143,144] Before annealing for crystallization of the perovskite film, the intermediate phase morphology highly depends on the additives in the antisolvent. When no additives (control) or PTMTA (already crosslinked TMTA) are added in the antisolvent, the coverage of the intermediate phase is poor, while TMTA in the antisolvent results in the film with improved coverage and homogeneity (Fig. 14(b)–(d)). Therefore, the TMTA is assumed to contribute to uniformly
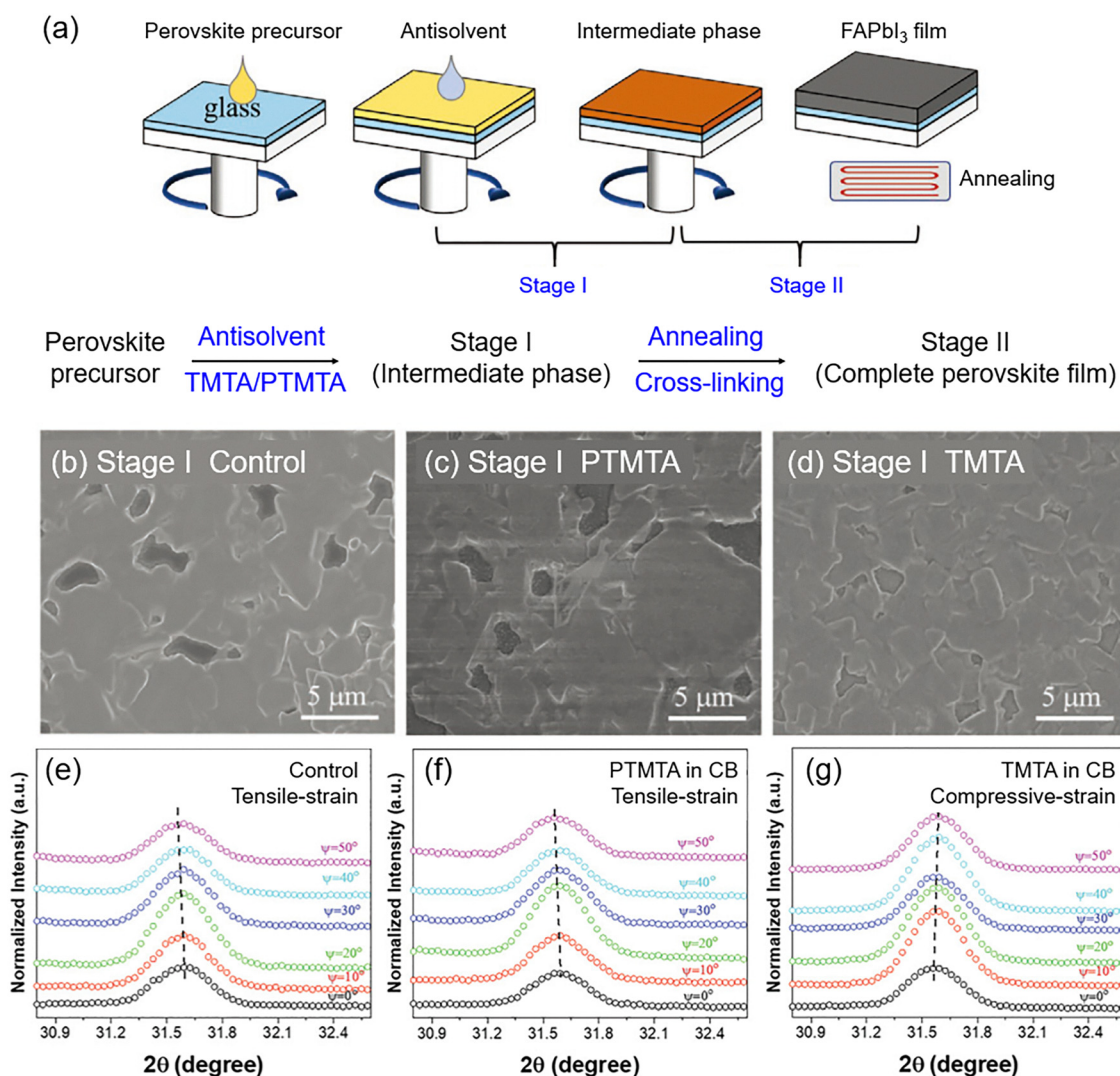

Fig. 14 (a) Schematic of TMTA-CSRC treatment based on two stages (stages I and II) of perovskite formation. SEM images of (b) the control, (c) PTMTA-, and (d) TMTA-treated perovskite films at stage I. GIXRD spectra of (e) the control, (f) PTMTA-, and (g) TMTA (for SCRC)-treated perovskite films. Reproduced with permission from ref. 142. Copyright 2021, Wiley-VCH.

This journal is © The Royal Society of Chemistry 2025

Chem. Soc. Rev., 2025, **54**, 7870–7912 | **7885**

distributed heterogeneous nucleation over the perovskite precursor film (stage I) and enhance the grain size by applying *in situ* crosslinking (stage II).[142] The residual lattice strain of the resultant perovskite film is analyzed by measuring GIXRD using the side-inclination method. Although the control film and the PTMTA-induced film exhibit a slight 2θ shift toward a lower angle as Ψ increases (Fig. 14(e) and (f)), indicating a pronounced in-plane tensile strain at the bottom, the CSRC-treated film with TMTA bears in-plane compressive strain (the opposite 2θ peak shift direction) with smaller d increasing the depth from the top to the bottom (Fig. 14(g)). The residual in-plane compressive strain is ascribed to the compression confinement of the perovskite lattice during the crosslinking of TMTA molecules coordinated with Pb in perovskite nuclei because the perovskite growth and TMTA crosslinking occur simultaneously during the annealing process.[142] The resultant compression confinement seems to offset the processing-induced in-plane tensile strain, including the effect of thermal contraction with different degrees.

Similarly, acrylamide (Am) is introduced as a monomer that undergoes light-triggered polymerization and turns into poly-acrylamide (PAm).[145] When AM is coated after finishing the crystallization of the perovskite film (AAC treatment in Fig. 15(a)), Am is ruled out of the crystallization of perovskite

and merely leads to a surface passivation effect. However, AM is treated on wet film with perovskite precursors before crystallization in the ABC treatment (Fig. 15(b)), which allows AM to participate in the nucleation and the growth of perovskite crystals and results in large and isolated grains, leaving PAm at grain boundaries and the top surface in the amorphous phase. It is worth noting that the liquidity of AM suppresses lattice distortion during crystal growth, thereby reducing lattice strain during the crystallization of the perovskite film, which balances the chronic in-plane tensile strain induced by different degrees of lattice thermal expansion/contraction with the underlying substrate. The GIXRD patterns of the (022) plane of the AAC-treated perovskite film exhibit the same tendency as the control film without AM inclusion, where the gradual 2θ peak shift toward a lower angle as Ψ increases in the side-inclination method indicates the residual tensile strain (Fig. 15(c) and (d)). Meanwhile, almost full release of the tensile strain is observed when the ABC strategy is applied, demonstrating a negligible peak shift regardless of varying Ψ (Fig. 15(e)).[145] Similarly, the residual lattice strain can be effectively regulated by incorporating self-polymerizable additives into the perovskite wet film prior to crystallization.[146–148] Self-polymerizing materials are prone to restrict the thermal expansion of the perovskite during the crystallization process at high temperatures, effectively
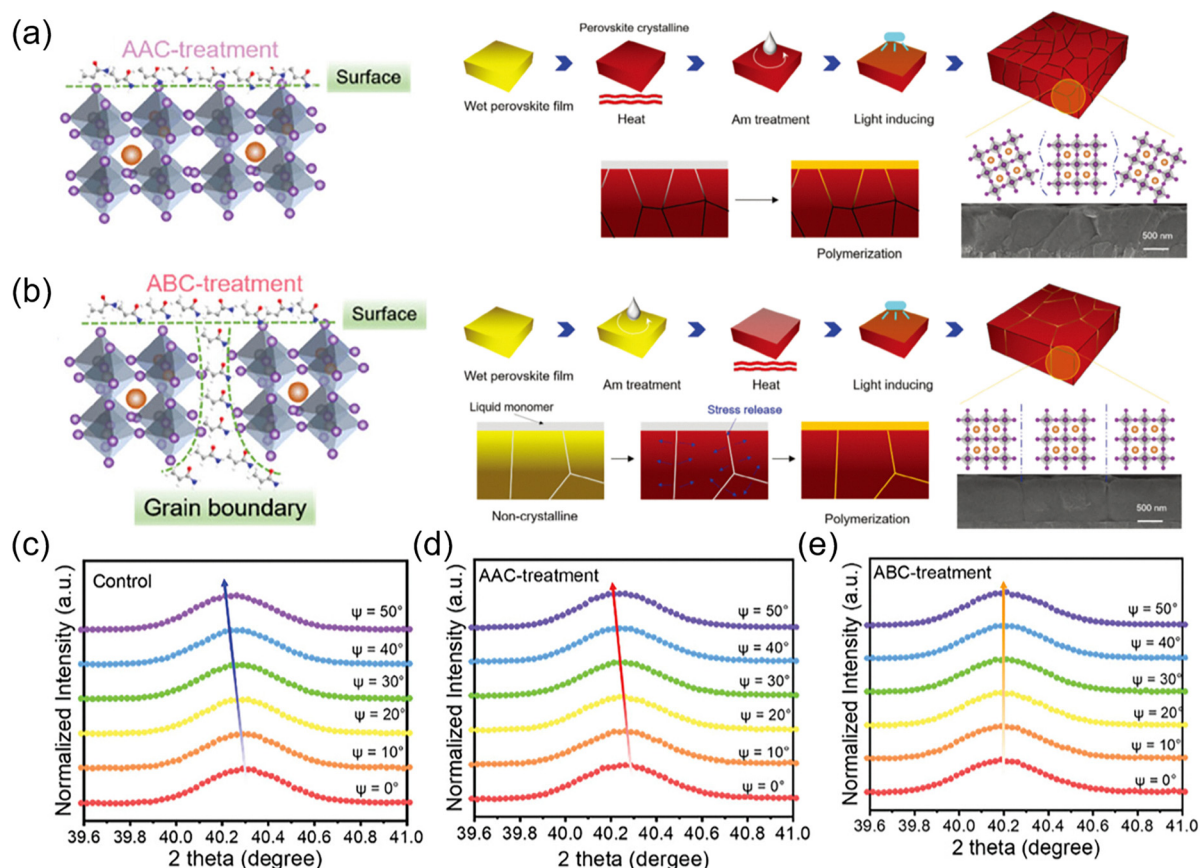

Fig. 15 Illustration of the perovskite lattice and schematic of perovskite crystallization using (a) AAC and (b) ABC treatments with corresponding grains and grain boundaries. GIXRD patterns for the (022) planes of (c) control, (d) AAC-treated, and (e) ABC-treated perovskite films. Reproduced with permission from ref. 145. Copyright 2024, Wiley-VCH.

7886 | *Chem. Soc. Rev.*, 2025, **54**, 7870–7912

This journal is © The Royal Society of Chemistry 2025

mitigating the tensile strain in the perovskite film.[146–148] Self-polymerizing *n*-methacrylamide (NMA) monomers interact with perovskite nuclei and constrain the perovskite lattice from thermally expanding during the annealing process, which reduces the residual tensile strain by approximately 34%.[146] Furthermore, the inclusion of octafluoro-1,6-hexanediol diacrylate (OF-HDDA) induces coordination between the –C=O of OF-HDDA and Pb^{2+} of perovskite during the annealing process and thus regulates crystallization. Consequently, the combined polymerization of OF-HDDA occurs with perovskite crystallization, effectively alleviating the residual tensile strain.[147]

7.1.2. Epitaxial growth strategy. Epitaxial growth of three-dimensional (3D) perovskite film by utilizing two-dimensional (2D) perovskite as a substrate is also regarded as one of the effective ways to control the lattice strain by regulating crystallization. 2D perovskite $(NAM)_2PbI_4$ (NAM = nicotinamide) is devised to provide a highly matched heterointerface with $FAPbI_3$. $(NAM)_2PbI_4$ has a weak hydrogen bonding between the organic molecule of NAM^+ and the inorganic PbI_6^{4-} framework, which loosens the octahedra tilting and allows for a large Pb–I–Pb angle (167.18°).[122] The Pb–I–Pb angle of 2D perovskite is well matched with that of 3D $FAPbI_3$ (176.85°), proposing the favorable heterointerface alignment between the (002) plane of

$(NAM)_2PbI_4$ and the (100) plane of $FAPbI_3$, as illustrated in Fig. 16(a). Although the 2D perovskite layer can be partially dissolved during the spin-coating of the 3D perovskite precursor solution, a portion remains at the bottom and serves as a substrate with a matched lattice for the heteroepitaxial growth of $FAPbI_3$, while the dissolved part of 2D recrystallizes at the grain boundaries of $FAPbI_3$, as shown in Fig. 16(b).[122] As indicated by the 2θ shift toward lower angle with increasing Ψ, as depicted in Fig. 16(c), the in-plane tensile strain is inherent in the control perovskite film, while the heteroepitaxial growth by utilizing the lattice matching with underlying 2D perovskite enables the upper 3D perovskite to involve in-plane compressive strain near the bottom interface, showing 2θ shift toward higher angle (decreased d) with increasing Ψ (increased beam penetration from the surface) in Fig. 16(d). Therefore, in the 2θ–$\sin^2\Psi$ plot (Fig. 16(e)), the negative slope for the control film is converted to the positive slope for the target film with $(NAM)_2PbI_4$.

Moreover, 2D nanoflakes play a similar role in regulating lattice strain by providing a well-matched crystal lattice structure with the perovskite layer for heteroepitaxial growth.[123,149,150] Fig. 17(a)–(c) shows the HR-TEM images of WS_2 nanoflakes. The 2.79 Å of d along the (100) plane in WS_2 nanoflakes is twice
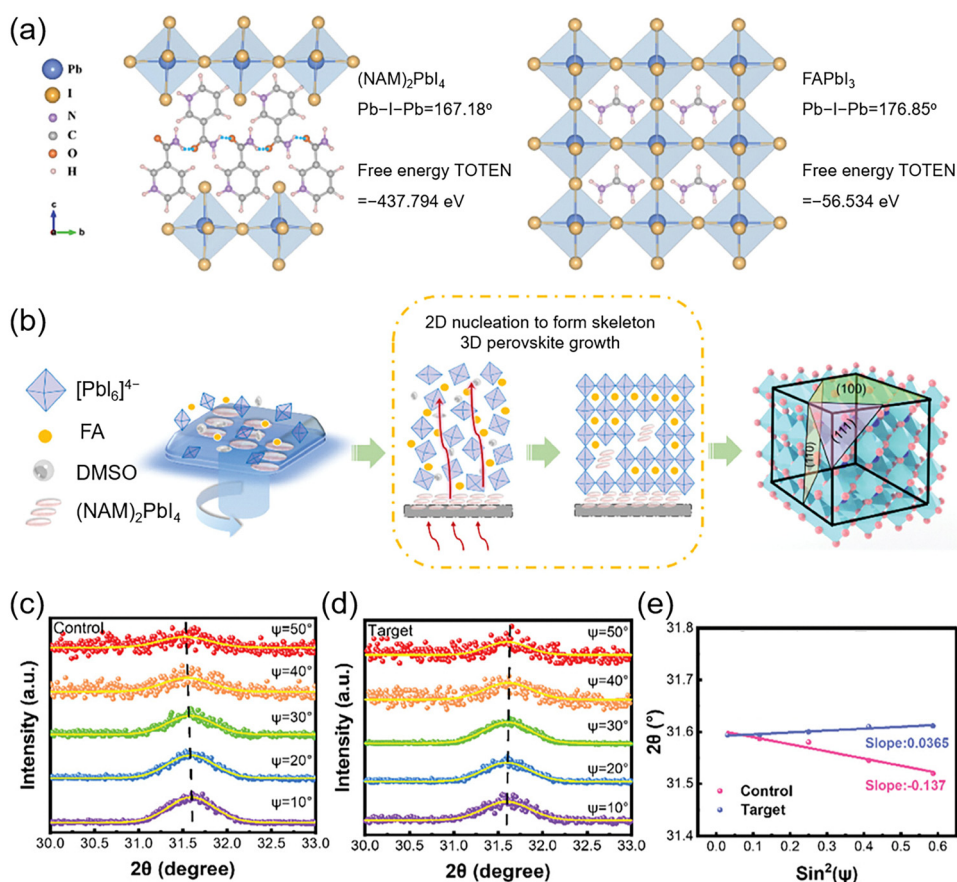

Fig. 16 (a) Illustration and Pb–I–Pb angles of $(NAM)_2PbI_4$ and $FAPbI_3$. Free energy TOTEN refers to the total free energy calculated based on DFT. (b) Schematic mechanism for the crystallization of the perovskite film using $(NAM)_2PbI_4$. GIXRD patterns of (c) the control and (d) $(NAM)_2PbI_4$-assisted target films. (e) 2θ–$\sin^2\Psi$ plots with linear fitting. Reproduced with permission from ref. 122. Copyright 2023, Wiley-VCH.

This journal is © The Royal Society of Chemistry 2025

Chem. Soc. Rev., 2025, **54**, 7870–7912 | **7887**

that of the (100) plane in CsPbBr$_3$, leading to favorable epitaxial growth of the CsPbBr$_3$ layer on top of WS$_2$ nanoflakes with lattice matching, as shown in Fig. 17(d) and (e). The van der Waals interactions between CsPbBr$_3$ and WS$_2$, along with the dangling bond-free surface of the WS$_2$ (100) plane, facilitate the crystal growth of CsPbBr$_3$ highly oriented along the out-of-plane direction layer with large grains and a low defect density.[123] Furthermore, the weak interaction between 2D nanoflake WS$_2$ and perovskite can act as a lubricant for lattice movements at the perovskite bottom interface during annealing and cooling (temperature changing) processes, which is beneficial in terms of residual strain.[123] GIXRD analysis with iso-inclination method is carried out to define the residual strain, as depicted in Fig. 17(g)–(i). In the absence of WS$_2$, no crystal growth regulation along the out-of-plane direction, 2θ peaks exhibit a noticeable shift toward lower angles as ω increases (Fig. 17(g)), while the introduction of WS$_2$ at the bottom interface significantly reduces the diffraction peak shift, as shown in Fig. 17(h). Fig. 17(i) illustrates that the in-plane tensile strain at the bottom lattice, reflected in a steep slope, in the control film is mitigated by regulating crystallization by WS$_2$, as noticed by a decreased slope of the d–ω plot.

7.1.3. Solid conversion strategy. More recently, noticeably oriented FAPbI$_3$ was reported by solid-based conversion from two-dimensional (2D) to three-dimensional (3D) crystals. Although rapid nucleation by evaporating solvents in traditional methodologies (*e.g.*, antisolvent) makes the control of crystal growth challenging,[151] the solid-based conversion from 2D FAMAPbI$_4$ perovskite (*Imma* space group) to 3D FAPbI$_3$ lattice by the sublimation of MAI is found to be highly beneficial for regulating the crystal orientation, as illustrated in Fig. 18(a).[61] The small ionic radius of MA$^+$ facilitates the lower vaporization temperature, unlike longer alkyl chain-based ones, while the consistency in halide composition with I$^-$ helps reduce compositional entropy and align crystal orientation during the lattice reordering.[61] Consequently, neighboring local spots in Fig. 18(b) demonstrate notably consistent structural ordering with analogous patterns and almost identical interplanar distance along (001), as confirmed in the high-magnification HR-TEM images (Fig. 18(c)). It is indeed worth noting that the lattice orientation in the single grain and the lattice matching between intra grains are obtained by the solid conversion (Fig. 18(d)), which is confirmed by the comparison of GIXRD patterns depicted in Fig. 18(e)–(g). The FAPbI$_3$ film prepared by applying the control method exhibits a significant peak 2θ shift by varying the incidence angle of ω (Fig. 18(e)), implying the prominent in-plane tensile strain at the bottom, while the solid conversion methodology enables FAPbI$_3$ film to
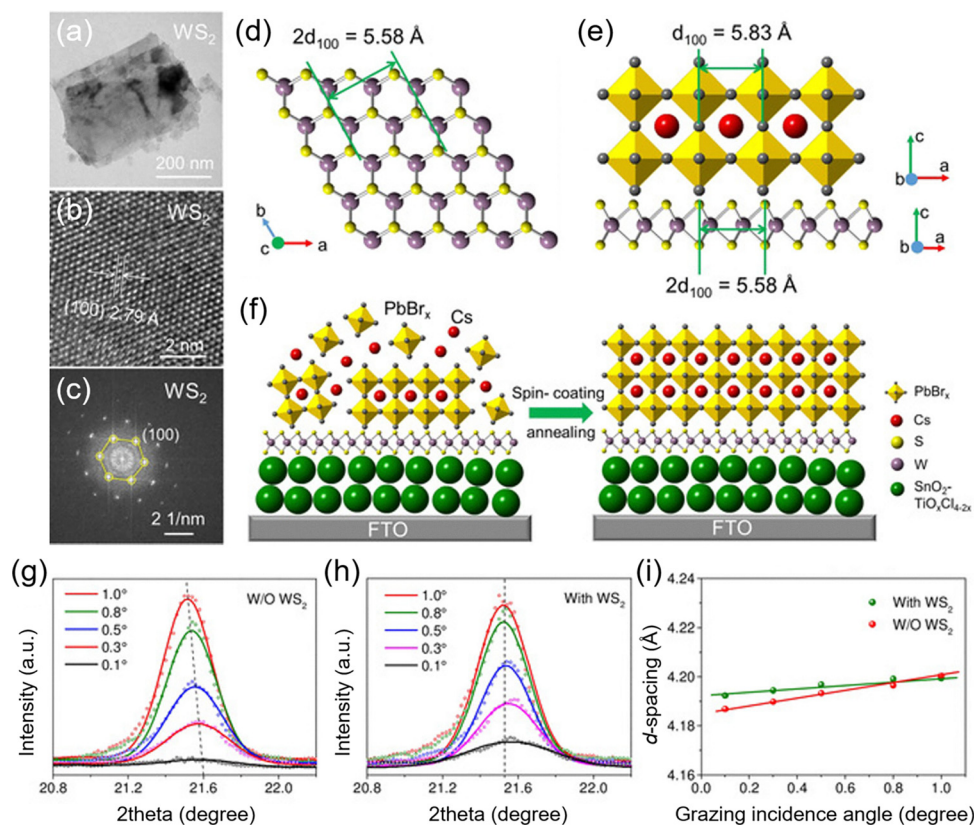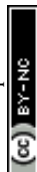

Fig. 17 (a) TEM, (b) HR-TEM, and (c) FFT images of WS$_2$ nanoflakes. (d) Atomic arrangement of the WS$_2$ (100) plane. (e) Cross-sectional atomic structure of the CsPbBr$_3$/WS$_2$ heterojunction. (f) Illustration of the van der Waals epitaxial growth of the CsPbBr$_3$ film on the WS$_2$-coated electron transport layer. Depth-dependent GIXRD patterns of the CSPbBr$_3$ film (g) without and (h) with WS$_2$ layer. (i) $d_{(110)}$–ω plots depending on WS$_2$ layer. Reproduced with permission from ref. 123. Copyright 2020, Wiley-VCH.

7888 | *Chem. Soc. Rev.*, 2025, **54**, 7870–7912

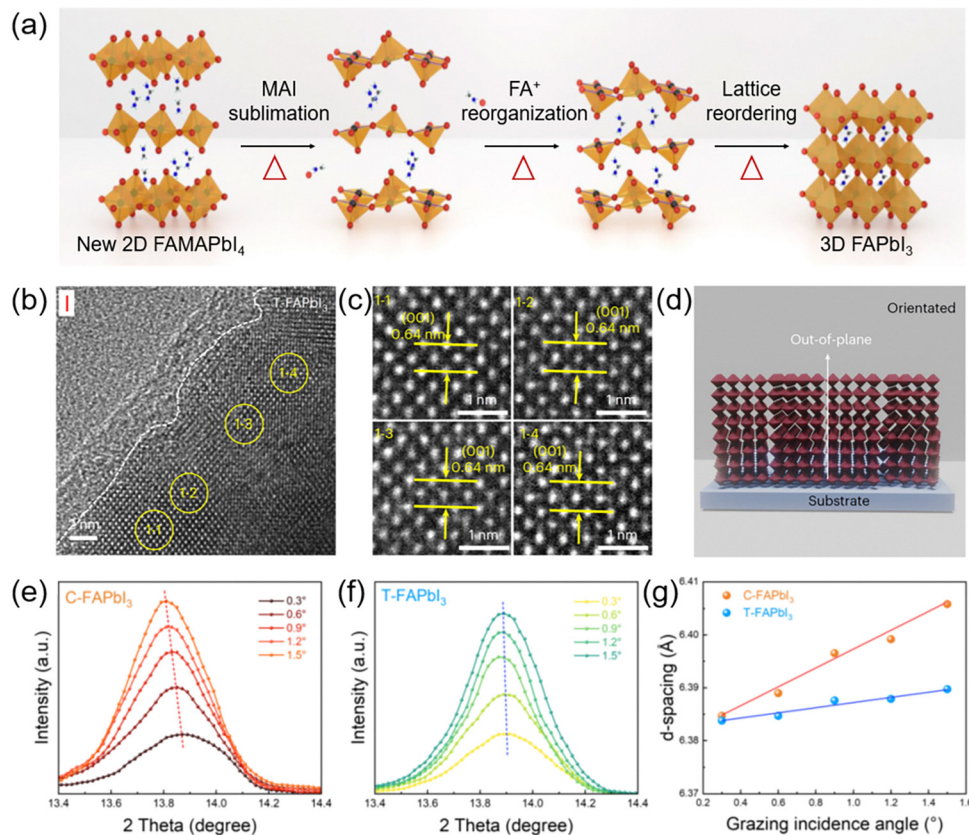This journal is © The Royal Society of Chemistry 2025

Fig. 18 (a) Schematic of the phase transformation *via* solid conversion from FAMAPbI$_4$ to FAPbI$_3$. (b) HR-TEM image and (c) high-magnification HR-TEM images of different spots (1-1 to 1-4 as indicated in (b)) of the crystal orientation-regulated FAPbI$_3$ film. (d) Schematic of the crystalline film of the crystal orientation-regulated FAPbI$_3$ film. Depth-dependent GIXRD plots for the (100) plane of the (e) control and (f) target films based on the solid conversion. (g) Interplanar spacing values as a function of incidence angle. Reproduced with permission from ref. 61. Copyright 2025, Springer Nature.

bear insignificant in-plane tensile strain, namely negligible strain inhomogeneity along the out-of-plane direction by presenting a significantly lowered slope in the d–ω plot (Fig. 18(g)).

The chemicals used for regulating the crystallization of the perovskite film in Section 7.1 are summarized in Table 1, involving related information on perovskite, strain and photovoltaic performance with long-term stability.

7.2. Strain control at the bottom interface

7.2.1. Small molecules as in-plane strain relievers

Small molecules on the metal oxide selective contact. As previously discussed, the solution-processed polycrystalline perovskite film generally exhibits residual in-plane tensile strain, which is the upmost pronounced at the bottom interface mainly owing to the low thermal coefficient of the rigid underlying substrate and gradually released across the film toward the top surface. The resultant strain inhomogeneity along the out-of-plane direction, which is attributed to the in-plane tensile strain with different degrees as a function of depth, is relieved by employing small molecules between the rigid substrate and the soft perovskite, as illustrated in Fig. 19(a). The control structure of the perovskite film, grown on SnO$_2$, demonstrates a prominent in-plane tensile strain by shifting the 2θ toward a lower angle, indicating an increase in d, with

increasing χ for deep penetration shown in Fig. 19(b).[102] However, the depth-dependent strain inhomogeneity is greatly relieved by employing phosphorylethanolamine (PEA) as an interlayer to restrain the perovskite film from being directly anchored to rigid SnO$_2$, which is evidenced by the negligible dependence of 2θ on χ, as illustrated in Fig. 19(c). The strain is quantified by converting the GIXRD results into the 2θ–$\sin^2\psi$ plot, which reveals that a steep slope of -0.043 ± 0.007 from the control film is reduced to 0.009 ± 0.009 by employing PEA, suggesting the successful elimination of the in-plane tensile strain. PEA consists of phosphate (–OPO(OH)$_2$) and amine groups (–NH$_2$), which are linked by an alkyl chain, where the alkyl chain serves a pivotal role in relieving the in-plane strain of the perovskite film by rotating along the C–C bond,[152] while the phosphate contributes to the passivation of oxygen vacancies of SnO$_2$ by forming a strong interaction as Lewis base.[153] Thus, –P=O of the phosphate can form a strong coordinated bond with both uncoordinated Pb^{2+} of the perovskite film and Sn^{4+} of the SnO$_2$ layer, while NH$_2$ forms a hydrogen bond with I$^-$ of the perovskite framework.[154,155] Therefore, various small molecules with the same functional groups of phosphate and amine have been widely utilized as an interlayer between the metal oxide substrate and the perovskite film.[154–157] Methylphosphonic acid (MPA) with a phosphate group releases the

This journal is © The Royal Society of Chemistry 2025

Chem. Soc. Rev., 2025, **54**, 7870–7912 | **7889**

Table 1 Chemicals employed for regulating the crystallization of perovskite film to relieve the out-of-plane strain inhomogeneity

Chemical type	Chemical equation	Chemical structure	Interaction type	Perovskite	Other additives or passivation materials	Characterization	Strain type (control)	Strain type (target)	PCE (%)	Long-term stability	Long-term stress condition	Ref.
Small molecule	Methylammonium iodide (MAI)			$FAPbI_3$		GIXRD	Tensile	Released tensile	25.01	$T_{90.8} = 150$ h	mpp, one sun, ambient air, 30% RH	61
Small molecule	1-(Phenylsulfonyl)-pyrrole (PSP)		Coordinated bond	$FA_{1-x}Cs_xPbI_3$	$MAPbBr_3$, PbI_2, MACl	TEM			26.09	$T_{92} = 2500$ h	mpp, N_2, RT, one sun	74
Small molecule	1-(2-Fluorobenzyl)-$1H$-pyrazolo[3,4-b]pyridine-3-carboximidamide hydrochloride (FPPC)		Coordinated bond/hydrogen bond	$FAPbI_3$	MACl	GIXRD	Tensile strain 0.0034^b	Released tensile 0.0002^b	25.63	$T_{90} = 500$ h	mpp, N_2, one sun, 35 °C	108
2D perovskites	$(NAM)_2PbI_4$			$FAPbI_3$	MACl	GIXRD	Tensile 61 Mpa^c	Compressive 16 Mpa^c	25.2	$T_{91} = 300$ h	mpp, one sun, N_2	122
2D nanoflake	WS_2			$CsPbBr_3$		GIXRD TEM	Tensile	Released tensile	10.65	$T_{80} = 120$ h	Encapsulation, 80% RH	123
Small molecule	$N1,N4$-Bis(2,3,5,6-tetrafluoro-4-iodophenyl)-terephthalamide, FIPh-A		Coordinated bond/hydrogen bond	$FA_{0.60}MA_{0.36}Cs_{0.04}Pb(I_{0.97}Br_{0.02}Cl_{0.01})_3$		GIXRD	Tensile	Released tensile	24.6	$T_{92} = 500$ h	One sun, aging track	140
Small molecule	Trimethylolpropane triacrylate (TMTA)		Coordinated bond	$(FAPbI_3)_{0.95}(MAPbBr_3)_{0.05}$		GIXRD	Tensile	Compressive	22.39	$T_{95} = 4000$ h	Stored in a dark, dry box, RT	142
Small molecule	Acrylamide (Am)		Coordinated bond/hydrogen bond	$(FAPbI_3)_{0.95}(MAPbBr_3)_{0.05}$		GIXRD	Tensile 36.5 MPa^c	Released tensile 7.44 MPa^c	24.45	$T_{80} = 1008$ h	One sun, 10% RH	145
Small molecule	n-Methacrylamide (NMA)		Coordinated bond/hydrogen bond	$FA_xMA_{1-x}PbCl_xI_{3-x}$		GIXRD	Tensile 85.0 ± 5.6 Mpa^c	Released tensile 55.9 ± 5.2 Mpa^c	22.0	$T_{91} = 1500$ h	Aging track, ambient air (25 °C ± 5 °C, 30 ± 5% RH), dark	146
Small molecule	Octafluoro-1,6-hexanediol diacrylate (OF-HDDA)		Coordinated bond/hydrogen bond	$Cs_{0.03}FA_{0.95}MA_{0.02}Pb(I_{0.975}Br_{0.025})_3$		GIXRD	Tensile 0.613^a	Released tensile 0.117^a	24.76	$T_{92} = 1000$ h	N_2, mpp, one sun, 35 °C	147
Small molecule	N-Carbamoyl-2-propan-2-ylpent-4-enamide (apronal)		Coordinated bond/hydrogen bond	$Cs_{0.05}(FA_{0.85}MA_{0.15})_{0.95}Pb(I_{0.75}Br_{0.25})_3$		GIXRD	Tensile	Compressive	25.09	$T_{90.3} = 1404$ h	N_2, mpp, encapsulation, one sun, 35 °C	148

^{a} Value obtained from the 2θ–$\sin^2\Psi$ plot (side-inclination method). ^{b} Value obtained from the d–ω plot (iso-inclination method). ^{c} Value obtained from the 2θ–$\sin^2\Psi$ plot according to eqn (4) (side-inclination method).mpp: maximum power point tracking; +RH: relative humidity.

7890 | *Chem. Soc. Rev.*, 2025, **54**, 7870–7912

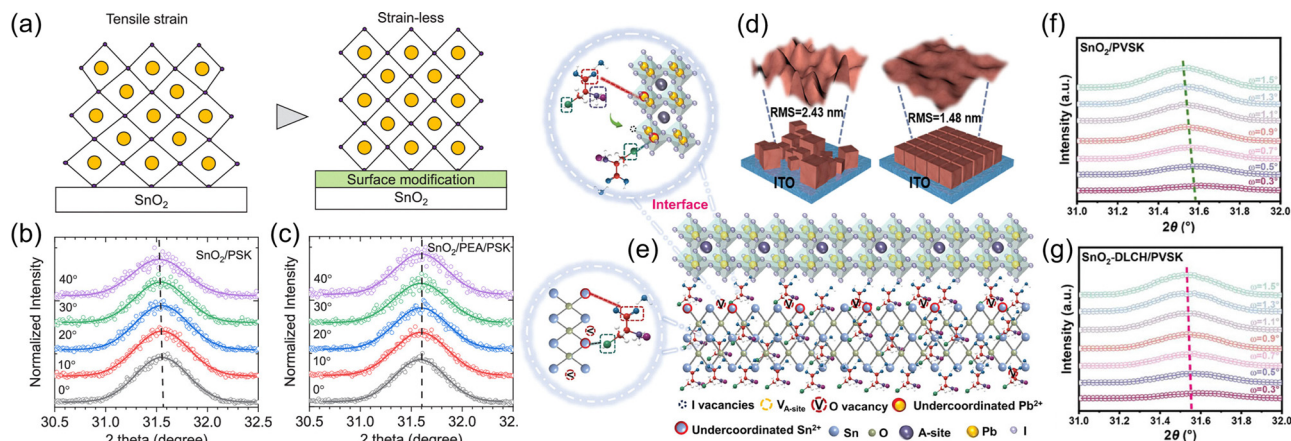This journal is © The Royal Society of Chemistry 2025

Fig. 19 (a) Schematic of the regulation of in-plane tensile strain by surface modification of SnO₂. GIXRD spectra of perovskite films on (b) bare SnO₂ and (c) PEA-modified SnO₂. Reproduced with permission from ref. 102. Copyright 2024, American Chemical Society. (d) Reduction in root-mean-square surface roughness after the incorporation of DLCH. (e) Schematic of bottom-up multilayer control by DLCH. GIXRD spectra of perovskite films deposited on (f) SnO₂ and (g) DLCH-modified SnO₂. Reproduced with permission from ref. 156. Copyright 2024, Wiley-VCH.

residual in-plane tensile strain of the perovskite film, leading to the slope reduction in the $2\theta-\sin^2\Psi$ plot from -0.043 ± 0.007 to -0.043 ± 0.007. The relatively weak effect of strain alleviation by MPA, compared to the slope of 0.009 ± 0.009 by PEA, could be attributed to the length of the alkyl chain. Longer alkyl chain linker connecting the bifunctional groups has a flexible molecular geometry and can accommodate the strain.[102] Apart from phosphate, small molecules with other electronegative functional groups, such as $-C=O$, $-S-H$, and pyridine, have been also utilized as an interlayer to release the residual strain by forming coordinated bonds with Pb²⁺ of upper perovskite film and Sn⁴⁺ of SnO₂.[120,154–159] DL-Cysteine hydrochloride monohydrate (DLCH) is pre-employed in the SnO₂ colloidal solution to suppress the spontaneous agglomeration of SnO₂ nanoparticles using the coordinated bond between DLCH and Sn⁴⁺,[156] which accordingly leads to smooth surface of SnO₂ layer as surface roughness decreases from 2.43 nm to 1.48 nm (Fig. 19(d)). DLCH also comprises multi-functional groups of $-COOH$ and $-SH$, serving as Lewis bases to passivate uncoordinated Pb²⁺ and Sn⁴⁺ defects,[157,160–163] and $-NH_3^+$, forming a hydrogen bond with I⁻.[156] Therefore, the formation of multiple bonding modes allows DLCH to perform bottom-up multifunctional modification, as illustrated in Fig. 19(e).[164] In addition to the role of DLCH molecule in mitigating the in-plane tensile strain at the interface, the smoother surface of SnO₂–DLCH is indicated as a parameter to reduce the strain by improving the bottom interface contact.[165] Consequently, the in-plane tensile strain of the control film, with a prominent shift of 2θ toward lower angle with increasing ω (Fig. 19(f)), is effectively relieved by employing DLCH at the interface, showing a marginal shift in Fig. 19(g).

Small molecules on the polymer selective contact. Small molecules with an alkyl chain (or flexible moiety) and functional groups are similarly utilized to release residual tensile strain of the perovskite deposited on the polymer.[166,167] Most of the

polymers, which can serve as a selective contact with superior hole transport, have a lower thermal expansion coefficient compared to that of halide perovskite,[25,168] causing the same issue of the residual in-plane tensile strain, to a lesser extent than metal oxide, at the bottom interface. Fig. 20(a) illustrates the volume contraction of the ideal case (I) and real case (II), where the latter is dominantly governed by thermal contraction with different degrees between perovskite and poly(triaryl amine) (PTAA) substrate.[160,167,169] It is noteworthy that the real state with residual strain (II) is depicted in bi-axial in-plane tensile strain accompanied by out-of-plane compressive strain although specific experimental evidence is not shown. Amphiphilic soft molecules (ASMs) containing long alkyl chains and Lewis base groups are introduced at the interface between perovskite and PTAA, aiming to release the residual strain. Dodecyltrimethylammonium chloride (DTAC) is employed as an ASM and helps the contraction mismatch between two adjacent layers by enabling dynamic modulation of DTAC based on its soft self-adaptive long chain (III in Fig. 20(a)).[170] In addition, the interaction between the hydrophilic Lewis base group and the uncoordinated Pb²⁺ of the perovskite can cope with defects (IV in Fig. 20(a)). The residual strain of the control and target films is analyzed by the Williamson–Hall plot, as illustrated in Fig. 20(b) and (c), where a slight decrease in ε is observed. The acquisition of ε by the Williamson–Hall plot reflects the microstrain in terms of bulk film and provides limited strain information as a function of the depth (strain inhomogeneity along the out-of-plane direction).

Small molecules in the absence of selective contact (directly on TCO). Recently, self-assembled molecules (SAMs) have been widely used as hole transport materials (HTMs) in inverted PSCs. Because the most common transparent conducting oxide (TCO) electrodes (fluorine-doped SnO₂ (FTO) and indium-doped SnO₂ (ITO)) are basically based on SnO₂, SAMs utilized in the inverted structure significantly resemble the aforementioned small

This journal is © The Royal Society of Chemistry 2025

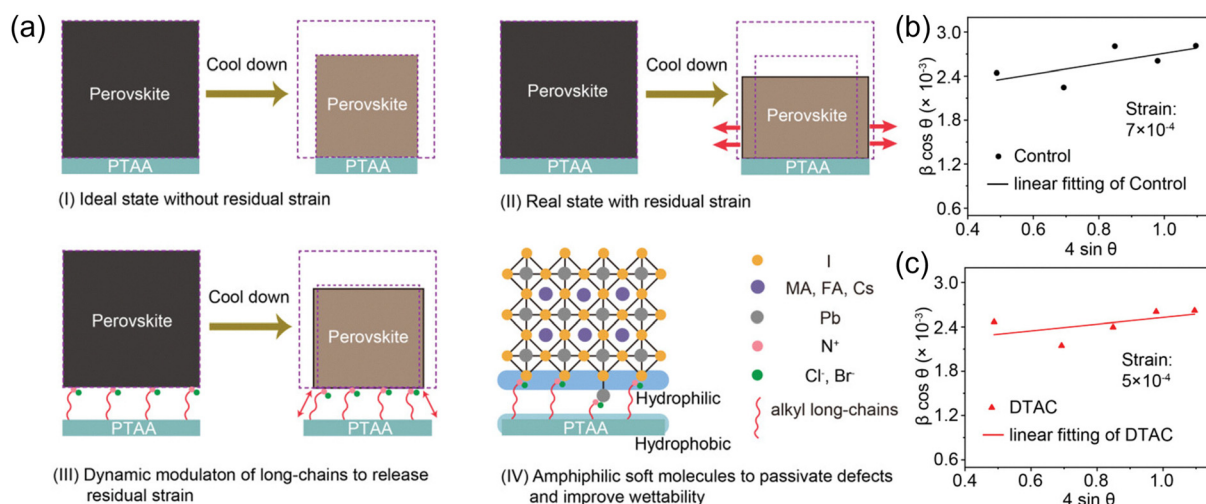*Chem. Soc. Rev.*, 2025, **54**, 7870–7912 | **7891**

Fig. 20 (a) Schematic of strain effect during cooling after the annealing of perovskite films for (I) ideal state and (II) real state. (III) Strain release by introducing a buffer layer using soft molecules with long alkyl chains, with the (IV) defect passivation effect. $\beta\cos\theta - 4\sin\theta$ plots of perovskite films deposited on (b) PTAA (control) and (c) DTAC-coated PTAA, with linear fitting to calculate strain by the slope. Reproduced with permission from ref. 169. Copyright 2022, Wiley-VCH.
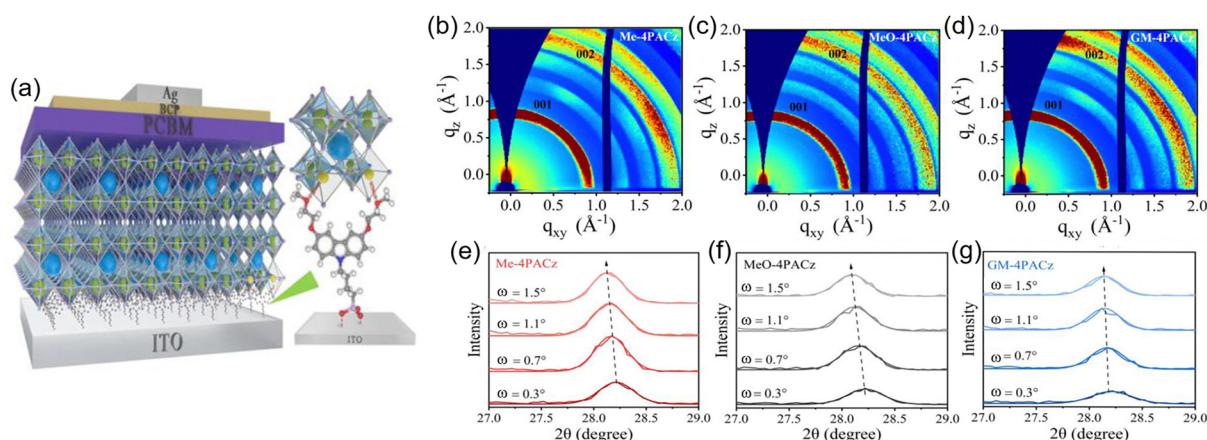

Fig. 21 (a) Schematic of SAM interaction between the substrate and perovskite. GIWAXS images of perovskite films on (b) Me-4PACz, (c) MeO-4PACz, and (d) GM-4PACz substrates. GIXRD spectra of perovskite films on (e) Me-4PACz, (f) MeO-4PACz, and (g) GM-4PACz substrates. Reproduced with permission from ref. 173. Copyright 2024, Wiley-VCH.

molecules sandwiched between metal oxide substrate and perovskite to relieve the in-plane tensile strain at the bottom interface, particularly in terms of functional groups. SAMs consist of head and tail functional groups, which can form strong interactions with perovskite and TCO, respectively, and a linker that connects the head and tail groups. Phosphate (–PO(OH)$_2$) is a dominant functional group to anchor the SAMs in TCO.[171] However, carbazole-based functional groups are prevalently employed to form an interaction with the upper perovskite film while modulating the surface work function.[172] To this end, [2-(3,6-dimethoxy-9H-carbazol-9-yl)ethyl]phosphonic acid (MeO-2PACz), 4-(3,6-dimethyl-9H-carbazol-9-yl)butyl]phosphonic acid (Me-4PACz) and [4-(3,6-dimethoxy-9H-carbazol-9-yl)butyl]phosphonic acid (MeO-4PACz), consisting of phosphate and carbazole, are the most representative SAMs that have been widely used in the

inverted PSCs. Fig. 21(a) illustrates the inverted structure that employs a new SAM, 4-(3,6-glycol monomethyl ether-9H-carbazol-9-yl)butyl]phosphonic acid (GM-4PACz), with functional groups of phosphate for ITO adhesion and glycol monomethyl ether, instead of the conventional carbazole-based group, for interacting with perovskite.[173] GM-4PACz-coated ITO results in a smoother surface than ITO/Me-4PACz and ITO/MeO-4PACz, which is responsible for the improved crystallinity of the perovskite film, as confirmed by the brightest diffraction ring from GIWAXS analysis (Fig. 21(b)–(d)). The improved crystallinity along with enhanced orientation, particularly as monitored from the (002) diffraction ring, of the perovskite film grown on GM-4PACz is highly favorable for reducing the local strain heterogeneity even on a grain scale based on the relatively ordered structure. From the perspective

7892 | *Chem. Soc. Rev.*, 2025, **54**, 7870–7912

This journal is © The Royal Society of Chemistry 2025

of collective strain inhomogeneity across the bulk film, the perovskite film grown on the conventional SAMs, Me-4PACz (Fig. 21(e)) and MeO-4PACz (Fig. 21(f)), still suffers from the in-plane lattice strain at the bottom interface, as indicated by the shift of Bragg 2θ toward lower angle with increasing ω using the iso inclination method. Notably, the use of SAMs still prevents the perovskite lattice from being fully unaffected by the intrinsic substrate of ITO underneath the SAM. The extremely thin layer, ideally a monolayer of Me-4PACz and MeO-4PACz, seems insufficient to handle the in-plane tensile strain raised by the thermal expansion coefficient mismatch between the upper perovskite and the under ITO.[174] However, GM-4PACz is effective in releasing the residual strain by showing a limited shift of 2θ as ω increases, which is ascribed to the flexible ether chain at the 3,6-positions of 4PACz.[173]

Small molecules on the SAM layer. Uneven coverage of SAMs on ITO accelerates the hindrance to the uniform growth of the perovskite film,[175] which hinders the perovskite film from growing uniformly. Phenylethylammonium chloride (PEACl) is employed as a flexible buffer layer not only to prevent direct adhesion between MeO-2PACz and perovskite but also to enhance the surface energy compared to MeO-2PACz, which is favorable for accommodating lattice mismatch between the perovskite and the substrate. The halide component of Cl^- in PEACl is prone to fill the I^- vacancy of the perovskite surface, while the NH^{3+} group of PEACl forms a coordination bond with Pb^{2+}.[176] By the aid of passivated vacancies based on the strong interaction, the PEACl interlayer plays a beneficial role in releasing the residual in-plane tensile strain by reducing lattice mismatch, as illustrated in Fig. 22(a).[177] Fig. 22(b) and (c) show the GIXRD results based on the iso-inclination method. The prominent tensile strain at the bottom of the perovskite film,

indicated by a decrease in 2θ as ω increases in the control film (Fig. 22(b)), is significantly relieved by employing PEACl, resulting in almost invariant 2θ (Fig. 22(c)).

7.2.2. Polymer as an in-plane strain reliever

Polymer on the metal oxide layer. Polymer substrate can be preferred in terms of thermal expansion coefficient, which is closer to that of perovskite film compared to that of metal oxide.[168,178,179] Therefore, various polymers are introduced between the soft perovskite film and rigid metal oxide substrate to reduce the extent of thermal contraction. A formation of a composite between polymer and SnO_2 is proposed to control the residual strain. Polyacrylic acid (PAA) is mixed into SnO_2 quantum dots (QDs) to prevent the agglomeration of QDs and to reduce oxygen vacancies caused by hydroxyl separation during the annealing process.[180] The oxygenic group of PAA bonds with uncoordinated Sn^{4+} and fills the oxygen vacancies of both FTO and SnO_2 QDs, forming a hard SnO_2 film with few microcracks.[181] Additionally, PAA serves as a buffer spring to release the residual strain at the interface and passivates two adjacent layers with functional groups responding to oxygen vacancies of SnO_2 and the Pb dangling bonds.[182] As shown in Fig. 23(a), PAA is present at the interface as an interlayer and diffuses into the perovskite bulk along the vertical grain boundaries owing to a relatively low volatility temperature of PAA ($\sim$200 °C) compared to the high annealing temperature (250 °C) of the $CsPbBr_3$ film according to the mechanism, as depicted in Fig. 23(b).[183] Fig. 23(c) and (d) show the analysis of GIXRD using the iso-inclination method, where the dependence of 2θ on ω (dashed guideline) greatly dwindles by employing PAA. The gentle slope in the converted d–ω plot depicted in Fig. 23(e) accordingly indicates the relaxation of the residual in-plane strain, that is the suppression of strain inhomogeneity along the depth of the perovskite film grown
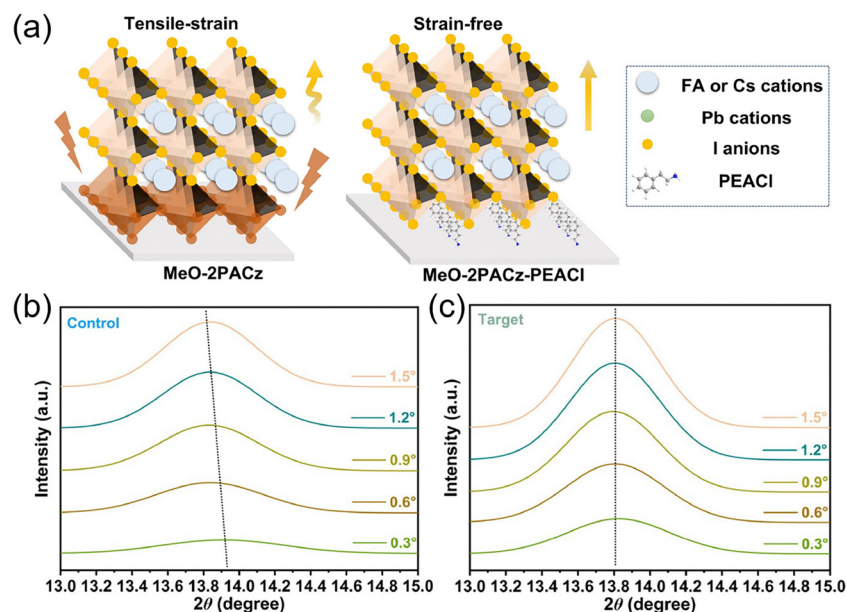

Fig. 22 (a) Schematic of the lattice strain of perovskite grains deposited on MeO-2PACz and MeO-2PACz/PEACl substrates. GIXRD spectra of perovskite films on (b) MeO-2PACz and (c) MeO-2PACz/PEACl. Reproduced with permission from ref. 177. Copyright 2024, Wiley-VCH.

This journal is © The Royal Society of Chemistry 2025

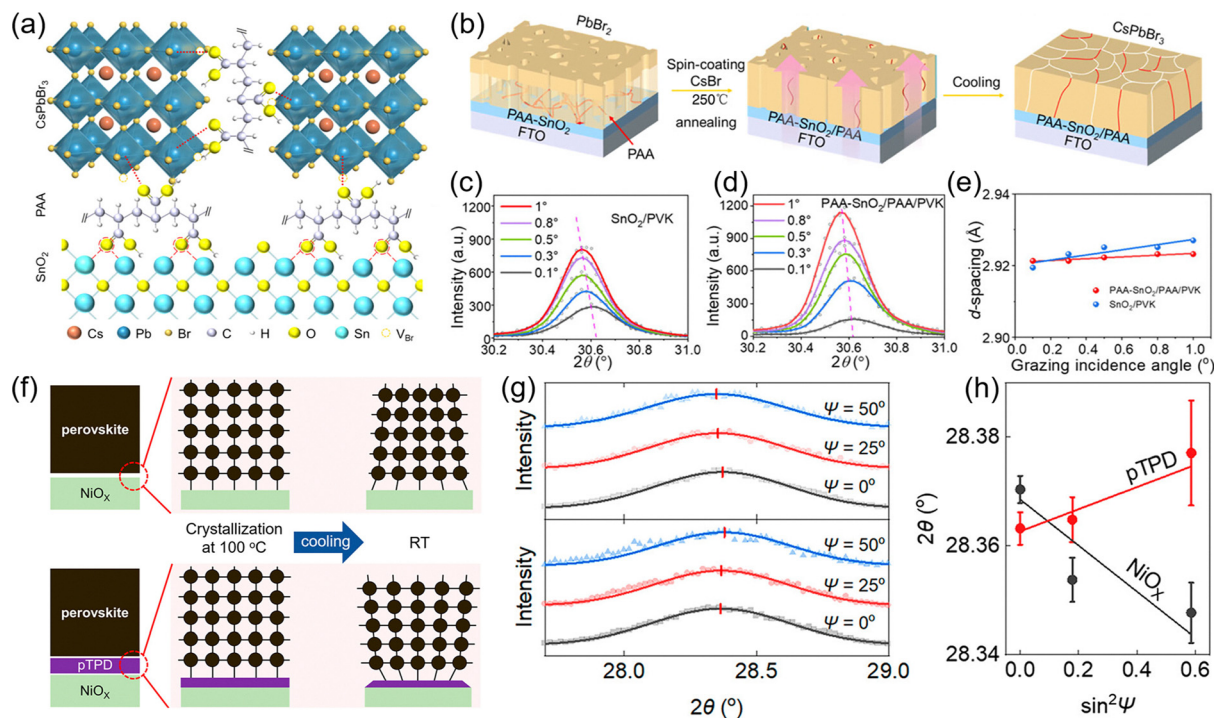*Chem. Soc. Rev.*, 2025, **54**, 7870–7912 | **7893**

Fig. 23   (a) Schematic of defect passivation by PAA at the bottom interface and grain boundaries of the perovskite film. (b) Schematic of the passivation and diffusion of PAA along the grain boundaries of the perovskite film. GIXRD spectra of the perovskite film on (c) SnO_2 and (d) on PAA–modified SnO_2. (e) d–ω plots with linear fitting depending on PAA. Reproduced with permission from ref. 183. Copyright 2023, Wiley-VCH. (f) Schematic of perovskite lattice strain development depending on the substrate. (g) GIXRD spectra of perovskite film on NiOx (top) and pTPD (bottom). (h) Linear fitting of 2θ–$\sin^2\Psi$ depending on the substrate. Reproduced with permission from ref. 185. Copyright 2022, American Chemical Society.

on PAA.[183] Furthermore, the inverted structure employing NiOx as an HTM is similarly modulated with a polymer, poly(4-butyl-phenyldiphenylamine) (pTPD). Although a great difference in thermal coefficients of NiOx (14.0×10^{-6} K^{-1})[178] and FAPbI$_3$ (98.6–100×10^{-6} K^{-1})[51] readily leads to the in-plane tensile strain at the bottom perovskite lattice, pTPD with a higher thermal expansion coefficient (1.0×10^{-3} K^{-1} above 60 °C and 1.2×10^{-4} K^{-1} below 60 °C)[184] can even ideally induce the in-plane compressive strain, as illustrated in Fig. 23(f). The residual strain is characterized by applying the side-inclination method GIXRD, which clearly shows the distinct shift patterns of 2θ as Ψ increases depending on the pTPD interlayer (2θ shifts toward lower and higher angle without (upper figure) and with pTPD (lower figure), respectively, as depicted in Fig. 23(g)).[185] The 2θ–$\sin^2\Psi$ graph shown in Fig. 23(h) estimates σ of 0.0164 for NiOx substrate and -0.0079 for pTPD substrate, where positive and negative values indicate tensile and compressive strain, respectively.[25] The effective regulation of the lattice in-plane strain from tensile to compressive using the polymer emphasizes the importance of considering the thermal expansion coefficient of the substrate for the solution-processed perovskite crystal growth but still would not guarantee the superior properties in terms of photovoltaic performance.

Polymer in the absence of an underlying layer (polymer on TCO). PTAA is dominantly used as a polymeric HTM for the inverted structure of PSCs, but it has intrinsic limitations, such

as strong aggregation and poor wettability.[174,186,187] One of the main issues in the inverted structure based on PTAA is processibility. The strong hydrophobic surface of PTAA tends to aggregate and prevents the precursor solution of perovskite from wetting, leading to a rough perovskite film with poor coverage, with nanovoids at the bottom surface image of the perovskite film (Fig. 24(a)).[188] PTACz-PO is devised to overcome the wettability issue by employing diethyl phosphate groups. The increased polarity of PTACz-PO is beneficial for improving wettability and consequently enhances the passivation effect on the bottom surface of the perovskite film, resulting in a neat interface when compared between Fig. 24(a) and (b). The increased polarity of PTACz-PO even enables the conventional solvent, chlorobenzene (CB), with methyltetrahydrofuran (MeTHF), where the pre-aggregation of the PTACz-PO with 10.34 nm in CB is considerably inhibited by forming 0.43 nm-sized particles when dissolved in MeTHF. This indicates that PTACz-PO tends to aggregate in CB, while in MeTHF, pre-aggregation is significantly reduced.[186] Therefore, the buried interface of the perovskite film grown on the PTACz-PO layer exhibits larger grain sizes when using MeTHF as a solvent for the polymer, compared to CB as the solvent (Fig. 24(b) and (c)). Along with the enhanced crystallinity and morphology of the perovskite film, PTACz-Po based on diethyl phosphate exhibits a remarkable effect on releasing in-plane residual stress.[186] GIXRD patterns, obtained by varying Ψ from 0° to 50° in the side-inclination method, estimate the most intense in-plane

7894 | *Chem. Soc. Rev.*, 2025, **54**, 7870–7912

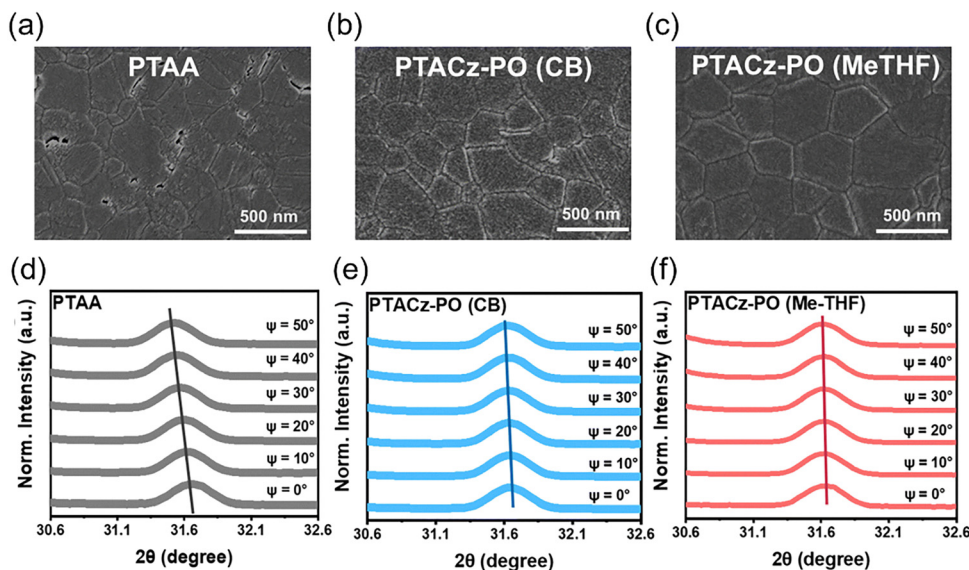This journal is © The Royal Society of Chemistry 2025

Fig. 24 SEM images of the buried interface of perovskite films grown on (a) PTAA, (b) CB-processed PTACz-PO, and (c) MeTHF-processed PTACz-PO. GIXRD spectra of perovskite films grown on (d) PTAA, (e) CB-processed PTACz-PO, and (f) MeTHF-processed PTACz-PO. Reproduced with permission from ref. 186. Copyright 2025, Royal Society of Chemistry.

tensile strain from the PTAA substrate with a prominent Ψ-dependent 2θ shift (Fig. 24(d)). The shift extent is reduced by replacing the PTAA with PTACz-PO (Fig. 24(e)), while almost negligible variation in 2θ is observed when replacing the solvent for PTACz-PO from CB to MeTHF (Fig. 24(f)). The residual strains obtained by 2θ–$\sin^2\Psi$ are 49.51 MPa, 13.56 MPa, and 7.70 MPa for PTAA, CB-processed PTACz-PO, and MeTHF-processed PTACz-PO, respectively.

7.2.3. Inorganic materials as in-plane strain relievers. Although small molecules and polymers mostly serve as strain relievers with a flexible core structure forming an interlayer, inorganic materials tend to induce a selective lattice contraction at the bottom to release the in-plane tensile strain either by doping or by involving pre-compressive strain.

It reveals that doping of the perovskite lattice with alkali metal cations can alter the lattice strain.[59,189] When rubidium dihydrogen phosphate (RbDP) is introduced into the SnO_2, Rb^+ is prone to diffuse into the perovskite lattice during the perovskite crystallization process, as illustrated in Fig. 25(a),[121] owing to the lower adsorption energy of Rb^+ on the SnO_2 surface.[190] X-ray photoelectron spectroscopy (XPS) spectra of the perovskite layer show signals of Rb and P, confirming the diffusion of RbDP, although the depth of diffusion remains unclear.[121] Furthermore, XRD peak corresponding to the crystal planes of (110) and (220) exhibits a slight shift to a higher angle, indicating a decrease in d likely due to a partial replacement of FA^+ (an ionic radius of 2.79 Å) with Rb^+ (an ionic radius of 1.52 Å) for lattice contraction.[121,191–193] As depicted in Fig. 25(b), the pristine perovskite film exhibits a gradual shift of 2θ toward a lower angle as Ψ increases, implying a larger d near the bottom interface of perovskite, compared to the upper lattice, which is in accordance with the routine in-plane residual strain. The incorporation of RbDP at the bottom interface

of the perovskite film notably induces a slight shift in 2θ toward higher angle as Ψ increases, which confirms the effective role of RbDP in regulating the residual in-plane strain type in the perovskite lattice from tensile- to compressive-strain.[121] The tensile strain is modulated by the synergistic effects of $H_2PO_4^-$ and Rb^+, wherein $H_2PO_4^-$ interacts with SnO_2 and uncoordinated Pb^{2+}, while the diffusion-induced Rb^+ doping substitutes FA^+. The reduction in d occurs more prominently near the bottom interface, nullifying the formation of in-plane tensile strain. Similarly, the in-plane lattice strain of the perovskite film can be relieved by inducing selective lattice contraction near the bottom. For the case of $CsPbBr_3$ film, the lattice contraction at the bottom film can be pursued by incorporating Cl^- with a smaller ionic radius to replace Br^-, as illustrated in Fig. 25(d).[194] CsCl is employed in SnO_2, where the increased interplanar spacing of SnO_2 with CsCl suggests that Cs^+ is well distributed within the SnO_2 lattice.[194] Owing to the smaller ionic radius of Cl^- compared to Br^-, a strong electronic coupling between Pb^{2+} and Cl^- occurs and consequently induces the lattice contraction at the bottom.[194] Time-of-flight secondary ion mass spectrometry (TOF-SIMS) confirms that Cl^- components are selectively distributed at the interface of SnO_2/$CsPbBr_3$.[194] The Cl^--induced lattice contraction at the bottom can facilitate uniform crystal growth and mitigate strain inhomogeneity along the out-of-plane direction by attenuating depth-dependent d mismatch.[194] As illustrated in Fig. 25(e) and (f), the residual strains of perovskite grown on SnO_2 and $CsCl$–SnO_2 substrate are compared, where the pronounced shift in 2θ toward higher angle is slightly eased using the $CsCl$–SnO_2 substrate, confirming the relieved in-plane tensile strain.[194]

A strategy of pre-strain, which is intentionally introduced to the material prior to completion of the process, can be applied

This journal is © The Royal Society of Chemistry 2025

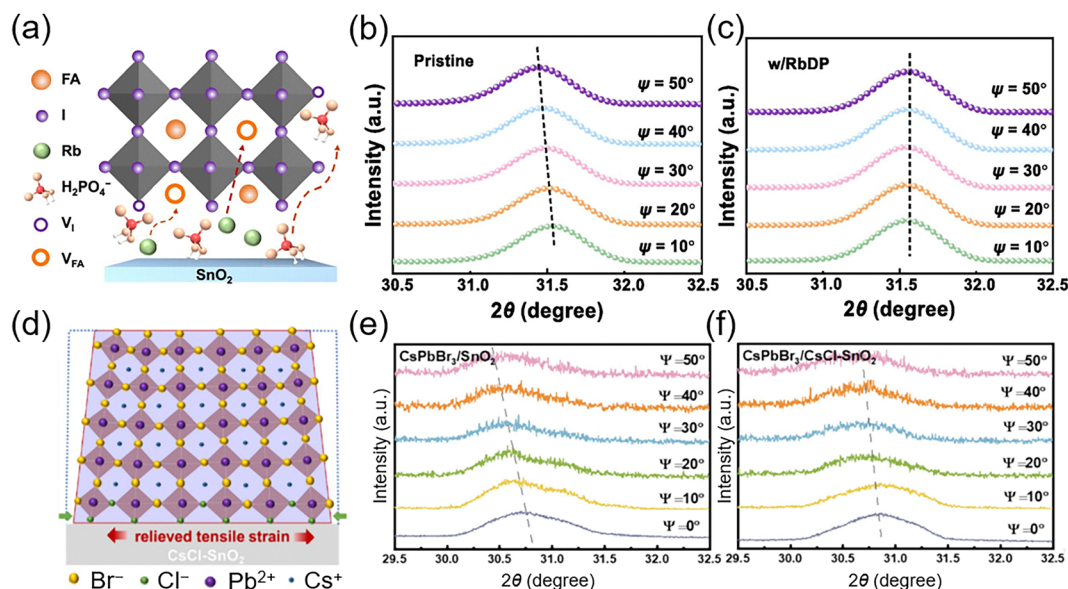Chem. Soc. Rev., 2025, **54**, 7870–7912 | 7895

Fig. 25 (a) Illustration of RbDP diffusion into the perovskite layer. GIXRD patterns of (b) control and (c) RbDP-modified perovskite films. (d) Schematic of the bottom interface when CsCl is incorporated in SnO_2. GIXRD patterns of perovskite films grown on (e) SnO_2 and (f) $CsCl-SnO_2$. Reproduced with permission from ref. 121. Copyright 2024, Elsevier and 194 Copyright 2024, Elsevier.
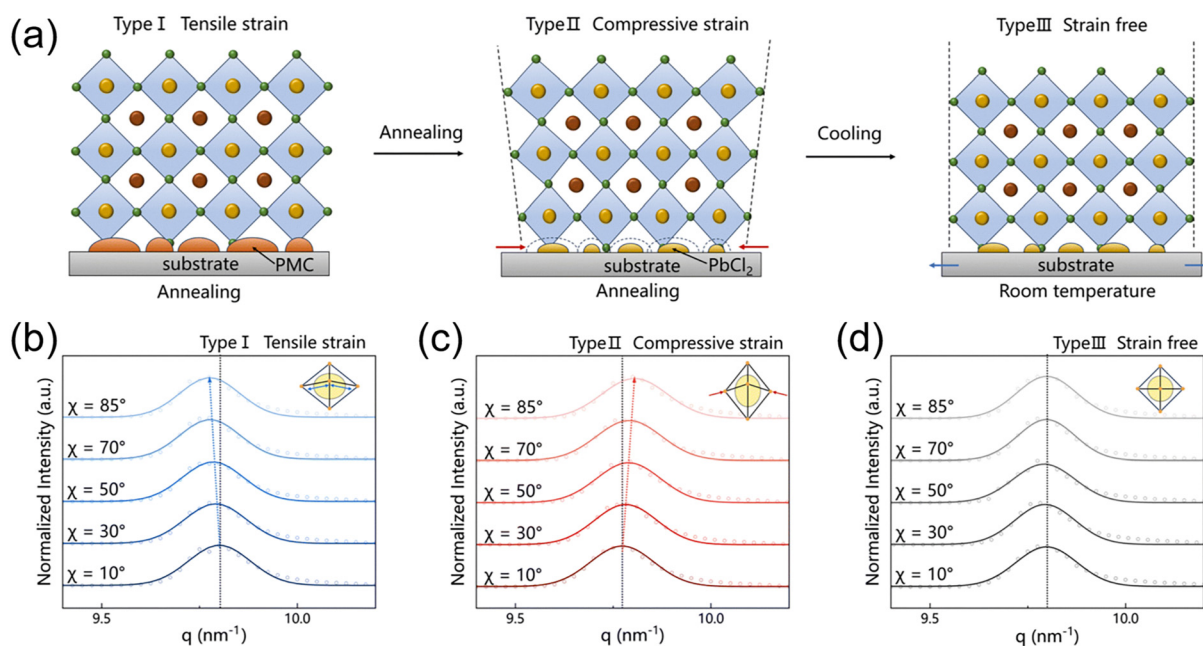

Fig. 26 (a) Illustration of the mechanism of the pre-strain strategy. GIWAXS of the (100) plane at different χ angles for (b) type 1, (c) type 2 and (d) type 3. Reproduced with permission from ref. 112. Copyright 2024, Royal Society of Chemistry.

to the bottom interface of perovskite films to regulate the residual lattice strain.[112] When the metastable material of $Pb(CH_3NH_3)_2Cl_2$ (PMC) is located at the interface between substrate and perovskite film, volatile MA^+ is evaporated during the annealing process, forcing the bottom lattice of the perovskite film to contract (the left side of Fig. 26(a)).[112] During the subsequent cooling process, the upper lattice of perovskite freely shrinks unlike the bottom lattice adhering to the substrate, which converts the in-plane compressive strain, in the

form of pre-strain, into a strain-free state (the right side of Fig. 26(a)).[112] This pre-strain concept is verified by grazing incidence wide-angle X-ray scattering (GIWAXS) along with TOF-SIMS. The conversion of PMC to $PbCl_2$ at the bottom interface of the perovskite film during the annealing process is evidenced by GIWAXS,[112] which is in accordance with the TOF-SIMS results, showing a gradual signal decrease for MA^+ while maintaining Cl^-.[112] Fig. 26(b)–(d) evidently illustrates the strain type conversion. As depicted in Fig. 26(b), the residual

in-plane tensile strain is confirmed by a shift of the (100) diffraction peak toward lower q, indicating larger d as χ increases. The formation of the pre-strain is shown in Fig. 26(c), where the reverse shift toward higher q with increasing χ implies that the pre-strain is revealed as in-plane compressive strain, which turns into a strain-free condition after cooling, as shown in Fig. 26(d).[112]

The chemicals used to release the residual in-plane tensile strain at the bottom interface of the perovskite film in Section 7.2 are summarized in Table 2, having related information on perovskite, strain and photovoltaic performance with long-term stability.

7.3. Strain control at the top interface

Materials deposited on top of the perovskite film can be similarly anchored to the top lattice and accordingly exert a strong interaction to formulate the residual lattice strain. Nevertheless, strain control at the top interface is not widely attempted because the fundamental origin of the residual in-plane lattice strain, causing the strain inhomogeneity along the out-of-plane direction, is inherent to the bottom interface. Therefore, the top interface approach is relatively limited compared to the bottom interface.

7.3.1. Small molecules as in-plane strain relievers. The residual tensile strain of the perovskite film is modulated by engineering its top surface with 2-(methylthio)ethylamine hydrochloride (2MTEAC). 2MTEAC has both an electron-donating group (–S as Lewis base) and an electron-withdrawing group (–NH^{3+} as Lewis acid), which are favorable for coordinating with undercoordinated Pb^{2+} and I or N of the top perovskite lattice, respectively, as illustrated in Fig. 27(a).[201] The effect of the top surface engineering on the residual strain of perovskite film is assessed by applying the side-inclination method, GIXRD, shown in Fig. 27(b)–(d). The target film with the surface treatment with 2MTEAC exhibits a relaxation of the scattering 2θ peak shift as Ψ increases (Fig. 27(c)) compared to the control film (Fig. 27(b)). The linear fitting shown in the 2θ–$\sin^2\Psi$ graph estimates the slopes of the control and the target films as $\varepsilon = 0.214$ and 0.173, respectively (Fig. 27(d)).[201] More specifically, an increased 2θ at higher $\sin^2\Psi$, indicating reduced d close to the bottom interface, is monitored from the target film, while d is even enlarged near the top interface of the target film by forming a strong interaction with the small molecules, confirming the relieved strain inhomogeneity along the out-of-plane direction for the 2MTEAC-treated target film. Furthermore, π-conjugated small molecules of aminobenzoic acid derivatives, *meta*-aminobenzoic acid (MABA) and *para*-aminobenzoic acid (PABA), are similarly introduced to the top surface of the perovskite film to passivate the defect and to release the residual in-plane tensile strain.[202,203] The two molecules consist of two bioactive-site ligands with π-conjugated systems, –NH_2 and –COOH, where the free movement of π-electrons occurs in the extended molecular orbital, and a lone pair electron can move from the strong electron donor –NH_2 group to the weak electron withdrawing –COOH group owing to π–π intermolecular interactions.[202] In addition, the presence of

both electron-rich and electron-donor ligands allows MABA and PBBA to passivate both negatively and positively charged defects (*e.g.*, uncoordinated Pb^{2+}, Br^- vacancy, and Cs^+ vacancy) in the perovskite film, as depicted in Fig. 27(e).[204] The iso-inclination method of GIXRD is used to confirm the effect of MABA- and PABA-treated perovskite films on the residual lattice strain. The control film in Fig. 27(f) exhibits an obvious peak shift of 2θ with increasing ω, implying the pronounced residual in-plane strain at the bottom region.[205] The peak shift is gradually relieved by the top surface engineering of perovskite film with MABA (Fig. 27(g)) and PABA (Fig. 27(h)), suggesting relieved strain inhomogeneity along the out-of-plane direction. It is noteworthy that the top surface engineering of the perovskite film by coordinating pertinent small molecules affords to wield distinct influence over the residual in-plane tensile strain, which dominantly originates from the bottom interface of the perovskite film although their effects on the related mechanism are not thoroughly discussed in the relevant studies.

Ligands of quantum dots (QDs) can also act as SAM on the perovskite surface and play a similar role in regulating the residual lattice strain. $CsPbI_3$ quantum dot (QD), capped with an optimal amount of ligand, is employed in toluene as an antisolvent, which is subsequently dropped on the spinning film with the $FA_{0.95}Cs_{0.05}PbI_3$ perovskite precursor solution, as illustrated in Fig. 28(a).[206] The ligand concentration is controlled by successive treatments with a mixed solvent of hexane and methyl acetate, where the strain degree varies with the ligand concentration. $CsPbI_3$ QDs mainly function as nucleation sites and are responsible for enhanced film quality, while the ligands are detached from the QD surface during the film annealing process and transferred to the surface of perovskite film, such as SAM, as confirmed by the shifted C=O stretching vibration of the oleic acid ligand from 1710 cm^{-1} in pure $CsPbI_3$ QDs to 1750 cm^{-1} in the perovskite film. It is noteworthy that the self-assembled ligands on the perovskite surface play a critical role in determining the residual lattice strain.[206] Fig. 28(b) presents the GIXRD pattern of the control film with the (012) plane, which is frequently selected to acquire more grain information than orientation impact.[142,206,207] As the Ψ angle increases, the peak shifts to a lower angle owing to the increased d of the (012) plane, suggesting in-plane tensile strain with increasing depth.[206] However, the ligand content readily governs the residual lattice strain ranging from compressive strain to strain-free and even to tensile strain by decreasing the ligand concentration from QDs-I (Fig. 28(c)) to QDs-II (Fig. 28(d)) and to QDs-III (Fig. 28(e)), as observed by 2θ peak shift direction with increasing Ψ. As illustrated in Fig. 28(f), the slope of the 2θ–$\sin^2\Psi$ plot indicates σ. When considering the negative slope of the control film as a reference point, the slope is widely varied from positive σ (compressive strain with QD-I) to negative σ (tensile strain with QD-III).

The chemicals used to release the residual in-plane tensile strain dominantly on the top surface of the perovskite film in Section 7.3 are summarized in Table 3 with related information on perovskite, strain and photovoltaic performance with long-term stability.

This journal is © The Royal Society of Chemistry 2025

Chem. Soc. Rev., 2025, **54**, 7870–7912 | 7897

Table 2 Chemicals employed at the bottom interface of the perovskite film to relieve out-of-plane strain inhomogeneity

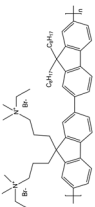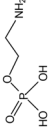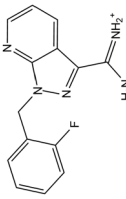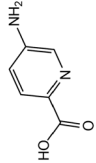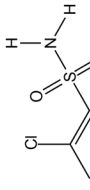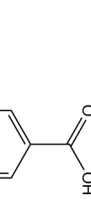| Chemical type	Chemical equation	Chemical structure	Interaction type	Perovskite	Other additives or passivation materials	Characterization	Strain type (control)	Strain type (target)	PCE (%)	Long-term stability	Long-term stress condition	Ref.
Polymer	Poly[9,9-bis(3′-(N,N-dimethyl)-nethylammoi-nium-propyl-2,7-fluorene)-alt-2,7-(9,9-dioctylfluorene)]dibromide (PFN-Br)		Coordinated bond	$Cs_{0.05}FA_{0.84}MA_{0.11}Pb(I_{0.86}Br_{0.14})_3$		GIXRD, Williamson–Hall	Compressive -112.2 MPa^c	Released compressive -39.8 MPa^c	21.93	$T_{97} =$ 240 h	mpp, one sun, N_2	23
Small molecule	Phosphorylethanolamine (PEA)			$(FA_{0.74}MA_{0.26})PbI_{1-x}Br_x$	OABr	GIXRD	Tensile -0.043 ± 0.007^a	Strain-free 0.009 ± 0.009^a	24.35	$T_{90} =$ 423 h	mpp, 0.95 sun, encapsulation, $\sim 40\%$ RH	102
Small molecule	1-(2-Fluorobenzyl)-1H-pyrazolo[3,4-b]pyridine-3-carboximidamide hydrochloride (FPPC)		Coordinated bond/hydrogen bond	$FAPbI_3$		GIXRD	Tensile 0.0034^b	Released tensile 0.0002^b	25.63	$T_{90} =$ 500 h	mpp, one sun, N_2	108
Small molecule	5-Aminopyridine-2-carboxylic acid (APC)		Coordinated bond, hydrogen bond, π–π bond, π–π stacking	$Cs_{0.05}FA_{0.85}MA_{0.10}Pb(I_{0.93}Br_{0.07})_3$	RbCl, TEACl	GIXRD, Williamson–Hall	Tensile 61.57 ± 6.92 MPa^c	Released tensile 27.54 $\pm$ 2.16 MPa^c	24.87	$T_{97} =$ 1800 h	mpp, one sun, N_2	110
Inorganic salt	$Pb(CH_3NH_2)_2Cl_2$ (PMC)		Coordinated bond	$FAPbI_3$	MACl	GIWAXS	Tensile 26.77 MPa^c	Strain-free -1.73 MPa^c	25.36	$T_{90} =$ 1000 h	mpp, one sun, N_2, $\sim 40\,^\circ C$	112
Small molecule	4-Chloro-3-sulfamoylben-zoic acid (CSBA)		Coordinated bond	$FA_{0.69}MA_{0.25}Rb_{0.06}PbI_3$	MeO-PEAI	GIXRD Williamson–Hall	Tensile 0.09752^b	Released tensile 0.0063^b	25.32	$T_{85} =$ 1200 h	One sun, N_2	120
Inorganic salt	RbH_2PO_4 (RbDP)		Coordinated bond	$FA_{1-x}MA_xPbI_3$		GIXRD Williamson–Hall	Tensile -0.105^a	Compressive 0.009^a	24.52	$T_{90} =$ 150 days	RT, RH $\sim 40\%$	121
Small molecule	3-Amino-5-bromopicolinal-dehyde (BD)		Coordinated bond/hydrogen bond	$Cs_{0.05}(FA_{0.95}MA_{0.05})_{0.95}Pb(I_{0.95}Br_{0.05})_3$		GIXRD	Tensile 48.8 MPa^c	Compressive -4.1 MPa^c	24.45	$T_{81} =$ 500 h	One sun, N_2	154

7898 | *Chem. Soc. Rev.*, 2025, **54**, 7870–7912

This journal is © The Royal Society of Chemistry 2025
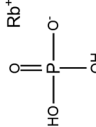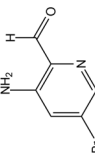
Table 2 (continued)

Chemical type	Chemical equation	Chemical structure	Interaction type	Perovskite	Other additives or passivation materials	Characterization	Strain type (control)	Strain type (target)	PCE (%)	Long-term stability	Long-term stress condition	Ref.
Small molecule	Bis(2,2,2-trifluoroethyl)(methoxycarbonylmethyl)phosphonate (BTP)		Coordinated bond/hydrogen bond	$Rb_{0.02}(FA_{0.95}Cs_{0.05})_{0.98}PbI_{2.91}Br_{0.03}Cl_{0.06}$		GIXRD	Tensile	Released tensile	24.26	$T_{54.5} = 1728$ h	One sun, N_2	155
Small molecule	DL-Cysteine hydrochloride monohydrate (DLCH)		Coordinated bond/hydrogen bond	$(FA_{0.95}Cs_{0.05})_{0.98}Rb_{0.02}Pb(Br_{0.03}Cl_{0.06}I_{2.91})$		GIXRD	Tensile	Released tensile	24.01	$T_{93} = 1800$ h	Dark, N_2, 65 °C	156
Small molecule	Ergothioneine (EGT)		Coordinated bond/hydrogen bond	$Rb_{0.02}(FA_{0.95}Cs_{0.05})_{0.98}PbI_{2.91}Br_{0.03}Cl_{0.06}$	PEAI	GIXRD	Tensile	Released tensile	25.13	$T_{90.1} = 930$ h	mpp, one sun	157
Small molecule	Cucurbit[5]uril (CB[5])		Coordinated bond	$Cs_{0.03}FA_{0.95}MA_{0.02}Pb(I_{0.975}Br_{0.025})_3$		GIXRD	Tensile	Released tensile	24.83	$T_{87.5} = 1000$ h	mpp, under illumination, N_2	158
Small molecule	1-Adamantaneacetic acid (ADAA)		Coordinated bond	$Rb_{0.02}(FA_{0.95}Cs_{0.05})_{0.98}PbI_{2.91}Br_{0.03}Cl_{0.06}$		GIXRD	Tensile	Released tensile	22.83	$T_{92.4} = 1000$ h	N_2, dark, 65 °C	159
Small molecule	2-Butynoic acid (BA)		Coordinated bond	$FA_{0.85}Cs_{0.15}PbI_3$		GIXRD	Tensile -0.117^a	Released tensile -0.109^a	23.33	$T_{72} = 500$ h	mpp, one sun, RH (40 ± 10%)	160
Small molecule	Hexadecyltrimethylammonium chloride (CTAC)		Coordinated bond	$Rb_{0.05}Cs_{0.05}MA_{0.05}FA_{0.85}Pb(I_{0.95}Br_{0.05})_3$		Williamson–Hall	Tensile $7.0 \times 10^{-4\,d}$	Released tensile $3.5 \times 10^{-4\,d}$	22.04	$T_{73} = 1200$ h	Encapsulation, 1.0 cm2, one sun	166
Small molecule	Piperazine dihydriodide (PDI$_2$)		Coordinated bond	$Cs_{0.05}FA_{0.87}MA_{0.08}Pb(I_{0.97}Br_{0.03})_3$		GIXRD	Tensile -0.1035 ± 0.0132^a	Released tensile -0.0524 ± 0.0089^a	23.47			168
Small molecule	Dodecyltrimethylammonium chloride (DTAC)			$Cs_{0.05}FA_{0.81}MA_{0.14}Pb(I_{0.86}Br_{0.14})_3$		Williamson–Hall	Tensile $7 \times 10^{-4\,d}$	Released tensile $5 \times 10^{-4\,d}$	19.7	$T_{84} = 6200$ h	~65 °C	169

This journal is © The Royal Society of Chemistry 2025

Chem. Soc. Rev., 2025, 54, 7870–7912 | 7899

Table 2 (continued)

Chemical type	Chemical equation	Chemical structure	Interaction type	Perovskite	Other additives or passivation materials	Characterization	Strain type (control)	Strain type (target)	PCE (%)	Long-term stability	Long-term stress condition	Ref.
Small molecule	[4-(3,6-Glycol monomethyl ether-9H-carbazol-9-yl]butyl]phosphonic acid (GM-4PACz)		Coordinated bond, hydrogen bond	$(FA_{0.95}MA_{0.05})_{0.95}Cs_{0.05}Pb(I_{0.95}Br_{0.05})_3$		GIXRD	Tensile Me-4PACz: 35.88 MPa^c MeO-4PACz: 51.83 MPa^c	Released tensile 23.31 MPa^c	25.52	T_{91} = 1000 h	mpp, one sun, N_2	173
Small molecule	Phenylethylammonium chloride (PEACl)		Coordinated bond	$Cs_{0.15}FA_{0.85}PbI_3$		GIXRD	Tensile	Released tensile	24.11	T_{97} = 1500 h	Tracking under 0.9 V, one sun, N_2	177
Polymer	Poly(acrylic acid) (PAA)		Coordinated bond (with Sn)	$CsPbBr_3$		GIXRD	Tensile	Released tensile	10.83	T = 100 h	mpp, LED (100 mW cm^{-2})	183
Polymer	Poly(4-butylphenyldiphenylamine) (pTPD)			$Cs_{0.05}FA_{0.83}MA_{0.12}Pb(I_{0.88}Br_{0.12})_3$		GIXRD	Tensile -0.04235 ± 0.02084^a	Compressive 0.02035 ± 0.00749^a		T = 911 h	Dry air (~745 h) RH (35-45%) (745-911 h)	185
Polymer	PTACz-PO			$Cs_{0.05}(FA_{0.95}MA_{0.05})_{0.95}Pb(I_{0.95}Br_{0.05})_3$		GIXRD	Tensile 49.51 MPa^c	Released tensile 7.70 MPa^c	26.31	T_{94} = 1450 h	65 °C, 50% RH, one sun	186
Inorganic salt	CsCl			$CsPbBr_3$		GIXRD	Tensile	Released tensile	11.16	1000 h	One sun, ambient air	194
Small molecule	4-Sulfobenzoic acid monopotassium salt (K-SBA)		Coordinated bond	$FA_{1-x}MA_xPbI_3$		GIXRD	Tensile -0.16465^a	Released tensile -0.02928^a	24.56	T_{90} = 500 h	mpp, one sun, N_2, 50-60 °C	195
2D perovskite	PEA_2PbBr_4			$CsPbBr_3$		STEM (strain mapping)	Strain ~ 6%^{e}	Strain ~ 2%^{e}				196
Small molecule	Rb_2CO_3			$FA_{0.93}Cs_{0.07}PbI_3$		GIXRD	Tensile 0.7 MPa^c	Compressive -38 MPa^c	22.7	T_{95} = 2700 h	mpp, one sun, N_2	197

7900 | Chem. Soc. Rev., 2025, 54, 7870-7912

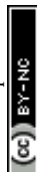This journal is © The Royal Society of Chemistry 2025

Table 2 (continued)

Chemical type	Chemical equation	Chemical structure	Interaction type	Perovskite	Other additives or passivation materials	Characterization	Strain type (control)	Strain type (target)	PCE (%)	Long-term stability	Long-term stress condition	Ref.
Small molecule	6FPPY			$FA_{0.95}Cs_{0.05}PbI_3$		GIXRD	Tensile −0.0195[a]	Released tensile 0.0044[a]	24	T_{90} = 200 h	mpp, one sun, N_2	198
Small molecule	p-Chlorobenzene-sulfonic acid (CBSA)		Covalent bond	$MAPbI_3$		GIXRD	Tensile −0.097[a]	Strain-free −0.013[a]	20.7	T_{84} = 3000 h	N_2	199
Small molecule	2-Thiopheneacetic acid (TPA)		Coordinated bond	$CsPbBr_3$		GIXRD	Tensile	Released tensile	11.23	T_{84} = 120 h	mpp, LED (100 mW cm^{-2})	200

[a] Value obtained from 2θ–$\sin^2\Psi$ plot (side-inclination method). [b] Value obtained from d–ω plot (iso-inclination method). [c] Value obtained from 2θ–$\sin^2\Psi$ plot according to eqn (4) (side-inclination method). [d] Value obtained from the Williamson–Hall graph slope. [e] STEM (strain mapping). mpp: maximum power point tracking; RH: relative humidity; RT: room temperature.

7.4. Strain control at grain boundaries

A flexible chain can bear strain and thus mitigate the strain in the system.[210] Small molecules with long alkyl chains, which cannot fit in the perovskite lattice, are expelled from the lattice during crystallization but remain at the grain boundaries as spacers.[99,104,106,211] The contribution of molecules sitting at grain boundaries to the lattice strain should be carefully assessed because the molecules unavoidably affect the lattice crystallization, thereby modulating the residual strain without accounting for the effect of molecules at the grain boundaries. This effect is closely related to the earlier-mentioned effect in subsection and Section '7.1. Strain control by regulating crystallization and 7.1.1. Additive strategy', respectively. Here, we attempt to consider the predominant effect (either crystallization or a certain role at grain boundaries) on strain control to distinguish and categorize the effect although a single molecule/material can sufficiently introduce multiple synergistic effects, and it is difficult to decouple the contribution extent.

Alkylamines with different chain lengths, n-butylamine (BA), n-hexylamine (HA), and n-octylamine (OA), are introduced as dopants in the perovskite precursor solution to regulate the lattice strain.[210] The electronegativity of HA is slightly higher than that of BA and OA.[210] The perovskite film incorporating HA can induce the strongest coordination interaction between the amino group of HA and Pb^{2+} in the perovskite film, which is responsible for an obvious peak shift of Pb 4f to lower binding energy in XPS analysis, compared to the control film without any dopant. The GIXRD pattern of the control film reveals a significant 2θ shift toward a lower angle with increasing ω (Fig. 29(b)), confirming the residual in-plane tensile strain in the control film. The in-plane tensile strain in the control film is most effectively relieved by the HA dopant, where the ω-dependent 2θ peak shift becomes less prominent (Fig. 29(c)).

The perovskite lattice at the grain boundaries is generally coordinated with ammonium ligands by hydrogen bonds, while intermolecular interaction between ammonium ligands is based on van der Waals interactions, where the ligands function as spacers to define grain boundaries.[212–214] Monoammonium ligands (n-octylamine iodide, OAI) and diammonium ligands (1,3-diaminopropane, DAP) with different alkyl chain lengths and different numbers of ammonium functional groups are also added in the perovskite precursor solution as additives. Monoammonium ligands with long alkyl chains (e.g., OAI) guarantee a wide grain boundary spacing capability but mostly rely on hydrogen bonding, coupled with weak van der Waals interactions.[134] However, diammonium ligands with short alkyl chains (e.g., DAP) can induce a strong interaction based on hydrogen bond at the grain boundaries while maintaining a narrow spacing between grains, where a migration of ions across the grain boundary can be facilitated owing to the narrow spacing.[215] Therefore, a mixed ammonium ligand passivation strategy, using OAI and DAP (OAI:DAP), is introduced to generate the synergistic effect of two ligands. Furthermore, OAI is prone to form a Ruddlesden–Popper (RP) 2D capping layer, which encourages the lattice stability while suppressing ion migration.[216] Meanwhile, the Dion–Jacobson (DJ) 2D lattice

This journal is © The Royal Society of Chemistry 2025

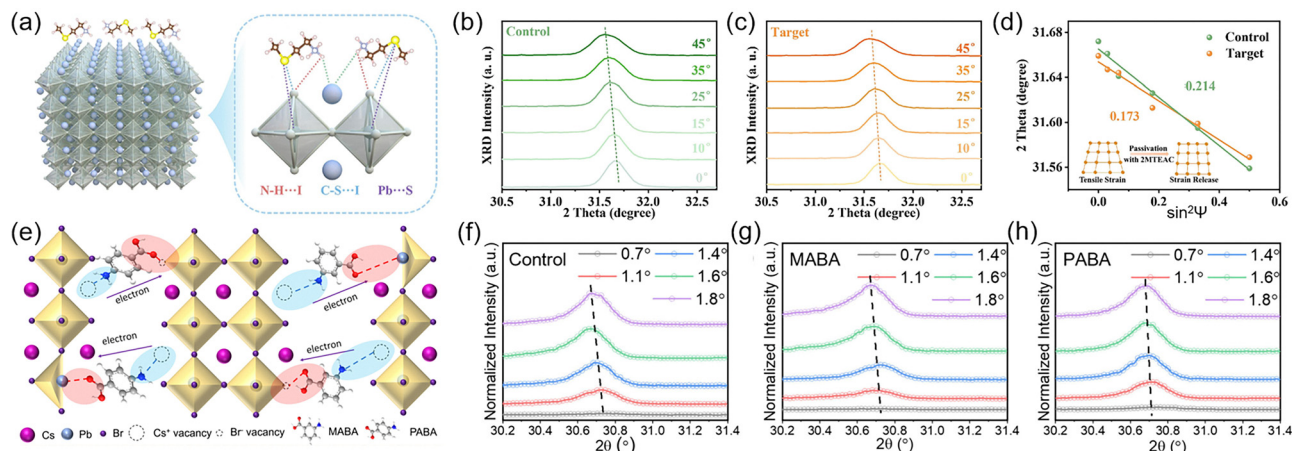Chem. Soc. Rev., 2025, **54**, 7870–7912 | 7901
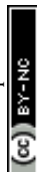
Fig. 27 (a) Schematic of the interaction between 2MTEAC and perovskite. GIXRD spectra of (b) control and (c) 2MTEAC-treated perovskite films. (d) Linear fit of $2\theta - \sin^2\Psi$ plots. Reproduced with permission from ref. 201. Copyright 2025, Elsevier. (e) Schematic of multifunctional passivation at different defect sites in $CsPbBr_3$ by MABA and PABA. GIXRD spectra of (f) control, (g) MABA-treated, and (h) PABA-treated perovskite films. Reproduced with permission from ref. 205. Copyright 2024, American Chemical Society.
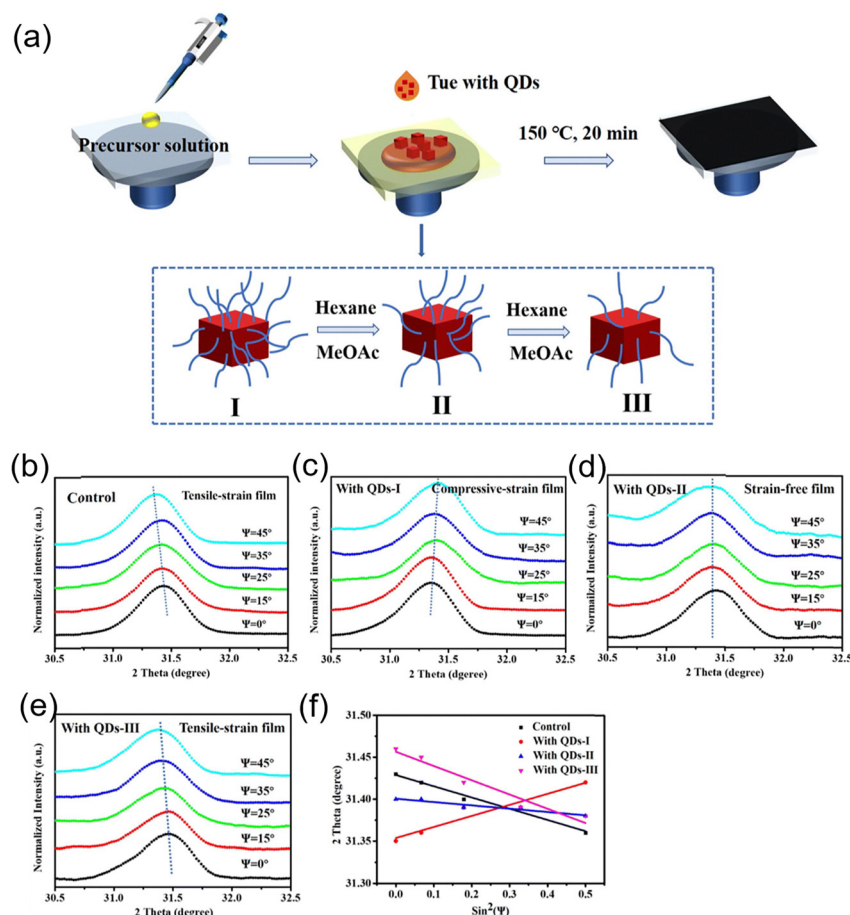
Fig. 28 (a) Schematic of the fabrication process of perovskite films with $CsPbI_3$ QDs, determining the number of surface ligands to modulate the lattice strain in the perovskite film. GIXRD patterns of (b) control film and films treated with (c) QD-I, (d) QDs-II, and (e) QDs-III. (f) Linear fit of $2\theta - \sin^2\Psi$ depending on the employment of the QDs. Reproduced with permission from ref. 206. Copyright 2023, Royal Society of Chemistry.

exhibits an overall opposite effect to the RP phase, facilitating charge transport but with reduced lattice stability.[212,213,216]

Microstrain is estimated by the Williamson–Hall method, as shown in Fig. 29(d), where the strain of the control film is most

7902 | Chem. Soc. Rev., 2025, 54, 7870–7912

This journal is © The Royal Society of Chemistry 2025

Table 3 Chemicals employed at the top interface of the perovskite film to relieve out-of-plane strain inhomogeneity

Chemical type	Chemical equation	Chemical structure	Interaction type	Perovskite	Characterization	Strain type (control)	Strain type (target)	PCE (%)	Long-term stability	Long-term stress conditions	Ref.
Small molecule	2-(Methylthio)ethylamine hydrochloride (2MTEAC)	[structure]	Coordinated bond/hydrogen bond	$(FA_{0.98}MA_{0.02})_{0.95}Cs_{0.05}Pb(I_{0.95}Br_{0.05})_3$	GIXRD	Tensile -0.214^a	Released tensile -0.173^a	24.52	$T_{90} = 1000$ h	N_2, 85 °C	201
Small molecule	*para*-Amino-benzoic acid (PABA)	[structure]	Coordinated bond	$CsPbBr_3$	GIXRD	Tensile	Released tensile	11.02	$T_{89} = 50$ days	85% RH, 25 °C	205
Inorganic QD	QD $CsPbI_3$			$FA_{0.95}Cs_{0.05}PbI_3$	GIXRD	Tensile	Strain-free	23.3	$T_{90} = 360$ h	55% RH, ambient air	206
Small molecule	1,1'-(Methylenedi-4,1-phenylene) bismaleimide, BMI	[structure]	Coordinated bond/hydrogen bond	$FA_{0.96}Cs_{0.04}PbI_3$	GIXRD	Tensile 6.2 Mpa^b	Compressive -7.4 Mpa^b	22.7	$T_{91.8} = 1000$ h	mpp, one sun, N_2	208
Small molecule	Organic polymer J71	[structure]	Coordinated bond	$CsPbI_2Br$	GIXRD TEM	Tensile -0.26897 ± 0.0093^a	Released tensile -0.19753 ± 0.0075^a	16.15	$T_{85} = 826$ h	N_2, 25% RH	209

^{a} Value obtained from 2θ–$\sin^2\Psi$ plot (side-inclination method). ^{b} Value obtained from 2θ–$\sin^2\Psi$ plot according to eqn (4) (side-inclination method). mpp: maximum power point tracking; RH: relative humidity.

effectively relieved by employing OAI with a long alkyl chain, while the DAP with a relatively short alkyl length is less effective in releasing the strain. Even though the microstrain has a limitation in evaluating the depth-dependent strain information, such as GIXRD, and simply possesses overall strain inhomogeneity, the relieved strain value certainly implies a more uniform strain distribution in the engineered film. Similarly, an extremely thin capping layer of the 2D perovskite is formed on 3D perovskite film (2D@3D) by incorporating 2-(2-pyridyl)ethylamine (2-PyEA), as shown in Fig. 29(e).[217] The ammonium functional group ($-NH_3^+$) can occupy the vacancy at the FA^+ site, while the N atom of pyridine interacts with the Pb^{2+} ions in the perovskite surface, resulting in the regulation of the surface termination and a partial relief of the residual tensile strain.[217] Therefore, the significant 2θ peak shift toward lower angle as Ψ increases in the control 3D film (Fig. 29(f)) is slightly relieved in the 2D@3D film (Fig. 29(g)), which is further alleviated by the post-treatment of the 2D@3D film with 2-PyEAI (2D@3D/2D), as shown in Fig. 29(h). Fig. 29(i) shows the molecular structure of 3-phosphonopropanoic acid (3-PPA), which is also used as a dopant in the precursor solution and simultaneously influences the residual lattice strain. The bilateral head group of 3-PPA stabilizes the octahedral lattice, while the alkyl chain alleviates the residual stress through the rotation of carbon–carbon single bonds at the grain boundaries.[152] The C=O and P=O bonds of 3-PPA coordinate with the Pb^{2+} ions of the perovskite, while the hydrogen bonds between 3-PPA and the N–H group of FA^+ are formed.[152] The GIXRD pattern of (001) planes in the control film shows a prominent 2θ shift toward a lower angle as ω increases (Fig. 29(j)), indicating the tensile strain. The strain inhomogeneity along the out-of-plane direction is considerably resolved in the target film (Fig. 29(k)), leading to a lower slope for the target film in the d–ω plot than that of the control film (Fig. 29(l)). Notably, relieved strain inhomogeneity is achieved by decreasing d at high ω (near the bottom interface) and by increasing d values near the top surface (at low ω) in the target film. The d values at low ω in the target film are even greater than those of the control film. In other words, 3-PPA enlarges the d of (001) particularly near the top interface, which readily contributes to the decrease in slope in the d–ω plots although the in-plane tensile strain is absolutely more involved at the top lattice of the target film.

The chemicals used to release the residual in-plane tensile strain dominantly at the grain boundaries of the perovskite film in Section 7.4. are summarized in Table 4, with related information on perovskite, strain and photovoltaic performance with long-term stability.

8. Synergistic effects of strain control

8.1. Improved optoelectronic properties and lattice stability

In terms of reducing the local strain inhomogeneity, the enhanced crystal orientation with a larger grain size is generally pursued by regulating crystallization to maintain structural homogeneity, where lattice deformation with octahedra tilting to afford the strain can be significantly suppressed.

This journal is © The Royal Society of Chemistry 2025

Chem. Soc. Rev., 2025, **54**, 7870–7912 | 7903

Fig. 29 (a) Molecular structure of BA, HA and OA. Depth-dependent GIXRD patterns of (b) pristine perovskite film and (c) film with HA. Reproduced 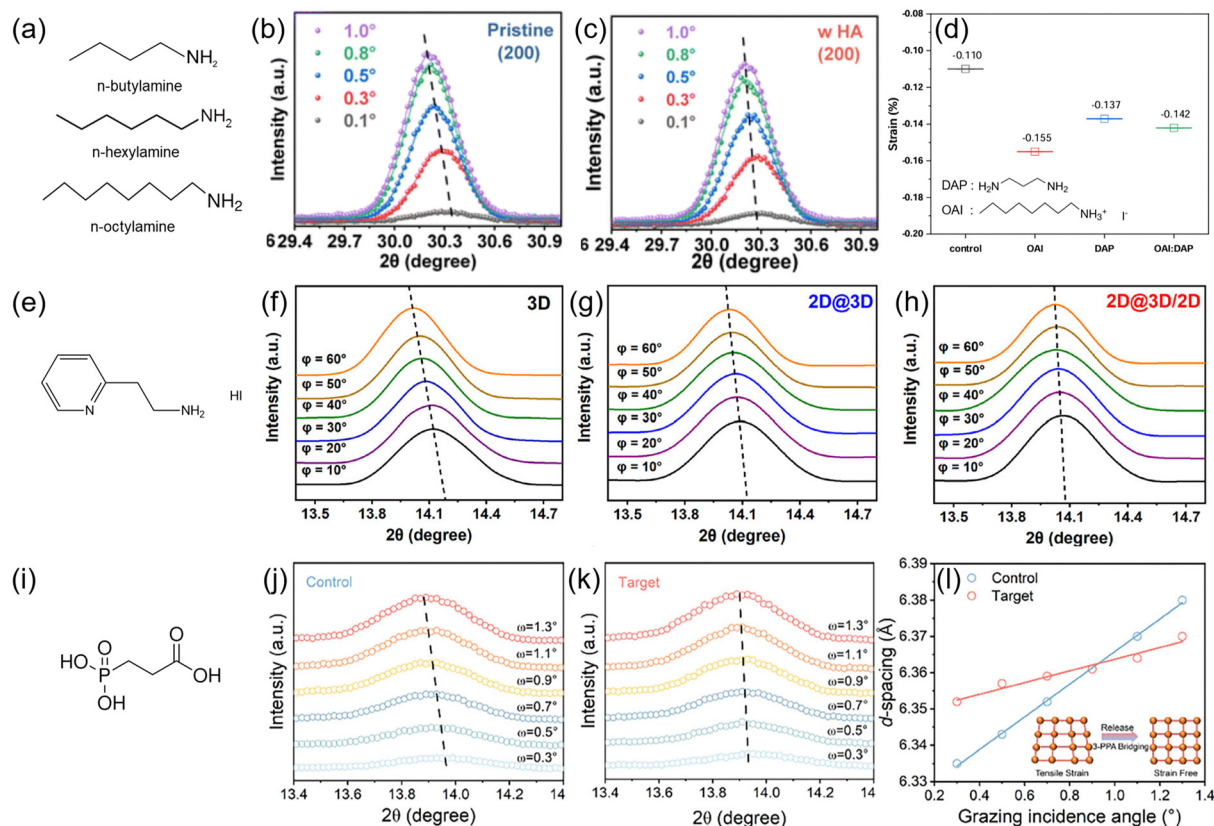with permission from ref. 210. Copyright 2024, Royal Society of Chemistry. (d) Microstrain in perovskite films containing OAI, OAI:DAP, and DAP. Reproduced with permission from ref. 211. Copyright 2023, Wiley-VCH. (e) Molecular structure of 2-PyEAI. GIXRD patterns of (110) planes in the perovskite film with (f) 3D (control), (g) 2D@3D, and (h) 2D@3D/2D. Reproduced with permission from ref. 217. Copyright 2023, American Chemical Society. (i) Molecular structure of 3-PPA. GIXRD patterns of (j) control and (k) target (containing 3-PPA) perovskite films. (l) $d-\omega$ plots with linear fitting. Reproduced with permission from ref. 152. Copyright 2024, Wiley-VCH.

Consequently, long-range effective overlapping between Pb–I–Pb with less PbI_6^{4-} octahedral tilting is enabled, which establishes a spatially independent uniform band structure. In the case of FAPbI₃, the cubic-like structure with suppressed lattice deformation is favorable for a strong spin–orbit coupling effect to suppress the carrier recombination,[222] as well as for light carrier effective masses to enhance charge transport properties.[223,224] Therefore, the long-range lattice order with uniform orientation by minimizing the local strain inhomogeneity is preferred for deriving superior optoelectronic properties and for ensuring performance reliability. Similarly, the residual lattice strain even intensifies the lattice deformation and readily affects the Pb–I bonding nature in the inorganic framework; hence, its electronic band structure, particularly the valence band, is accordingly altered with modulating optoelectronic properties.[60,62] It is noteworthy that even a small strain (about ±0.5%, positive value for the tensile strain and negative value for the compressive strain) can induce a noticeable physical change when considering a gradual change in the electronic band structure with varying strains.[26,27] It is assumed that the experimentally feasible strain window is limited to ±4%,[26-28,225] while the best performance is mostly

observed from the strain ranging from 0% (strain-free) to −1.5% (slightly compressive strain).[26-28] Generally, the residual in-plane tensile strain tends to form a dispersed curvature in the electronic valence band structure as a function of wave vector, while a large curvature results from the compressive strain. Therefore, in contrast with relatively constant electron effective mass, the hole effective mass significantly depends on the lattice strain, where the hole effective mass is gradually decreased by converting from tensile strain to strain-free, and to compressive strain.[28] The hole mobility thus gradually increases by strengthening the compressive strain until the critical dislocation occurs to nullify the intense compressive strain.[226] For the case of α-FAPbI₃, −1.2% of compressive strain is suggested as a compromise point between a low hole effective mass and a high trap density owing to the dislocation.[28] Besides, the residual strain is closely related to the defect dynamics,[227] where the activation energies for defect formation and migration are governed by the lattice strain. The compressive strain generally increases the activation energies for defect and migration, while the tensile strain helps defects form and migrate by decreasing the activation energies.[228] The high defect density under the in-plane tensile strain is well reflected

7904 | Chem. Soc. Rev., 2025, **54**, 7870–7912

This journal is © The Royal Society of Chemistry 2025

Table 4 Chemicals employed at grain boundaries of the perovskite film to release out-of-plane strain inhomogeneity

Chemical type	Chemical equation	Chemical structure	Interaction type	Perovskite	Characterization	Strain type (control)	Strain type (target)	PCE (%)	Long-term stability	Long-term stress conditions	Ref.
Small molecule	Pemirolast potassium, PP		Coordinated bond	$FA_{0.88}Cs_{0.12}Pb(I_{0.88}Br_{0.12})_3$	GIXRD	Compressive 0.405^a	Released compressive 0.305^a	23.06	$T_{90} = 250$ h	85 °C, N_2	24
Small molecule	3-Phosphonopropanoic acid (3-PPA)		Coordinated bond/hydrogen bond	$Cs_{0.05}FA_{0.95}PbI_3$	GIXRD	Tensile 0.045^b	Released tensile 0.016^b	24.05	$T_{86.4} = 1254$ h	Ambient air, 30–40% RH	152
Small molecule	n-Hexylamine		Coordinated bond	$CsPbIBr_2$	GIXRD	Tensile	Released tensile	10.67	$T_{79} = 100$ h	One sun	210
Small molecule	n-Octylammonium iodide, OAI/1,3-diaminopropane, DAP		Hydrogen bond	$Cs_{0.175}FA_{0.825}Pb(I_{0.85}Br_{0.15})_3$	Williamson–Hall	Compressive -0.110^d	Compressive -0.142^d	21	$T_{94} = 1000$ h	Encapsulation, one sun	211
Small molecule	2-(2-Pyridylthylamine (2-PyEA)		Coordinated bond/hydrogen bond	$FA_{0.75}MA_{0.25}PbI_3$	GIXRD	Tensile	Released tensile	23.2	$T_{92} = 3000$ h	RT, 30% RH, ambient air	217
Inorganic salt	Lead formate, PbFa		Coordinated bond	$(FAPbI_3)_{0.95}(MAPbBr_3)_{0.05}$	GIXRD Williamson–Hall	Tensile 38.5 MPa^c	Released tensile 27.09 MPa^c	24.32	$T_{90} = 300$ h	One sun, N_2	218
Small molecule	2,2′-Diamino-[1,1′-biphenyl]-4,4′-dicarboxylic acid, DBDA		Coordinated bond/hydrogen bond	$FA_{0.71}FA_{0.29}Pb(I_{0.88}Br_{0.22}Cl_{0.1})_3$	GIXRD	Tensile 0.0628^a	Compressive -0.1814^a	24.57	$T_{92} = 1000$ h	mpp, one sun, N_2	219
Small molecule	Methyl(methylsulfinyl)methyl sulfide, MMS		Coordinated bond	$Cs_{0.05}FA_{0.95}PbI_3$	GIXRD	Tensile 22.5 MPa^c	Released tensile 9.4 MPa^c	26.12	$T_{82} = 1650$ h	mpp, one sun, 30 ± 5% RH	220
Small molecule	Methylamine formate, MAFa			$FAPbI_3$	GIXRD, Williamson–Hall	Compressive -3.8 MPa^c	More compressive -13.9 MPa^c	24.08	$T_{90} = 1000$ h	30 ± 5% RH	221

^{a} Value obtained from the 2θ–$\sin^2\Psi$ plot (side-inclination method). ^{b} Value obtained from the d–ω plot (iso-inclination method). ^{c} Value obtained from the 2θ–$\sin^2\Psi$ plot according to eqn (4) (side-inclination method). ^{d} Value obtained from the Williamson–Hall graph slope.mpp: maximum power point tracking; RH: relative humidity; RT: room temperature.

This journal is © The Royal Society of Chemistry 2025

Chem. Soc. Rev., 2025, **54**, 7870–7912 | 7905

in the higher ideality factor of 1.55 compared to that of 1.05 under the compressive strain,[27] where the ideality factor varies from 1 for ideal radiative recombination to 2 for trap-assisted nonradiative recombination.[229] The strain-dependent defect dynamics is critically important for $FAPbI_3$ because the phase transition from α- to δ-phase should accompany atomic displacement in the soft lattice,[10] where the activation energy highly depends on the defect density.[230] Furthermore, the residual strain influences the unit cell volume in lattice, which can affect the lattice stability by H-driven change in G.[22] Therefore, the lattice strain control toward improving homogeneity and relieving the tensile strain, possibly leading to a decrease in G by the volume reduction in the unit cell, simultaneously exhibits enhanced optoelectronic properties and lattice stability as synergistic effects.

8.2. Defect passivation at the interface and grain boundaries

The lattice strain control is dominantly triggered by additives during crystallization or interfacial management (bottom, top, and grain boundaries) with specific materials, as discussed earlier. The additives for regulating crystallization contain functional groups to induce a strong interaction with precursors of perovskite (e.g., Pb^{2+}, I^-, and organic cation) and are subsequently situated at grain boundaries after completing the crystallization.[24,211] Similarly, the materials for interfacial management also consist of functional groups to interact with perovskite in common and optionally to interact with adjacent selective contact (electron or hole transport layer) depending on the target interface.[110,160] Therefore, the strategies for suppressing the strain inhomogeneity and relieving the in-plane tensile strain usually accompany chemicals employing specific functional groups, which can act as Lewis bases or acids (e.g., $-OPO(OH)_2$, $-NH_2$, $-NH_3^+$, $-C=O$, $-SH$, and $-COOH$) to efficiently coordinate with perovskite surface (e.g., Pb^{2+}, I^-, organic cation, and vacancies), resulting in surface passivation.[205,208] Because the interfacial defect predominantly serves as a main route for facilitating nonradiative carrier recombination,[231] the chemicals, which are utilized for modulating lattice strain, simultaneously suppress nonradiative recombination by coordinating with defect sites, as evidenced by increased photoluminescence lifetime and recombination resistance.[201,209,218] The interfacial defect passivation is, therefore, responsible for the increased PCE by reducing the energy loss and the enhanced long-term stability by stabilizing defects.

8.3. Favorable band energy alignment by interface management

Although the residual lattice strain would manipulate the band structure of the perovskite bulk film, the interface energy level alignment is mainly governed by the chemicals used to modulate the residual lattice strain at the interface of the perovskite.[120,159,195,218] The interfacial energy band alignment is generally estimated by Kelvin probe force microscopy for work function, ultraviolet photoelectron spectroscopy for valence band maximum, and UV-vis spectrometer for bandgap. The Fermi level of the selective contact is highly dominated by a change in the surface potential of the chemical-treated selective contact,[120] which is accordingly reflected in the energy alignment at the interface with varying energy offsets. Notably, the modified interfacial energy alignment is frequently found to either be favorable for charge extraction or effectively suppress the charge recombination at the interface,[120,159,195] contributing to improved photovoltaic performance.

9. Summary and perspective

Halide perovskite film exhibits a soft lattice, particularly for $APbI_3$, which can accommodate strain by undergoing lattice deformation based on octahedra PbI_6^- tilting. The polycrystalline nature of the perovskite film imposes local variation in structural orientation and consequently increases local strain heterogeneity in the perovskite lattice. The local strain is directly reflected in the chemical bonding in the core framework, which determines the local electronic band structure. The reliability of device performance is closely related to the uniform electronic band structure by minimizing local dependency. Therefore, the control of strain inhomogeneity is highly important for achieving reliability and reproducibility from the perspective of device performance. In addition, the lattice strain plays an important role in determining defect dynamics in the lattice, which is closely related to its formation and migration. The lattice stability is, therefore, inherent to the lattice strain because the atomic displacement under phase conversion can be significantly facilitated by involving defects. To this end, various approaches for enhancing crystallinity with a long-range structural orientation effectively reduce the local strain inhomogeneity in the perovskite film. Apart from the local strain and its heterogeneity, originating from a polycrystalline soft lattice, depth-dependent in-plane tensile strain is generally entailed in the solution-processed perovskite film and regarded as a more detrimental factor to device performance. The strain inhomogeneity along the out-of-plane direction is found to be resolved by regulating crystallization and/or interface management. Although the control of crystallization is aimed principally at avoiding the formation of the in-plane tensile strain, interface management usually pursues relaxation of the residual strain by employing an interlayer based on a flexible alkyl chain to effectively dissipate the strain at the interface. Effective strategies to relieve the in-plane tensile strain consequently exhibit improved device stability with enhanced performance owing to the synergistic effect on interfacial defect passivation and interfacial energy band alignment, which is favorable for charge collection.

Strain control strategies have mostly focused on the problematic residual tensile strain along the in-plane direction and have accordingly been devised to relieve residual strain to improve the long-term stability of PSCs. However, regulating the lattice strain can be one of the fascinating methods for delicately manipulating the electronic band structure and lattice stability. In this regard, the development of advanced technology to control the residual lattice strain is in high

7906 | Chem. Soc. Rev., 2025, **54**, 7870–7912

This journal is © The Royal Society of Chemistry 2025

demand to passively deal with the current issue and to actively derive the maximal benefits in optoelectronic properties and lattice stability, which would likely pave the way for opening new horizons by overcoming the persistent stability issue.

Conflicts of interest

The authors declare no conflict of interest.

Data availability

This is a review article and does not report any original data. All data discussed are from previously published sources, which are appropriately cited within the text.
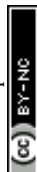
Acknowledgements

References

1 H.-S. Kim, C.-R. Lee, J.-H. Im, K.-B. Lee, T. Moehl, A. Marchioro, S.-J. Moon, R. Humphry-Baker, J.-H. Yum, J. E. Moser, M. Grätzel and N.-G. Park, *Sci. Rep.*, 2012, **2**, 591.

2 M. M. Lee, J. Teuscher, T. Miyasaka, T. N. Murakami and H. J. Snaith, *Science*, 2012, **338**, 643–647.

3 A. Machín and F. Márquez, *Materials*, 2024, **17**, 1165.

4 P. Chen, Y. Xiao, S. Li, X. Jia, D. Luo, W. Zhang, H. J. Snaith, Q. Gong and R. Zhu, *Chem. Rev.*, 2024, **124**, 10623–10700.

5 H. Zhang, X. Ji, H. Yao, Q. Fan, B. Yu and J. Li, *Sol. Energy*, 2022, **233**, 421–434.

6 National Renewable Energy Laboratory, *Champion Photo-voltaic Module Efficiency Chart*, **https://www.nrel.gov/pv/cell-efficiency**, (accessed January 2025).

7 National Renewable Energy Laboratory, *Best Research-Module Efficiency Chart*, **https://www2.nrel.gov/pv/module-efficiency**, (accessed December 2024).

8 H.-S. Kim and N.-G. Park, *Appl. Phys. Rev.*, 2025, **12**, 021313.

9 H.-J. Kim, H.-S. Kim and N.-G. Park, *Adv. Energy Sustainability Res.*, 2021, **2**, 2000051.

10 H.-S. Kim and N.-G. Park, *Adv. Energy Mater.*, 2025, **15**, 2400089.

11 E. M. Hutter, M. C. Gélvez-Rueda, A. Osherov, V. Bulović, F. C. Grozema, S. D. Stranks and T. J. Savenije, *Nat. Mater.*, 2017, **16**, 115–120.

12 K. Galkowski, A. Mitioglu, A. Miyata, P. Plochocka, O. Portugall, G. E. Eperon, J. T.-W. Wang, T. Stergiopoulos, S. D. Stranks, H. J. Snaith and R. J. Nicholas, *Energy Environ. Sci.*, 2016, **9**, 962–970.

13 S. D. Stranks, G. E. Eperon, G. Grancini, C. Menelaou, M. J. P. Alcocer, T. Leijtens, L. M. Herz, A. Petrozza and H. J. Snaith, *Science*, 2013, **342**, 341–344.

14 K. Handloser, N. Giesbrecht, T. Bein, P. Docampo, M. Handloser and A. Hartschuh, *ACS Photonics*, 2016, **3**, 255–261.

15 J. M. Ball, M. M. Lee, A. Hey and H. J. Snaith, *Energy Environ. Sci.*, 2013, **6**, 1739.

16 N.-Y. Jo, Y.-K. Hong, S. Yang and H.-S. Kim, *Bull. Korean Chem. Soc.*, 2024, **45**, 570–575.

17 J. Suo, B. Yang, E. Mosconi, D. Bogachuk, T. A. S. Doherty, K. Frohna, D. J. Kubicki, F. Fu, Y. Kim, O. Er-Raji, T. Zhang, L. Baldinelli, L. Wagner, A. N. Tiwari, F. Gao, A. Hinsch, S. D. Stranks, F. D. Angelis and A. Hagfeldt, *Nat. Energy*, 2024, **9**, 172–183.

18 Y. S. Shin, J. Lee, D. G. Lee, J. W. Song, J. Seo, J. Roe, M. J. Sung, S. Park, G. Y. Shin, J. Yeop, D. Lee, C. H. Yoon, M. Kim, J. G. Son, G.-H. Kim, S. Cho, J. Y. Kim, T. K. Lee and D. S. Kim, *Energy Environ. Sci.*, 2025, **18**, 3269–3277.

19 Z. Zheng, Z. Xue, K. Zhao, Y. Yang, X. Zhu, H. Li, S. Cheng, S. Li, N. Yan and Z. Wang, *Sol. RRL*, 2024, **8**, 2301076.

20 G. Tang, P. Ghosez and J. Hong, *J. Phys. Chem. Lett.*, 2021, **12**, 4227–4239.

21 H.-S. Kim and N.-G. Park, *NPG Asia Mater.*, 2020, **12**, 78.

22 H.-S. Kim and N.-G. Park, *Adv. Mater.*, 2023, **35**, 2204807.

23 B. Hou, C. Shang, C. Wang, D. Qu, J. Qiao, X. Zhang, W. Zhao, R. Han, S. Dong, Y. Xue, Y. Ke, F. Ye, X. Yang, Y. Tu and W. Huang, *Research*, 2024, **7**, 0309.

24 J. Li, L. Xie, Z. Pu, C. Liu, M. Yang, Y. Meng, B. Han, S. Bu, Y. Wang, X. Zhang, T. Wang and Z. Ge, *Adv. Funct. Mater.*, 2023, **33**, 2301956.

25 D.-J. Xue, Y. Hou, S.-C. Liu, M. Wei, B. Chen, Z. Huang, Z. Li, B. Sun, A. H. Proppe, Y. Dong, M. I. Saidaminov, S. O. Kelley, J.-S. Hu and E. H. Sargent, *Nat. Commun.*, 2020, **11**, 1514.

26 J. Zhao, Y. Deng, H. Wei, X. Zheng, Z. Yu, Y. Shao, J. E. Shield and J. Huang, *Sci. Adv.*, 2017, **3**, eaao5616.

27 C. Zhu, X. Niu, Y. Fu, N. Li, C. Hu, Y. Chen, X. He, G. Na, P. Liu, H. Zai, Y. Ge, Y. Lu, X. Ke, Y. Bai, S. Yang, P. Chen, Y. Li, M. Sui, L. Zhang, H. Zhou and Q. Chen, *Nat. Commun.*, 2019, **10**, 815.

28 Y. Chen, Y. Lei, Y. Li, Y. Yu, J. Cai, M.-H. Chiu, R. Rao, Y. Gu, C. Wang, W. Choi, H. Hu, C. Wang, Y. Li, J. Song, J. Zhang, B. Qi, M. Lin, Z. Zhang, A. E. Islam, B. Maruyama, S. Dayeh, L.-J. Li, K. Yang, Y.-H. Lo and S. Xu, *Nature*, 2020, **577**, 209–215.

29 S. Cheng, Y. Yang, X. Zhu, Y. Li, H. Li, W. Xiong, Z. Zheng, S. Li, Y. Liu, X. Liu, Q. Lin, S. Yuan, E. Shi and Z. Wang, *Energy Environ. Sci.*, 2025, **18**, 2452–2461.

30 A. Garrote-Márquez, L. Lodeiro, R. Suresh, N. C. Hernández, R. Grau-Crespo and E. Menéndez-Proupin, *J. Phys. Chem. C*, 2023, **127**, 15901.

31 X. Yue, C. Wang, B. Zhang, Z. Zhang, Z. Xiong, X. Zu, Z. Liu, Z. Hu, G. O. Odunmbaku, Y. Zheng, K. Sun and J. Du, *Nat. Commun.*, 2023, **14**, 917.

32 B. Jin, J. Cao, R. Yuan, B. Cai, C. Wu and X. Zheng, *Adv. Energy Sustainability Res.*, 2023, **4**, 2200143.

This journal is © The Royal Society of Chemistry 2025

Chem. Soc. Rev., 2025, **54**, 7870–7912 | **7907**

33 Y. Wang, L. Gao, Y. Yang, Y. Xiang, Z. Chen, Y. Dong, H. Zhou, Z. Cai and G.-C. Wang, *Phys. Rev. Mater.*, 2018, **2**, 076002.

34 M. I. Saidaminov, J. Kim, A. Jain, R. Quintero-Bermudez, H. Tan, G. Long, F. Tan, A. Johnston, Y. Zhao, O. Voznyy and E. H. Sargent, *Nat. Energy*, 2018, **3**, 648–654.

35 I. Borriello, G. Cantele and D. Ninno, *Phys. Rev. B:Condens. Matter Mater. Phys.*, 2008, **77**, 235214.

36 G. E. Eperon, S. D. Stranks, C. Menelaou, M. B. Johnston, L. M. Herz and H. J. Snaith, *Energy Environ. Sci.*, 2014, **7**, 982–988.

37 R. Prasanna, A. Gold-Parker, T. Leijtens, B. Conings, A. Babayigit, H.-G. Boyen, M. F. Toney and M. D. McGehee, *J. Am. Chem. Soc.*, 2017, **139**, 11117–11124.

38 W. Travis, E. N. K. Glover, H. Bronstein, D. O. Scanlon and R. G. Palgrave, *Chem. Sci.*, 2016, **7**, 4548–4556.

39 T.-Y. Wang, Y.-Y. Hao, M.-Z. Zhu, G.-R. Cao and Z.-M. Zhou, *Chin. J. Chem.*, 2024, **42**, 1284–1306.

40 M. Senno and S. Tinte, *Phys. Chem. Chem. Phys.*, 2021, **23**, 7376–7385.

41 O. J. Weber, D. Ghosh, S. Gaines, P. F. Henry, A. B. Walker, M. S. Islam and M. T. Weller, *Chem. Mater.*, 2018, **30**, 3768–3778.

42 M. Šimėnas, S. Balčiūnas, M. Mączka and J. Banys, *J. Mater. Chem.*, 2022, **10**, 5210–5217.

43 X.-G. Zhao, G. M. Dalpian, Z. Wang and A. Zunger, *Phys. Rev. B*, 2020, **101**, 155137.

44 G. Laurita, D. H. Fabini, C. C. Stoumpos, M. G. Kanatzidis and R. Seshadri, *Chem. Sci.*, 2017, **8**, 5628.

45 A. M. A. Leguy, A. R. Goñi, J. M. Frost, J. Skelton, F. Brivio, X. Rodríguez-Martínez, O. J. Weber, A. Pallipurath, M. Isabel Alonso, M. Campoy-Quiles, M. T. Weller, J. Nelson, A. Walsh and P. R. F. Barnes, *Phys. Chem. Chem. Phys.*, 2016, **18**, 27051–27066.

46 M. A. Carignano, Y. Saeed, S. A. Aravindh, I. S. Roqan, J. Even and C. Katan, *Phys. Chem. Chem. Phys.*, 2016, **18**, 27109–27118.

47 C. Quarti, E. Mosconi, J. M. Ball, V. D'Innocenzo, C. Tao, S. Pathak, H. J. Snaith, A. Petrozza and F. D. Angelis, *Energy Environ. Sci.*, 2016, **9**, 155.

48 J.-S. Park, S. Choi, Y. Yan, Y. Yang, J. M. Luther, S.-H. Wei, P. Parilla and K. Zhu, *J. Phys. Chem. Lett.*, 2015, **6**, 4304.

49 J. S. Bechtel, R. Seshadri and A. V. D. Ven, *J. Phys. Chem. C*, 2016, **120**, 12403.

50 D. Zhang, Y. Zhu, L. Liu, X. Ying, C.-E. Hsiung, R. Sougrat, K. Li and Y. Han, *Science*, 2018, **359**, 675–679.

51 D. H. Fabini, C. C. Stoumpos, G. Laurita, A. Kaltzoglou, A. G. Kontos, P. Falaras, M. G. Kanatzidis and R. Seshadri, *Angew. Chem., Int. Ed.*, 2016, **55**, 15392–15396.

52 T. Chen, B. J. Foley, C. Park, C. M. Brown, L. W. Harriger, J. Lee, J. Ruff, M. Yoon, J. J. Choi and S.-H. Lee, *Sci. Adv.*, 2016, **2**, e1601650.

53 B. Charles, J. Dillon, O. J. Weber, M. S. Islam and M. T. Weller, *J. Mater. Chem. A*, 2017, **5**, 22495–22499.

54 M. Kim, G.-H. Kim, T. K. Lee, I. W. Choi, H. W. Choi, Y. Jo1, Y. J. Yoon, J. W. Kim, J. Lee, D. Huh, H. Lee, S. K. Kwak, J. Y. Kim and D. S. Kim, *Joule*, 2019, **3**, 2179–2192.

55 F. Ye, J. Ma, C. Chen, H. Wang, Y. Xu, S. Zhang, T. Wang, C. Tao and G. Fang, *Adv. Mater.*, 2021, **33**, 2007126.

56 J. S. Bechtel and A. V. D. Ven, *Phys. Rev. Mater.*, 2018, **2**, 025401.

57 R. J. Tilley, *Perovskites: structure-property relationships*, John Wiley & Sons, United Kingdom, 2016.

58 X. Zheng, C. Wu, S. K. Jha, Z. Li, K. Zhu and S. Priya, *ACS Energy Lett.*, 2016, **1**, 1014–1020.

59 G. Kim, H. Min, K. S. Lee, D. Y. Lee, S. M. Yoon and S. I. Seok, *Science*, 2020, **370**, 108–112.

60 S. Jariwala, H. Sun, G. W. P. Adhyaksa, A. Lof, L. A. Muscarella, B. Ehrler, E. C. Garnett and D. S. Ginger, *Joule*, 2019, **3**, 3048–3060.

61 Z. Liang, J. Cao, Z. Zhou, L. Ren, H. Wu, Z. Wang, C. Yi, D. Yang, K. Wang and C. Wu, *Nat. Synth.*, 2025, 1–12.

62 T. W. Jones, A. Osherov, M. Alsari, M. Sponseller, B. C. Duck, Y.-K. Jung, C. Settens, F. Niroui, R. Brenes, C. V. Stan, Y. Li, M. Abdi-Jalebi, N. Tamura, J. E. Macdonald, M. Burghammer, R. H. Friend, V. Bulović, A. Walsh, G. J. Wilson, S. Lilliu and S. D. Stranks, *Energy Environ. Sci.*, 2019, **12**, 596–606.

63 M. U. Rothmann, W. Li, J. Etheridge and Y.-B. Cheng, *Adv. Energy Mater.*, 2017, **7**, 1700912.

64 G. W. P. Adhyaksa, S. Brittman, H. Āboliņš, A. Lof, X. Li, J. D. Keelor, Y. Luo, T. Duevski, R. M. A. Heeren, S. R. Ellis, D. P. Fenning and E. C. Garnett, *Adv. Mater.*, 2018, **30**, 1804792.

65 Z. Guo, J. S. Manser, Y. Wan, P. V. Kamat and L. Huang, *Nat. Commun.*, 2015, **6**, 7471.

66 A. M. Stoneham, *Rep. Prog. Phys.*, 1981, **44**, 1251–1295.

67 W. Li, S. K. Yadavalli, D. Lizarazo-Ferro, M. Chen, Y. Zhou, N. P. Padture and R. Zia, *ACS Energy Lett.*, 2018, **3**, 2669–2670.

68 S. Li, Y. Xiao, R. Su, W. Xu, D. Luo, P. Huang, L. Dai, P. Chen, P. Caprioglio, K. A. Elmestekawy, M. Dubajic, C. Chosy, J. Hu, I. Habib, A. Dasgupta, D. Guo, Y. Boeije, S. J. Zelewski, Z. Lu, T. Huang, Q. Li, J. Wang, H. Yan, H.-H. Chen, C. Li, B. A. I. Lewis, D. Wang, J. Wu, L. Zhao, B. Han, J. Wang, L. M. Herz, J. R. Durrant, K. S. Novoselov, Z.-H. Lu, Q. Gong, S. D. Stranks, H. J. Snaith and R. Zhu, *Nature*, 2024, **635**, 874–881.

69 S. Jariwala, H. Sun, G. W. P. Adhyaksa, A. Lof, L. A. Muscarella, B. Ehrler, E. C. Garnett and D. S. Ginger, *Joule*, 2019, **3**, 3048–3060.

70 M.-J. Choi, J.-W. Lee and H. W. Jang, *Adv. Mater.*, 2024, **36**, 2308827.

71 J. Zhou, S. Fu, S. Zhou, L. Huang, C. Wang, H. Guan, D. Pu, H. Cui, C. Wang, T. Wang, W. Meng, G. Fang and W. Ke, *Nat. Commun.*, 2024, **15**, 2324.

72 Z. Qin, M. Chen, Z. Zhang, Y. Wang and L. Han, *Energy Environ. Sci.*, 2025, **18**, 2264–2272.

73 M. Hao, J. Yang, W. Yu, B. J. Lawrie, P. Guo, X. Zhang, T. Duan, T. Xiao, L. Chen, Y. Xiang, P. Guo, M. Ahmadi and Y. Zhou, *Nat. Nanotechnol.*, 2025, **20**, 630–638.

74 Z. Liang, Y. Zhang, H. Xu, W. Chen, B. Liu, J. Zhang, H. Zhang, Z. Wang, D.-H. Kang, J. Zeng, X. Gao, Q. Wang,

7908 | *Chem. Soc. Rev.*, 2025, **54**, 7870–7912

This journal is © The Royal Society of Chemistry 2025

H. Hu, H. Zhou, X. Cai, X. Tian, P. Reiss, B. Xu, T. Kirchartz, Z. Xiao, S. Dai, N.-G. Park, J. Ye and X. Pan, *Nature*, 2023, **62**, 557–563.

75 T. Huang, F. Xu, J. Hu, J. Wu, S. Li, P. Chen, X. Jia, Q. Li, H. Yan, Y. Ji, D. Luo, D. Wang, J. Hu, H.-H. Chen, Z. Lu, H. Xu, L. Li, R. Sha, Q. Zhong, X. Bai, M. I. Dar, T. Song, Z. Li, X. Yang, L. Zhao, Z.-H. Lu, Q. Gong and R. Zhu, *Energy Environ. Sci.*, 2024, **17**, 5984–5992.

76 L. Zheng, M. Wei, F. T. Eickemeyer, J. Gao, B. Huang, U. Gunes, P. Schouwink, D. W. Bi, V. Carnavali, M. Mensi, F. Biasoni, Y. Zhang, L. Agosta, V. Slama, N. Lempesis, M. A. Hope, S. M. Zakeeruddin, L. Emsley, U. Rothlisberger, L. Pfeifer, Y. Xuan and M. Grätzel, *Science*, 2025, **388**, 88–95.

77 J. Xu, C. C. Boyd, Z. J. Yu, A. F. Palmstrom, D. J. Witter, B. W. Larson, R. M. France, J. Werner, S. P. Harvey, E. J. Wolf, W. Weigand, S. Manzoor, M. F. A. M. van Hest, J. J. Berry, J. M. Luther, Z. C. Holman and M. D. McGehee, *Science*, 2020, **367**, 1097–1104.

78 P. Wang, Y. Wu, B. Cai, Q. Ma, X. Zheng and W.-H. Zhang, *Adv. Funct. Mater.*, 2019, **29**, 1807661.

79 D. Liu, D. Luo, A. N. Iqbal, K. W. P. Orr, T. A. S. Doherty, Z.-H. Lu, S. D. Stranks and W. Zhang, *Nat. Mater.*, 2021, **20**, 1337–1346.

80 M. Keshavarz, M. Ottesen, S. Wiedmann, M. Wharmby, R. Küchler, H. Yuan, E. Debroye, J. A. Steele, J. Martens, N. E. Hussey, M. Bremholm, M. B. J. Roeffaers and J. Hofkens, *Adv. Mater.*, 2019, **31**, 1900521.

81 T. J. Jacobsson, L. J. Schwan, M. Ottosson, A. Hagfeldt and T. Edvinsson, *Inorg. Chem.*, 2015, **54**, 10678–10685.

82 H. Tsai, R. Asadpour, J.-C. Blancon, C. C. Stoumpos, O. Durand, J. W. Strzalka, B. Chen, R. Verduzco, P. M. Ajayan, S. Tretiak, J. Even, M. A. Alam, M. G. Kanatzidis, W. Nie and A. D. Mohite, *Science*, 2018, **360**, 67–70.

83 H. Zhang and N.-G. Park, *J. Phys. Energy*, 2023, **5**, 024002.

84 W. Mao, C. R. Hall, S. Bernardi, Y.-B. Cheng, A. Widmer-Cooper, T. A. Smith and U. Bach, *Nat. Mater.*, 2021, **20**, 55.

85 Q. Li, Y. Zheng, H. Wang, X. Liu, M. Lin, X. Sui, X. Leng, D. Liu, Z. Wei, M. Song, D. Li, H. G. Yang, S. Yang and Y. Hou, *Science*, 2025, **387**, 1069–1077.

86 N. Rolston, R. Bennett-Kennett, L. T. Schelhas, J. M. Luther, J. A. Christians, J. J. Berry and R. H. Dauskardt, *Science*, 2020, **368**, eaay8691.

87 W. Meng, K. Zhang, A. Osvet, J. Zhang, W. Gruber, K. Forberich, B. Meyer, W. Heiss, T. Unruh, N. Li and C. J. Brabec, *Joule*, 2022, **6**, 458–475.

88 Y. Shen, T. Zhang, G. Xu, J. A. Steele, X. Chen, W. Chen, G. Zheng, J. Li, B. Guo, H. Yang, Y. Wu, X. Lin, T. Alshahrani, W. Yin, J. Zhu, F. Wang, A. Amassian, X. Gao, X. Zhang, F. Gao, Y. Li and Y. Li, *Nature*, 2024, **635**, 882–889.

89 Q. Wang, B. Chen, Y. Liu, Y. Deng, Y. Bai, Q. Dong and J. Huang, *Energy Environ. Sci.*, 2017, **10**, 516–522.

90 J. S. Yun, J. Kim, T. Young, R. J. Patterson, D. Kim, J. Seidel, S. Lim, M. A. Green, S. Huang and A. Ho-Baillie, *Adv. Funct. Mater.*, 2018, **28**, 1705363.

91 S. Shin, S.-H. Yang, S. Seo, H. Park, U. Amornkitbamrung, Y. In, C. Wang, T. Nakamura, A. Wakamiya, Y.-M. Kim, Y.-M. Kim, Y.-M. Kim and H. Shin, *ACS Energy Lett.*, 2024, **9**, 3618–3627.

92 C. Gammer, J. Kacher, C. Czarnik, O. L. Warren, J. Ciston and A. M. Minor, *Appl. Phys. Lett.*, 2016, **109**, 081906.

93 D. Ivanov, S. Ivanov, S. Lomov and I. Verpoest, *Opt. Lasers Eng.*, 2009, **47**, 360–370.

94 J. Wu, S.-C. Liu, Z. Li, S. Wang, D.-J. Xue, Y. Lin and J.-S. Hu, *Natl. Sci. Rev.*, 2021, **8**, nwab047.

95 C. Xing, Q. Bao, S. Liu, X. Chu, F. Lu, L. Zhang, L. Yu, T. Zhang and D. Wang, *Sol. RRL*, 2023, **7**, 2300434.

96 G. Yuan, W. Xie, Q. Song, S. Ma, Y. Ma, C. Shi, M. Xiao, F. Pei, X. Niu, Y. Zhang, J. Dou, C. Zhu, Y. Bai, Y. Wu, H. Wang, Q. Fan and Q. Chen, *Adv. Mater.*, 2023, **35**, 2211257.

97 R. Wang, X. Li, J. Qi, C. Su, J. Yang, S. Yang, M. Yuan and T. He, *Adv. Mater.*, 2023, **35**, 2304149.

98 L. Ning, L. Song, Z. Yao, W.-H. Chen, P. Du, P.-C. Jiang and J. Xiong, *Adv. Energy Mater.*, 2024, **14**, 2401320.

99 M. Dimitrievska, A. Fairbrother, R. Gunder, G. Gurieva, H. Xie, E. Saucedo, A. Pérez-Rodríguez, V. Izquierdo-Roca and S. Schorr, *Phys. Chem. Chem. Phys.*, 2016, **18**, 8692–8700.

100 C. Luo, G. Zheng, F. Gao, X. Wang, C. Zhan, X. Gao and Q. Zhao, *Nat. Photonics*, 2023, **17**, 856–864.

101 J. Epp, *X-ray diffraction (XRD) techniques for materials characterization*, Woodhead Publishing, 2016, pp. 81–124.

102 D.-A. Park, C. Zhang and N.-G. Park, *ACS Energy Lett.*, 2024, **9**, 2428–2435.

103 M. J. Berger, J. H. Hubbell, S. M. Seltzer, J. Chang, J. S. Coursey, R. Sukumar, D. S. Zucker and K. Olsen, *XCOM: photon cross sections database*, **https://www.nist.gov/pml/data/xcom/index.cfm**, 1998.

104 A. K. Zak, W. H. A. Majid, M. E. Abrishami and R. Yousefi, *Solid State Sci.*, 2011, **13**, 251–256.

105 J. Liu, R. E. Saw and Y.-H. Kiang, *J. Pharm. Sci.*, 2010, **99**, 3807–3814.

106 U. Welzel, J. Ligot, P. Lamparter, A. C. Vermeulenb and E. J. Mittemeijer, *J. Appl. Crystallogr.*, 2005, **38**, 1–29.

107 C.-H. Ma, J.-H. Huang and H. Chen, *Thin Solid Films*, 2002, **418**, 73–78.

108 T. Yang, Y. Yang, T. Niu, E. Zhao, N. Wu, S. Wang, X. Chen, S. Wang, Y. Wang, Y. Wu, Z. Zhang, C. Ma, Y. Gong, D. Liu and K. Zhao, *ACS Energy Lett.*, 2024, **10**, 427–438.

109 C. Zhang, S. Wu, L. Tao, G. M. Arumugam, C. Liu, Z. Wang, S. Zhu, Y. Yang, J. Lin, X. Liu, R. E. I. Schropp and Y. Mai, *Adv. Energy Mater.*, 2020, **10**, 2002004.

110 X. Xu, Q. Du, H. Kang, X. Gu, C. Shan, J. Zeng, T. Dai, Q. Yang, X. Sun, G. Li, E. Zhou, G. Luo, B. Xu and A. K. K. Kyaw, *Adv. Funct. Mater.*, 2024, **34**, 2408512.

111 X. Wang and A. V. Riessen, *Powder Diffr.*, 2017, **32**, S9–S15.

112 H. Xu, Y. Xiao, K. A. Elmestekawy, P. O. Caprioglio, Q. Li, Q. Zhong, Y. Ji, T. Huang, H. Yan, Y. Yang, L. M. Herz, Q. Gong, H. J. Snaith, R. Zhu and L. Zhao, *Energy Environ. Sci.*, 2025, **18**, 246–255.

113 P. Bindu and S. Thomas, *J. Theor. Appl. Phys.*, 2014, **8**, 123–134.

114 S. A. Hassanzadeh-Tabrizi, *J. Alloys Compd.*, 2023, **968**, 171914.

This journal is © The Royal Society of Chemistry 2025

Chem. Soc. Rev., 2025, **54**, 7870–7912 | 7909

115 G. Srinet, S. Sharma, M. Kumar and A. Anshul, *Phys. E*, 2021, **125**, 114381.

116 H. Bantikatla, L. D. N.S.M.P. and R. K. Bhogoju, *Mater. Today: Proc.*, 2021, **47**, 4891–4896.

117 A. M. Sami and K. H. Harbbi, *AIP Conf. Proc.*, 2022, **2394**, 090018.

118 F. T. L. Muniz, M. A. R. Miranda, C. Morilla dos Santos and J. M. Sasake, *Acta Crystallogr.*, 2016, **72**, 385–390.

119 A. S. Abdel-Rahman and Y. A. Sabry, *Int. J. Non-Linear Mech.*, 2024, **161**, 104670.

120 X. Wang, H. Huang, M. Wang, Z. Lan, P. Cui, S. Du, Y. Yang, L. Yan, Q. Zhang, S. Qu and M. Li, *Adv. Mater.*, 2024, **36**, 2310710.

121 P. Yang, J. Wu, W. Lin, X. Jiang, Y. Wang, W. Sun, Z. Lan and J. Lin, *Chem. Eng.*, 2024, **488**, 151128.

122 Y. Meng, Y. Wang, C. Liu, P. Yan, K. Sun, Y. Wang, R. Tian, R. Cao, J. Zhu, H. Do, J. Lu and Z. Ge, *Adv. Mater.*, 2024, **36**, 2309208.

123 Q. Zhou, J. Duan, X. Yang, Y. Duan and Q. Tang, *Angew. Chem., Int. Ed.*, 2020, **132**, 22181–22185.

124 J. Kim, J.-S. Park, G. Y. Kim and W. Jo, *Adv. Energy Mater.*, 2024, **14**, 2402117.

125 Y. Zhou, A. L. Vasiliev, W. Wu, M. Yang, S. Pang, K. Zhu and N. P. Padture, *J. Phys. Chem. Lett.*, 2015, **6**, 2292–2297.

126 M. U. Rothmann, W. Li, Y. Zhu, A. Liu, Z. Ku, U. Bach, J. Etheridge and Y.-B. Cheng, *Adv. Mater.*, 2018, **30**, 1800629.

127 N. D. Bassim, B. T. DE Gregorio, A. L. D. Kilcoyne, K. Scott, T. Chou, S. Wirick, G. Cody and R. M. Stroud, *J. Microsc.*, 2012, **245**, 288–301.

128 L. Hao and S. Cai, *Microstructures*, 2025, **5**, 2025012.

129 Y. Miao, Y. Zhao, S. Zhang, R. Shi and T. Zhang, *Adv. Mater.*, 2022, **34**, 2200868.

130 J. Jeong, M. Kim, J. Seo, H. Lu, P. Ahlawat, A. Mishra, Y. Yang, M. A. Hope, F. T. Eickemeyer, M. Kim, Y. Jin Yoon, I. W. Choi, B. P. Darwich, S. J. Choi, Y. Jo, J. H. Lee, B. Walker, S. M. Zakeeruddin, L. Emsley, U. Rothlisberger, A. Hagfeldt, D. S. Kim, M. Grätzel and J. Y. Kim, *Nature*, 2021, **592**, 381–385.

131 Q. Tai, P. You, H. Sang, Z. Liu, C. Hu, H. L. W. Chan and F. Yan, *Nat. Commun.*, 2016, **7**, 11105.

132 C. Liang, H. Gu, Y. Xia, Z. Wang, X. Liu, J. Xia, S. Zuo, Y. Hu, X. Gao, W. Hui, L. Chao, T. Niu, M. Fang, H. Lu, H. Dong, H. Yu, S. Chen, X. Ran, L. Song, B. Li, J. Zhang, Y. Peng, G. Shao, J. Wang, Y. Chen, G. Xing and W. Huang, *Nat. Energy*, 2021, **6**, 38–45.

133 J. Park, J. Kim, H.-S. Yun, M. J. Paik, E. Noh, H. J. Mun, M. G. Kim, T. J. Shin and S. I. Seok, *Nature*, 2023, **616**, 724–730.

134 A. Hassan, Z. Wang, Y. H. Ahn, M. Azam, A. A. Khan, U. Farooq, M. Zubair and Y. Cao, *Nano Energy*, 2022, **101**, 107579.

135 X. Yuan, R. Li, Z. Xiong, P. Li, G. O. Odunmbaku, K. Sun, Y. Deng and S. Chen, *Adv. Funct. Mater.*, 2023, **33**, 2215096.

136 N. Li, Y. Luo, Z. Chen, X. Niu, X. Zhang, J. Lu, R. Kumar, J. Jiang, H. Liu, X. Guo, B. Lai, G. Brocks, Q. Chen, S. Tao, D. P. Fenning and H. Zhou, *Joule*, 2020, **4**, 1743–1758.

137 Y. Bai, Z. Huang, X. Zhang, J. Lu, X. Niu, Z. He, C. Zhu, M. Xiao, Q. Song, X. Wei, C. Wang, Z. Cui, J. Dou, Y. Chen, F. Pei, H. Zai, W. Wang, T. Song, P. An, J. Zhang, J. Dong, Y. Li, J. Shi, H. Jin, P. Chen, Y. Sun, Y. Li, H. Chen, Z. Wei, H. Zhou and Q. Chen, *Science*, 2022, **378**, 747–754.

138 Y. Zheng, X. Wu, J. Liang, Z. Zhang, J. Jiang, J. Wang, Y. Huang, C. Tian, L. Wang, Z. Chen and C.-C. Chen, *Adv. Funct. Mater.*, 2022, **32**, 2200431.

139 H. Min, S.-G. Ji and S. I. Seok, *Joule*, 2022, **6**, 2175–2185.

140 S. Cai, J. Gao, Y. Wu, Y. Zou, J. Liang, Y. Li, X. He, Q. Cai, M. Wang, X. Huang, X. Wang, S. Sajid, D. Wei, R. Zhang, D. Song and Y. Wang, *Adv. Funct. Mater.*, 2024, **34**, 2411014.

141 H. Zhang, Z. Wang, H. Wang, X. Yao, F. Wang, S. Wang, S. Bai, J. Huang, X. Luo, S. Wu and X. Liu, *J. Mater. Chem. A*, 2023, **11**, 15301–15310.

142 H. Zhang, Z. Chen, M. Qin, Z. Ren, K. Liu, J. Huang, D. Shen, Z. Wu, Y. Zhang, J. Hao, C.-S. Lee, X. Lu, Z. Zheng, W. Yu and G. Li, *Adv. Mater.*, 2021, **33**, 2008487.

143 X. Li, W. Zhang, Y.-C. Wang, W. Zhang, H.-Q. Wang and J. Fang, *Nat. Commun.*, 2018, **9**, 3806.

144 X. Li, S. Fu, S. Liu, Y. Wu, W. Zhang, W. Song and J. Fang, *Nano Energy*, 2019, **64**, 103962.

145 H. Guo, G. W. Yoon, Z. J. Li, Y. Yun, S. Lee, Y.-H. Seo, N. J. Jeon, G. S. Han and H. S. Jung, *Adv. Energy Mater.*, 2024, **14**, 2302743.

146 F. Qiu, J. Sun and J. Qi, *Chem. Eng. J.*, 2022, **430**, 132869.

147 J. Zhang, Z. Li, F. Guo, H. Jiang, W. Yan, C. Peng, R. Liu, L. Wang, H. Gao, S. Pang and Z. Zhou, *Angew. Chem., Int. Ed.*, 2023, **62**, e202305221.

148 J. Zhang, X. Niu, C. Peng, H. Jiang, L. Yu, H. Zhou and Z. Zhou, *Angew. Chem., Int. Ed.*, 2023, **62**, e202314106.

149 G. Tang, P. You, Q. Tai, A. Yang, J. Cao, F. Zheng, Z. Zhou, J. Zhao, P. K. L. Chan and F. Yan, *Adv. Mater.*, 2019, **31**, 1807689.

150 M. B. Faheem, B. Khan, C. Feng, M. W. S. Subhani, S. Mabrouk, M. H. Sayyad, A. Yildiz, W.-H. Zhang and Q. Qiao, *Adv. Mater. Interfaces*, 2022, **9**, 2200421.

151 Q. Gao, J. Qi, K. Chen, M. Xia, Y. Hu, A. Mei and H. Han, *Adv. Mater.*, 2022, **34**, 2200720.

152 K. Wang, Z. Xu, Z. Guo, H. Wang, S. M. H. Qaid, K. Yang and Z. Zang, *Adv. Energy Mater.*, 2024, **14**, 2402249.

153 B. Zhang, Y. Tian, J. X. Zhang and W. Cai, *Appl. Phys. Lett.*, 2011, **98**, 021906.

154 F. Zeng, L. Xu, C. Hu, J. Xing, Y. Wu, X. Bai, B. Dong and H. Song, *Adv. Funct. Mater.*, 2025, **35**, 2415547.

155 B. Liu, Q. Zhou, Y. Li, Y. Chen, D. He, D. Ma, X. Han, R. Li, K. Yang, Y. Yang, S. Lu, X. Ren, Z. Zhang, L. Ding, J. Feng, J. Yi and J. Chen, *Angew. Chem., Int. Ed.*, 2024, **63**, e202317185.

156 Q. Zhou, B. Liu, Y. Chen, D. Ma, X. Han, D. He, Z. Zhang, H. Yang, L. Ding, J. Feng, J. Yi, C. Chen and J. Chen, *Adv. Funct. Mater.*, 2024, **34**, 2315064.

157 H. Yang, Z. Xu, H. Wang, S. M. H. Qaid, O. F. Mohammed and Z. Zang, *Adv. Mater.*, 2024, **36**, 2411721.

158 Z. Long, C. Peng, K. Dong, H. Jiang, M. Zhu, W. Yan, Y. Dong, W. Jiang, L. Wen, X. Jiang and Z. Zhou, *Adv. Funct. Mater.*, 2024, **34**, 2408818.

7910 | *Chem. Soc. Rev.*, 2025, **54**, 7870–7912

This journal is © The Royal Society of Chemistry 2025

159 Q. Zhou, D. He, Q. Zhuang, B. Liu, R. Li, H. Li, Z. Zhang, H. Yang, P. Zhao, Y. He, Z. Zang and J. Chen, *Adv. Funct. Mater.*, 2022, **32**, 2205507.

160 J. Wang, S. Liu, X. Guan, K. Wang, S. Shen, C. Cong, C.-C. Chen and F. Xie, *ACS Appl. Mater. Interfaces*, 2024, **16**, 35732–35739.

161 L. Xie, J. Chen, P. Vashishtha, X. Zhao, G. S. Shin, S. G. Mhaisalkar and N.-G. Park, *ACS Energy Lett.*, 2019, **4**, 2192–2200.

162 L. Zhu, X. Zhang, M. Li, X. Shang, K. Lei, B. Zhang, C. Chen, S. Zheng, H. Song and J. Chen, *Adv. Energy Mater.*, 2021, **11**, 2100529.

163 Z. Wu, M. Jiang, Z. Liu, A. Jamshaid, L. K. Ono and Y. Qi, *Adv. Energy Mater.*, 2020, **10**, 1903696.

164 T. Li, S. Wang, J. Yang, X. Pu, B. Gao, Z. He, Q. Cao, J. Han and X. Li, *Nano Energy*, 2021, **82**, 105742.

165 H. Bi, H. Liu, D. He, L. Bai, W. Wang, Z. Zang and J. Chen, *Chem. Eng. J.*, 2021, **418**, 129375.

166 L. Wang, C. Wang, J. Li, C. Geng, Y. Mo, H. Li, T. Bu, J. Tong, Y.-B. Cheng and F. Huang, *Sol. RRL*, 2023, **7**, 2300144.

167 Q. Song, H. Gong, F. Sun, M. Li, T. Zhu, C. Zhang, F. You, Z. He, D. Li and C. Liang, *Small*, 2023, **19**, 2208260.

168 D. Music and L. Elalfy, *J. Phys. Condens. Matter*, 2019, **31**, 125101.

169 W. Lv, Z. Hu, W. Qiu, D. Yan, M. Li, A. Mei, L. Xu and R. Chen, *Adv. Sci.*, 2022, **9**, 2202028.

170 J. Fang, Z. Ding, X. Chang, J. Lu, T. Yang, J. Wen, Y. Fan, Y. Zhang, T. Luo, Y. Chen, S. (Frank) Liu and K. Zhao, *J. Mater. Chem. A*, 2021, **9**, 13297–13305.

171 J. Suo, B. Yang, D. Bogachuk, G. Boschloo and A. Hagfeldt, *Adv. Energy Mater.*, 2025, **15**, 2400205.

172 M. Azam, T. Du, Z. Wan, H. Zhao, H. Zeng, R. Wei, C. J. Brabec, J. Luo and C. Jia, *Energy Environ. Sci.*, 2024, **17**, 6974–7016.

173 H. Zhou, W. Wang, Y. Duan, R. Sun, Y. Li, Z. Xie, D. Xu, M. Wu, Y. Wang, H. Li, Q. Fan, Y. Peng, Y. Yao, C. Liao, Q. Peng, S. Liu and Z. Liu, *Angew. Chem., Int. Ed.*, 2024, **63**, e202403068.

174 N. Rolston, K. A. Bush, A. D. Printz, A. Gold-Parker, Y. Ding, M. F. Toney, M. D. McGehee and R. H. Dauskardt, *Adv. Energy Mater.*, 2018, **8**, 1802139.

175 S. Fu, N. Sun, H. Chen, Y. Li, Y. Li, X. Zhu, B. Feng, X. Guo, C. Yao, W. Zhang, X. Li and J. Fang, *Energy Environ. Sci.*, 2025, **18**, 3305–3312.

176 Y. Zhang, R. Yu, M. Li, Z. He, Y. Dong, Z. Xu, R. Wang, Z. Ma and Z. Tan, *Adv. Mater.*, 2024, **36**, 2310203.

177 C. Zhang, C. Liang, F. Sun, T. Zhu, X. Huang, Y. Guo, X. Guo, K. Ge, D. Li, F. You and Z. He, *Sci. China:Chem.*, 2025, **68**, 163–173.

178 M. Mori, T. Yamamoto, H. Itoh, H. Inaba and H. Tagawa, *J. Electrochem. Soc.*, 1998, **145**, 1374.

179 E. C. Schueller, G. Laurita, D. H. Fabini, C. C. Stoumpos, M. G. Kanatzidis and R. Seshadri, *Inorg. Chem.*, 2018, **57**, 695–701.

180 Z. Xiong, L. Lan, Y. Wang, C. Lu, S. Qin, S. Chen, L. Zhou, C. Zhu, S. Li, L. Meng, K. Sun and Y. Li, *ACS Energy Lett.*, 2021, **6**, 3824–3830.

181 M. Kim, J. Jeong, H. Lu, T. K. Lee, F. T. Eickemeyer, Y. Liu, I. W. Choi, S. J. Choi, Y. Jo, H.-B. Kim, S.-I. Mo, Y.-K. Kim, H. Lee, N. G. An, S. Cho, W. R. Tress, S. M. Zakeeruddin, A. Hagfeldt, J. Y. Kim, M. Grätzel and D. S. Kim, *Science*, 2022, **375**, 302–306.

182 B. Wang, J. Ma, Z. Li, G. Chen, Q. Gu, S. Chen, Y. Zhang, Y. Song, J. Chen, X. Pi, X. Yu and D. Yang, *Nano Res.*, 2022, **15**, 1069–1078.

183 Y. Zhao, L. Gao, Q. Wang, Q. Zhang, X. Yang, J. Zhu, H. Huang, J. Duan and Q. Tang, *Carbon Energy*, 2024, **6**, e468.

184 P. Fenter, F. Schreiber, V. Bulović and S. R. Forrest, *Chem. Phys. Lett.*, 1997, **277**, 521–526.

185 S.-Y. Ju, W. I. Lee and H.-S. Kim, *ACS Appl. Mater. Interfaces*, 2022, **14**, 39996–40004.

186 S. Yin, X. Luo, F. Tang, Z. Xiong, Y. Lin, W. Yang, Y. Shu, Y. Wang and L. Ying, *Energy Environ. Sci.*, 2025, **18**, 4153–4161.

187 Y. Huang, T. Liu, D. Li, Q. Lian, Y. Wang, G. Wang, G. Mi, Y. Zhou, A. Amini, B. Xu, Z. Tang, C. Cheng and G. Xing, *Small*, 2022, **18**, 2201694.

188 Y. Ma, J. Ge, A. K.-Y. Jen, J. You and S. F. Liu, *Adv. Opt. Mater.*, 2024, **12**, 2301623.

189 G. Kapil, T. Bessho, C. H. Ng, K. Hamada, M. Pandey, M. A. Kamarudin, D. Hirotani, T. Kinoshita, T. Minemoto, Q. Shen, T. Toyoda, T. N. Murakami, H. I. Segawa and S. Hayase, *ACS Energy Lett.*, 2019, **4**, 1991–1998.

190 J. Zhuang, P. Mao, Y. Luan, N. Chen, X. Cao, G. Niu, F. Jia, F. Wang, S. Cao and J. Wang, *Adv. Funct. Mater.*, 2021, **31**, 2010385.

191 X. Zhang, D. Zhang, Y. Zhou, Y. Du, J. Jin, Z. Zhu, Z. Wang, X. Cui, J. Li, S. Wu, J. Zhang and Q. Tai, *Adv. Funct. Mater.*, 2022, **32**, 2205478.

192 M. Saliba, T. Matsui, K. Domanski, J.-Y. Seo, A. Ummadisingu, S. M. Zakeeruddin, J.-P. Correa-Baena, W. R. Tress, A. Abate, A. Hagfeldt and M. Grätzel, *Science*, 2016, **354**, 206–209.

193 J.-W. Lee, D.-H. Kim, H.-S. Kim, S.-W. Seo, S. M. Cho and N.-G. Park, *Adv. Energy Mater.*, 2015, **5**, 1501310.

194 L. Zhou, M. Sui, J. Zhang, K. Cao, H. Wang, H. Yuan, Z. Lin, J. Zhang, P. Li, Y. Hao and J. Chang, *Chem. Eng. J.*, 2024, **496**, 154043.

195 Q. Xiao, Y. Zhao, Z. Huang, Y. Liu, P. Chen, S. Wang, S. Zhang, Y. Zhang and Y. Song, *Adv. Funct. Mater.*, 2024, **34**, 2314472.

196 Z. Zhu, C. Zhu, L. Yang, Q. Chen, L. Zhang, J. Dai, J. Cao, S. Zeng, Z. Wang, Z. Wang, W. Zhang, J. Bao, L. Yang, Y. Yang, B. Chen, C. Yin, H. Chen, Y. Cao, H. Gu, J. Yan, N. Wang, G. Xing, H. Li, X. Wang, S. Li, Z. Liu, H. Zhang, L. Wang, X. Huang and W. Huang, *Nat. Mater.*, 2022, **21**, 1042–1049.

197 C. Zhu, X. Wang, H. Li, C. Wang, Z. Gao, P. Zhang, X. Niu, N. Li, Z. Xu, Z. Su, Y. Chen, H. Zai, H. Xie, Y. Zhao, N. Yang, G. Liu, X. Wang, H. Zhou, J. Hong, X. Gao, Y. Bai and Q. Chen, *Interdiscip. Mater.*, 2023, **2**, 348–359.

198 H. Wang, W. Zhang, B. Wang, Z. Yan, C. Chen, Y. Hua, T. Wu, L. Wang, H. Xu and M. Cheng, *Nano Energy*, 2023, **111**, 108363.

This journal is © The Royal Society of Chemistry 2025

Chem. Soc. Rev., 2025, **54**, 7870–7912 | 7911

199 J. Zhang, J. Yang, R. Dai, W. P. Sheng, Y. Su, Y. Zhong, X. Li, L. Tan and Y. Chen, *Adv. Energy Mater.*, 2022, **12**, 2103674.

200 Q. Wang, J. Zhu, Y. Zhao, Y. Chang, N. Hao, Z. Xin, Q. Zhang, C. Chen, H. Huang and Q. Tang, *Carbon Energy*, 2024, **6**, e566.

201 R. Wu, W. Miao, R. Yin, W. Sun, Y. Sun, K. Wang, T. You and P. Yin, *Chem. Eng. J.*, 2025, **504**, 158954.

202 Y. Lao, S. Yang, W. Yu, H. Guo, Y. Zou, Z. Chen and L. Xiao, *Adv. Sci.*, 2022, **9**, 2105307.

203 R. Guo, J. Xia, H. Gu, X. Chu, Y. Zhao, X. Meng, Z. Wu, J. Li, Y. Duan, Z. Li, Z. Wen, S. Chen, Y. Cai, C. Liang, Y. Shen, G. Xing, W. Zhang and G. Shao, *J. Mater. Chem. A*, 2023, **11**, 408–418.

204 F. H. Isikgor, F. Furlan, J. Liu, E. Ugur, M. K. Eswaran, A. S. Subbiah, E. Yengel, M. D. Bastiani, G. T. Harrison, S. Zhumagali, C. T. Howells, E. Aydin, M. Wang, N. Gasparini, T. G. Allen, A. Rehman, E. V. Kerschaver, D. Baran, I. McCulloch, T. D. Anthopoulos, U. Schwingenschlogl, F. Laquai and S. D. Wolf, *Joule*, 2021, **5**, 1566–1586.

205 Z. Xin, Y. Zhao, L. Bian, Y. Cao, J. Duan, Q. Guo, J. Dou, Q. Zhang and Q. Tang, *ACS Mater. Lett.*, 2024, **6**, 3327–3334.

206 Y. Xu, Y. Ren, S. Cheng, L. Zhang, P. Niu, M. Lyu, H. Lu, M. Wang and J. Zhu, *J. Mater. Chem. A*, 2023, **11**, 868–877.

207 C.-C. Zhang, S. Yuan, Y.-H. Lou, Q.-W. Liu, M. Li, H. Okada and Z. K. Wang, *Adv. Mater.*, 2020, **32**, 2001479.

208 C. Shi, Q. Song, H. Wang, S. Ma, C. Wang, X. Zhang, J. Dou, T. Song, P. Chen, H. Zhou, Y. Chen, C. Zhu, Y. Bai and Q. Chen, *Adv. Funct. Mater.*, 2022, **32**, 2201193.

209 K. Zheng, C. Liu, K. Yu, Y. Meng, X. Yin, S. Bu, B. Han, C. Liu and Z. Ge, *Chem. Eng. J.*, 2022, **446**, 137307.

210 W. He, X. Duan, Q. Tang, J. Dou and J. Duan, *Chem. Commun.*, 2024, **60**, 4954–4957.

211 H.-J. Lee, Y.-J. Kang, S.-N. Kwon, D.-H. Kim and S.-I. Na, *Small Methods*, 2024, **8**, 2300948.

212 J. Yang, W. Sheng, X. Li, Y. Zhong, Y. Su, L. Tan and Y. Chen, *Adv. Funct. Mater.*, 2023, **33**, 2214984.

213 J. Gong, X. Fan, Z. Zong, M. Yang, Y. Sun and G. Zhao, *RSC Adv.*, 2023, **13**, 15531.

214 O. V. Oyelade, O. K. Oyewole, D. O. Oyewole, S. A. Adeniji, R. Ichwani, D. M. Sanni and W. O. Soboyejo, *Sci. Rep.*, 2020, **10**, 7183.

215 W.-Q. Wu, Z. Yang, P. N. Rudd, Y. Shao, X. Dai, H. Wei, J. Zhao, Y. Fang, Q. Wang, Y. Liu, Y. Deng, X. Xiao, Y. Feng and J. Huang, *Sci. Adv.*, 2019, **5**, eaav8925.

216 B. Han, Y. Wang, C. Liu, K. Sun, M. Yang, L. Xie, S. Yang, Y. Meng, S. Lin, P. Xu, J. Li, Q. Qiu and Z. Ge, *Angew. Chem., Int. Ed.*, 2023, **62**, 202217526.

217 G. Li, J. Song, J. Wu, Z. Song, X. Wang, W. Sun, L. Fan, J. Lin, M. Huang, Z. Lan and P. Gao, *ACS Energy Lett.*, 2021, **6**, 3614–3623.

218 Y. Sun, W. Miao, W. Sun, Z. Niu, R. Yin, X. Huo, K. Wang, T. You and P. Yin, *Small*, 2024, **20**, 2404272.

219 Q. Wang, X. Jiang, C. Peng, J. Zhang, H. Jiang, H. Bu, G. Yang, H. Wang, Z. Zhou and X. Guo, *Chem. Eng. J.*, 2024, **481**, 148464.

220 J. Yang, Q. Wang, W. Hui, X. Chen, Y. Yao, W. Tang, W. Qiu, X. Xu, L. Song, Y. Wu and Q. Peng, *Energy Environ. Sci.*, 2025, **18**, 1732–1744.

221 X. Jiang, X. Wang, X. Wu, S. Zhang, B. Liu, D. Zhang, B. Li, P. Xiao, F. Xu, H. Lu, T. Chen, A. K.-Y. Jen, S. Yang and Z. Zhu, *Adv. Energy Mater.*, 2023, **13**, 2300700.

222 F. Zheng, L. Z. Tan, S. Liu and A. M. Rapee, *Nano Lett.*, 2015, **15**, 7794–7800.

223 J.-H. Lee, N. C. Bristowe, J. H. Lee, S.-H. Lee, P. D. Bristowe, A. K. Cheetham and H. M. Jang, *Chem. Mater.*, 2016, **28**, 4259–4266.

224 A. Amat, E. Mosconi, E. Ronca, C. Quarti, P. Umari, M. K. Nazeeruddin, M. Grätzel and F. D. Angelis, *Nano Lett.*, 2014, **14**, 3608–3616.

225 L. Guo, G. Xu, G. Tang, D. Fang and J. Hong, *Nanotechnology*, 2020, **31**, 225204.

226 G. Giorgi, J.-I. Fujisawa, H. Segawa and K. Yamashita, *J. Phys. Chem. Lett.*, 2013, **4**, 4213–4216.

227 G. Liu, M. Ghasemi, Q. Wei, B. Jia, Y. Yang and X. Wen, *Adv. Energy Mater.*, 2025, **15**, 2405239.

228 J. Wu, S.-C. Liu, Z. Li, S. Wang, D.-J. Xue, Y. Lin and J.-S. Hu, *Sol. RRL*, 2024, **8**, 2400203.

229 T. S. Sherkar, C. Momblona, L. Gil-Escrig, J. Ávila, M. Sessolo, H. J. Bolink and L. J. A. Koster, *ACS Energy Lett.*, 2017, **2**, 1214–1222.

230 S. Tan, I. Yavuz, M. H. Weber, T. Huang, C.-H. Chen, R. Wang, H.-C. Wang, J. H. Ko, S. Nuryyeva, J. Xue, Y. Zhao, K.-H. Wei, J.-W. Lee and Y. Yang, *Joule*, 2020, **4**, 2426–2442.

231 E. Aydin, M. D. Bastiani and S. D. Wolf, *Adv. Mater.*, 2019, **31**, 1900428.

7912 | *Chem. Soc. Rev.*, 2025, **54**, 7870–7912

This journal is © The Royal Society of Chemistry 2025